Doctorare Dissertation
博士論文

Experimental and numerical investigation of universal fluctuations in out-of-equilibrium interface growth

（非平衡界面成長に現れる普遍ゆらぎに関する実験的・数値的研究）

A Dissertation Submitted for Degree of Doctor of Philosophy
December 2018
平成30年12月博士（理学）申請

Department of Physics, Graduate School of Science,
The University of Tokyo
東京大学大学院理学系研究科物理学専攻

Yohsuke T. Fukai
深井 洋佑

Abstract

The concept of scale-invariance-associated universality has been successfully extended to describe out-of-equilibrium phenomena with fluctuations, becoming an essential concept to explore universality in out-of-equilibrium systems. In this dissertation, the author aims to extend knowledge about the concept itself, by studying out-of-equilibrium interface growth phenomena associated with the (1+1)-dimensional Kardar–Parisi–Zhang (KPZ) universality class, a prototypical universality class for out-of-equilibrium systems.

The dissertation is devoted to the following two subjects: The first is the fluctuation of interfaces in the KPZ class with curved initial conditions, and the second is the fluctuation of a growing phase-boundary interface formed near the critical point of a nonequilibrium phase transition of the directed percolation (DP) universality class.

The first study is motivated by recent theoretical and experimental findings which indicate that interfaces in the KPZ class show distinct statistical properties depending on their geometries, or equivalently, the initial conditions. Though the statistical properties have been intensively studied for special cases such as flat and circular interfaces, knowledge for more general cases is still limited. To experimentally investigate interfaces with general initial conditions, the author constructed an experimental setup that enables investigation of the growth of the turbulent state of an electrically driven liquid-crystal film from arbitrarily designed initial conditions. With the experiments as well as numerical simulations of a cluster growth model, we revealed statistical properties of the interfaces with initial conditions with a shape of a circular ring, which naturally generalize those of the flat and circular interfaces. We further discuss the theoretical representation of the height distribution for locally parabolic initial conditions by a conjectural formula called the *variational formula*, which was found to be consistent with the experimental and numerical results we obtained.

The second study is inspired by empirical observations implying that models showing the DP-class transition also shows the growth of the phase-boundary interfaces with the KPZ-class fluctuation far from the critical point. To elucidate interface fluctuation near the critical point where the universality of the DP class arises, the author numerically investigated the interface growth process with the Langevin equation which describes the DP-class transition. We found a crossover connecting a novel interface fluctuation characterized by the DP-class universal exponents and the KPZ-class fluctuation.

Acknowledgements

First of all, I would like to express my sincerest gratitude to Prof. Masaki Sano, who supervised me for five years. During my Master course and Ph. D. course with run-and-tumble struggle, his advice has always been inspiring for me. I also appreciate the open and lively research environment and many opportunities of interaction with outstanding researchers he offered, without which I could not finish this Ph. D. course. I would like to celebrate his successful upcoming retirement with praying for his future success in the new environment.

I am genuinely thankful to Prof. Kazumasa A. Takeuchi for five years of mentoring and collaboration. I truly appreciate his insightful and instructive comments, warm support and patience. His passionate attitude towards science has always been, and will be, my guideline to be a scientist. Having started from elementary observations, the accomplishment on the curved KPZ interfaces in collaboration with him is my invaluable treasure now.

I am truly grateful to Prof. Tetsuya Hiraiwa, the assistant processor of the Sano laboratory, for his extensive supports, including the critical reading of manuscripts which was indispensable to continue my research.

The study on the relationship between the directed percolation and the KPZ class was motivated and propelled in collaboration with Prof. Tetsuya Hiraiwa, Dr. Keiichi Tamai and Mr. Hiroki Yamaguchi. I immensely appreciate their intensive and active collaboration which always inspired me.

I note that this research could not have been accomplished without deep discussions and valuable comments by many outstanding scientists. Though I cannot address all the people, especially I would like to thank the former and present members of the Sano laboratory and the Takeuchi laboratory. In the Sano laboratory, I thank Dr. Kyogo Kawaguchi for enlightening me for various attractive fields of biophysics, Dr. Sosuke Ito for broadening my mind toward the field of stochastic thermodynamics, Dr. Yohei Nakayama for continuous advices and discussions on hidden entropy production and molecular motors, and Dr. Kotaro Otomura for discussions on colloidal particles and many useful advices on numerical programming.

I have always been learning a lot from Dr. Takaki Yamamoto, who knowledgeably helped me about liquid crystal experiment, and Dr. Daiki Nishiguchi, who introduced me a fascinating world of active matter. I thank Dr. Keiichi Tamai for professional advices about the directed percolation and turbulence. Having many exciting discussions Ms. Sakurako Tanida, Mr. Masahito Uwamichi and Mr. Junichiro Iwasawa have been a great obliged for

me. I appreciate advice on many aspects of the experiments by Dr. Masafumi Kuroda and Mr. Hisanori Ohnuma, and warm support on administration by Ms. Chinae Kurimoto as the secretary of the laboratory.

In the Takeuchi laboratory, I appreciate Ms. Somayeh Zeraati for experimental collaborations and precious discussions on various things, Dr. Renan A. L. Almeida for invaluable discussions about the KPZ class and much more, Mr. Yasufumi Ito and Mr. Takayasu Iwatsuka for intensive discussions on the liquid crystal experiment.

I would like to take this opportunity to thank Prof. Peter Yunker, who hosted me for three months in the Georgia Institute of Technology. Though I could not include the results of the research I conducted there in my dissertation, they inspired me to obtain the results presented in the dissertation. I thank Mr. Federico Lancia and Prof. Nathalie H. Katsonis for supporting me visit their laboratory and letting me learn a lot about the liquid crystal experiments. I am grateful to Prof. Sergio Andraus for continuous discussion on the KPZ interfaces with curved initial conditions.

Finally, I would like to thank my family who supported me throughout my life with great care and generosity.

Notations

$X := Y$	Define X by Y.
$X =: Y$	Define Y by X.
$f(t) \propto g(t)$	$f(t)$ is proportional to $g(t)$; $f(t) = Cg(t)$ $(C \neq 0)$.
$f(t) \sim g(t)$	$f(t)$ is asymptotically proportional to $g(t)$; $\lim_{t\to\infty} \frac{f(t)}{g(t)} = C$ $(C \neq 0)$.
$f(t) \simeq g(t)$	$f(t)$ is asymptotically equal to $g(t)$; $\lim_{t\to\infty} \frac{f(t)}{g(t)} = 1$.
∂_x	Partial derivative with respect to a variable x ; $\frac{\partial}{\partial x}$.
$f(t) = \mathcal{O}(g(t))$	$f(t)$ is of the order of $g(t)$; $f(t) \sim g(t)$.
$f(t) = o(g(t))$	$f(t)$ is of the order smaller than $g(t)$; $\lim_{t\to\infty} \frac{f(t)}{g(t)} = 0$.
$X \approx Y$	X is approximately equal to Y.
$\mathbb{1}_A$	The indicator function; $\mathbb{1}_A = \begin{cases} 1 & \text{(if the condition } A \text{ is satisfied)} \\ 0 & \text{(otherwise)} \end{cases}$.
$\langle X \rangle$	(Ensemble) average of X.
$\langle X^k \rangle_c$	k-th cumulant of X.
$\mathrm{Sk}[X]$	Skewness of X.
$\mathrm{Ku}[X]$	Kurtosis of X.
$\mathrm{Cov}[X, Y]$	Covariance between X and Y.

Abbreviations

AC	alternative current
CCD	charge-coupled device
CDP	compact directed percolation
$(d+1)$-D	$(d+1)$-dimensional (d is the spatial dimension)
DP	directed percolation
DSM	dynamic scattering mode
EW	Edwards–Wilkinson
FKPP	Fisher–Kolmogorov–Petrovsky–Piscounov

GOE	Gaussian orthogonal ensemble
GUE	Gaussian unitary ensemble
IFTA	iterative Fourier transform algorithm
KPZ	Kardar–Parisi–Zhang
LC	liquid crystal
PNG	polynuclear growth model
SLM	spatial light modulator
(T)ASEP	(totally) asymmetric simple exclusion process
TW	Tracy–Widom
UV	ultra violet

Contents

Chapter 1

Introduction

Studying physical phenomena not only provides us with insights of themselves, but sometimes also introduces novel perspectives to understand the real world. Critical phenomena are one of the successful examples, which has led to the discovery of the renormalization group and associated universality of the phenomenological theories. Standing on a giant of those efforts, now we are on the stage to explore scale invariant phenomena in out-of-equilibrium systems and see how the concepts of scale-invariance-associated universality are extended. In this chapter, I briefly review the general background of the Kardar–Parisi–Zhang (KPZ) class, one of the representative classes for out-of-equilibrium systems, and then state our motivation.

1.1 Scale invariance and universality in growing interfaces

In the field of equilibrium critical phenomena, the emergent scale invariance and the universality of the phenomenology near the critical point has been understood using the concept of the celebrated renormalization group [1–3]. Regarding that the universality of the phenomenology is associated with the scale invariance, it is natural to consider that the scale-invariance-associated universality is not only for equilibrium systems. Indeed, universal phenomenological theories associated with scale invariance have attracted considerable interest in genuinely out-of-equilibrium systems, one example of which is fluctuations of growing interfaces, our primary target in this dissertation.

Often spontaneous fluctuation appears in growing interfaces, both in models and experiments [4, 5]. Here let us assume that, in a sufficiently coarse-grained scale, one can describe the interface shape by one-valued function $h(\mathbf{x}, t)$, where $\mathbf{x} \in \mathbb{R}^d$ is the position with the substrate dimension d and $t \in \mathbb{R}$ is the time. We call interfaces described in this form $(d+1)$-dimensional [$(d+1)$-D] interfaces.

Often large-scale profile of the interfaces are governed by two length scales diverging with time, as first observed with numerical simulations of interface models called the ballistic deposition model and the Eden model [4, 6, 7]. One is the fluctuation amplitude, defined

as, e.g., the standard deviation of the height. The other is a length scale transverse to the growth direction which can be observed by the decay of the correlation of the height in a snapshot of the interface.

Scale invariance often spontaneously appears in those interfaces with diverging length scales. For example, let us consider the *width* of the height $w(l,t)$, which is defined as the standard deviation of the height measured in a box with a side length of l as

$$w(l,t) =: \sqrt{\left\langle \left\langle (h(\mathbf{x},t) - \langle h(\mathbf{x},t)\rangle_l)^2 \right\rangle_l \right\rangle}, \tag{1.1}$$

where $\langle \cdots \rangle_l$ is the average in a box with a side length of l (Fig. 1.2). For a sufficiently large system and long time, $w(l,t)$ often follows a scaling form called the Family-Vicsek scaling [4, 6], which reads

$$w(l,t) \simeq t^{\beta} f(l/\xi(t)), \tag{1.2}$$

where $f(x)$ is a function satisfying

$$f(z) \sim \begin{cases} z^{\alpha} & (z \ll 1) \\ \text{const.} & (z \gg 1) \end{cases}, \tag{1.3}$$

$\xi(t)$ is a lengthscale called the correlation length satisfying $\xi(t) \sim t^{1/z}$, and the exponents β, z and α satisfies $\alpha := \beta z$. This scaling form suggests the existence of the scale invariance with respect to the transformation

$$t \to bt,\ \mathbf{x} \to b^{1/z}\mathbf{x},\ \delta h \to b^{\beta}\delta h, \tag{1.4}$$

where $\delta h := h - \langle h \rangle$. Similarly to that found critical phenomena, the scale invariance with diverging characteristic scales suggests the universality of the exponents. Indeed, the exponents have been experimentally and numerically found to be universal for microscopically different systems, and regarded as the indices for the universality classes similarly to those for critical phenomena [4, 5].

1.2 Continuum description and Kardar–Parisi–Zhang universality class

Regarding the universality in the large scale, it is reasonable to consider a simplest coarse-grained description of the growing interface reproducing the universal features, in analogy with the ϕ^4 model for the Ising universality class [3].

To begin with, let us put several assumptions for the dynamics. We consider the cases where the growth is local in the sense that, in a coarse-grained scale, the time derivative $\partial_t h(\mathbf{x},t)$ only depend on the value of the height $h(\mathbf{x},t)$ and its spatial derivatives, excluding

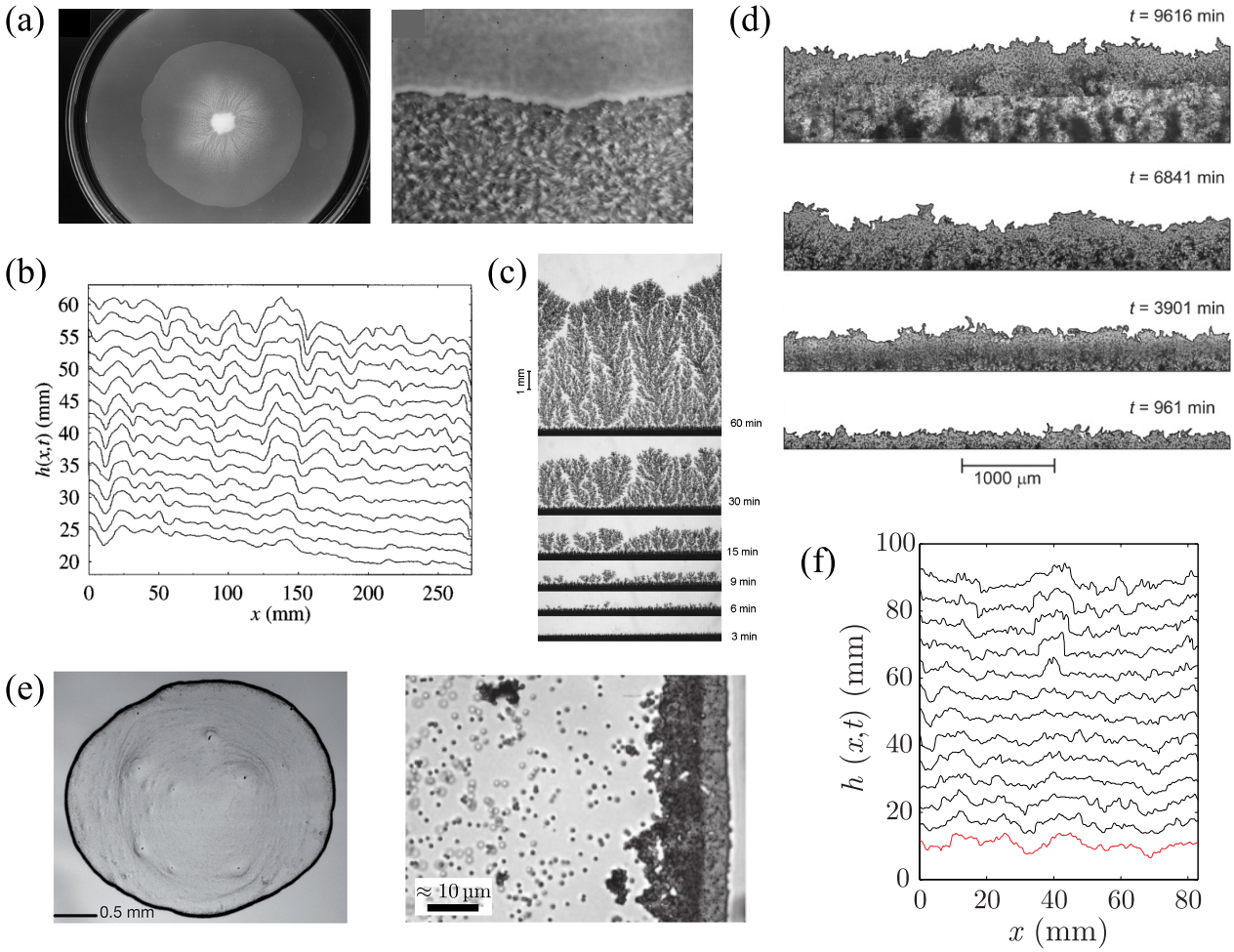

Figure 1.1: Examples of growing (1+1)-D interfaces showing scale-invariant fluctuation, featuring those with the KPZ-class exponents. (a) Growing colony of *Bacillus subtilis* [8]. The right is the magnified view. The figure is adopted from [9]. (b) Slow combustion front in a paper sheet [10]. (c) Electrodeposition of silver in a quasi-two-dimensional cell [11]. (d) Front of the growing Hela cell colony [12]. (e) Formation of ring-shaped deposition by evaporation of colloidal suspension (coffee-ring effect) [13]. The right is the magnified view during the evaporation. KPZ-class fluctuations are observed with slightly ellipsoidal particles [14]. (f) Chemical reaction front in porous media [15]. The figures are adopted from the corresponding references with permissions of (a) Elsevier (b-d,f) American Physical Society and (e) Springer Nature.

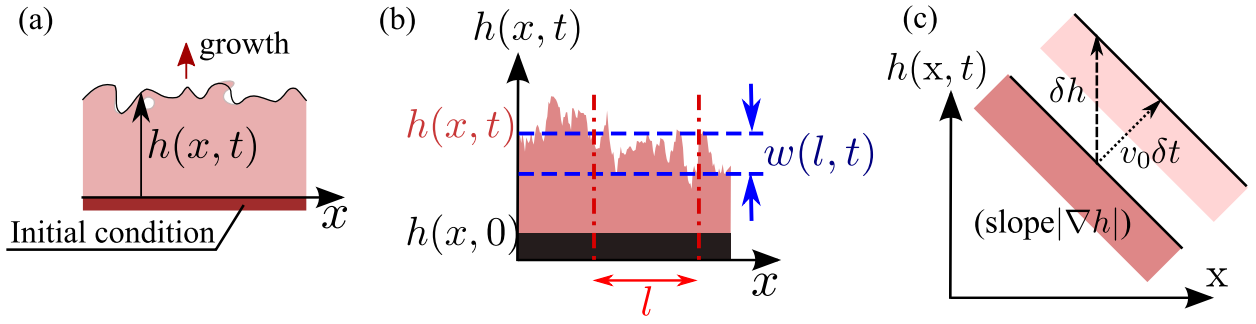

Figure 1.2: (a) Schematic for the definition of the height for the (1+1)-D interface. The height $h(x,t)$ of the interfaces are defined as a single-valued function by coarse-graining the void and overhangs. (b) Schematic for the definition of the width $w(l,t)$ in the case of (1+1)-D interfaces [Eq. (1.1)]. (c) Schematic for an intuitive interpretation of the nonlinear term in the KPZ equation (1.9). For a interface with the slope $|\nabla h|$, isotropic growth with the speed v_0 leads to the growth of the height h as $\frac{\delta h}{\delta t} = v_0\sqrt{1+(\nabla h)^2} = v_0 + \frac{v_0}{2}(\nabla h)^2 + \cdots$.

the cases where the growth rate at distinct points globally couples through other fields. We further assume that the growth occurs homogeneously in space and time, which requires the translational invariance of the equation with respect to $\mathbf{x} \to \mathbf{x}+\mathbf{x}_0$, $h \to h+h_0$ and $t \to t+t_0$, where $\mathbf{x}_0$, h_0, and t_0 are time-independent constants. Finally, for simplicity, we assume that the noise has a shortly-ranged correlation, and can be approximated by a white Gaussian noise in a sufficiently coarse-grained scale. With those assumptions, the Langevin equation

$$\partial_t h(\mathbf{x},t) = F\left[\nabla h(\mathbf{x},t), \nabla^2 h(\mathbf{x},t), \dots\right] + \sqrt{D}\eta(\mathbf{x},t), \tag{1.5}$$

where $D > 0$ and $\eta(\mathbf{x},t)$ is the white Gaussian noise satisfying

$$\langle \eta(x,t)\rangle = 0, \ \langle \eta(\mathbf{x},t)\eta(\mathbf{x}',t')\rangle = \delta(\mathbf{x}-\mathbf{x}')\delta(t-t'), \tag{1.6}$$

is a suitable description.

First, let us consider the simplest case without the spatial derivatives

$$\partial_t h(\mathbf{x},t) = \sqrt{D}\eta(\mathbf{x},t). \tag{1.7}$$

This case corresponds to, for example, the case where particles fall to the surface randomly and attach to the surface irrespective to the shape of the interface. This equation leads to the divergent fluctuation amplitude irrespective to the length of the interface. Evidently, $w(l,t)$ diverges as $w(l,t) \sim t^\beta$ with $\beta = 1/2$ according to the central limit theorem, with the one-point distribution of $h(\mathbf{x},t)$ following the Gaussian distribution. No spatial correlation is formed in this case.

To reproduce the Family-Vicsek scaling laws in which the time and length scales are coupled, one needs to introduce the spatial derivative terms allowed by the symmetries. In

1981, S. F. Edwards and D. R. Wilkinson considered a model in which a particle randomly ascends and relax toward a local minimum of the interface, and derived a coarse-grained linear Langevin equation [Edwards–Wilkinson (EW) equation] [16], which reads

$$\partial_t h(\mathbf{x},t) = \nu\nabla^2 h(\mathbf{x},t) + \sqrt{D}\eta(\mathbf{x},t) \tag{1.8}$$

where $\nu > 0$. The solution of this equation possesses the scale invariance [4, 7, 16] with the exponents $\beta = (2-d)/4$ and $z = 2$, defining the Edwards–Wilkinson universality class.

Notably, the exponents that had been universally found in numerical models such as the ballistic deposition and the Eden model on a one-dimensional substrate was different from the prediction of the EW class ($\beta = 1/4$ and $z = 2$) with the values taking $\beta \approx 1/3$ and $z \approx 3/2$ [4, 7]. One can interpret this discrepancy as the consequence of the symmetry $h \to -h$ that the EW equation possesses, which is in general absent in non-equilibrium growing interfaces.

In 1986, M. Kardar, G. Parisi and Y.-C. Zhang proposed a simple Langevin equation without the symmetry $h \to -h$, which can be regarded as the equation describing the general cases. It is nowadays called the Kardar–Parisi–Zhang (KPZ) equation and reads

$$\partial_t h(\mathbf{x},t) = \nu\nabla^2 h(\mathbf{x},t) + \frac{\lambda}{2}\left[\nabla h(\mathbf{x},t)\right]^2 + \sqrt{D}\eta(\mathbf{x},t) \tag{1.9}$$

where $\lambda > 0$. The non-linear term, that breaks the symmetry, can be intuitively interpreted by considering the effect of the growth normal to the interface [Fig. 1.2(c)] since the growth speed v of an inclined interface growing normally to the interface with the speed v_0 is written as $v = v_0\sqrt{1+(\nabla h)^2} = v_0 + \frac{v_0}{2}(\nabla h)^2 + \cdots$ [4] [Fig. 1.2(c)].

For the $(1+1)$-D cases, the exponents for the KPZ equation can be exactly derived [4, 7, 17]. First, because the stationary probability distribution for the Fokker-Planck equation is that for the Brownian motion,

$$\mathcal{P}[h(x)] \propto \exp\left(-\int \mathrm{d}x \left[\frac{\nu}{D}(\partial_x h)^2\right]\right), \tag{1.10}$$

one obtains $\alpha = 1/2$. Then the $z = 3/2$ is obtained by the scaling relation $\alpha + z = 2$ which is the consequence of the symmetry that the KPZ equation possesses [4, 7, 17]. The exponents suggest the scale invariance with respective to

$$t \to bt,\ x \to b^{2/3}x,\ \delta h \to b^{1/3}\delta h \tag{1.11}$$

defining the (1+1)-D KPZ universality class. The exponents for the (1+1)-D KPZ class were consistent with those found in the ballistic deposition and the Eden model, and nowadays have been observed in various experiments (Fig. 1.1) and models [4], confirming its universality [5].

For higher-dimensional cases [1], although the exact values of the exponents are still un-

[1] For the KPZ class with $d \geq 3$, the renormalization-group argument suggests that the EW-class fluctuation

known, its universality has been confirmed for some cases. Particularly, the properties of the $(2+1)$-D KPZ class, relevant for applications such as thin-film growth, have been intensively studied [20], and the universal exponents and even the universal height distribution have been observed experimentally [21, 22].

1.3 Kardar–Parisi–Zhang class for various phenomena

The KPZ class not only describe interface fluctuations, but also is relevant for various fields in nonequilibrium statistical physics. Here some examples out of the vast area are discussed.

First, by the variable transformation called the Hopf–Cole transformation

$$z(\mathbf{x},t) := \exp\left[\frac{\lambda}{2\nu}h(\mathbf{x},t)\right], \tag{1.12}$$

the KPZ equation is transformed into the stochastic heat equation

$$\partial_t z(\mathbf{x},t) = \nu\triangle z(\mathbf{x},t) + \frac{\lambda\sqrt{D}}{2\nu}z(\mathbf{x},t)\eta(\mathbf{x},t). \tag{1.13}$$

The solution of (1.13) with the initial condition $z(\mathbf{x},t)$ can be written in the form of the path integral, which can be interpreted as the partition function for a directed polymer in a random environment [4, 23, 24].

Also, by the transformation $\mathbf{u} := -\lambda\nabla h(\mathbf{x},t)$, one can transform the KPZ equation into

$$\partial_t \mathbf{u}(\mathbf{x},t) + (\mathbf{u}\cdot\nabla)\,\mathbf{u} = \nu\nabla^2\mathbf{u} - \lambda\sqrt{D}\nabla\eta \tag{1.14}$$

which is known as the noisy Burgers equation [4, 24, 25], indicating that the KPZ class can describe fluctuating hydrodynamics. An analogical argument has been used to understand behavior of conserved quantities in an anharmonic chain in terms of the coupled KPZ equation [26]. Another example in this context is a model called (totally) asymmetric simple exclusion process [(T)ASEP] [27], a particle-transport model which can be mapped into a interface growth model in the KPZ class [28].

In addition to those "classical" applications, the KPZ universality now has been found in a variety of fields including, but not restricted to, perturbation of evolution in spatiotemporal chaos [29], incompressible active matter [30], and even evolution of the entanglement entropy in a quantum spin chain under random unitary dynamics [31].

---

is observed with sufficiently small value of $(\lambda^2 D)/\nu^3$, and there exists the transition between the EW regime and the other regime with non-trivial "strong-coupling" exponents. The upper critical dimension d_c below which the strong-coupling exponents survive is still controversial, but some studies implies that $d_c = \infty$ [18, 19].

1.4 Exact solution, liquid crystal experiments and universality subclasses

In these two decades, there has been a breakthrough for the (1+1)-D KPZ class, that is, the derivation of the exact solutions for statistical properties of the interface fluctuation such as the height distribution and spatial correlation (Sec. 2.1.1). These theoretical efforts revealed the novel property of the KPZ class: the *geometry dependence* (or equivalently, the initial condition dependence) of the universal fluctuation. More specifically, for example, the flat interfaces growing from a line and the circular interfaces growing from a point shows distinct statistical properties of their interface fluctuation, while they are governed by the same universal exponents [24, 32, 33]. The experimental relevance of this geometry dependence was confirmed in experiments investigating the growth of a turbulent state invading another metastable turbulent state in an electrically driven thin film of liquid crystal (LC) [34–36]. The theoretical, experimental (and also numerical) effort, overall, established the physically relevant idea of the *universality subclasses*, that is characterized by the same scaling exponent yet different statistical properties of the fluctuation.

1.5 Motivations and organization of the dissertation

In this section, I describe two perspectives for the KPZ class, that we expect to help us further understand universal fluctuations in out-of-equilibrium systems. I then state our motivations and outline the organization of the following chapters.

Generalization of flat and circular universality subclasses

One of the perspectives is the geometry-dependence of the universal fluctuations revealed in the exact solutions and the LC electroconvection experiment. Since this feature has not been expected, to our knowledge, from the standard argument of the renormalization group, it is expectable that a novel framework is necessary to understand this geometry-dependence. However, the problem is that the geometry for which the interface fluctuation has been explicitly investigated is rather limited at this time. In Chapter 2, we generalize our knowledge by experimentally, numerically and theoretically studying interfaces with curved initial conditions, which can naturally interpolate (and extrapolate) the particular cases of the flat and circular interface which have been investigated intensively so far.

Connection with directed percolation universality class

The fact that the KPZ fluctuation was found in the LC electroconvection was also suggestive, since the DSM2 state in the LC electroconvection experience a non-equilibrium phase transition called the directed percolation (DP) transition (briefly reviewed in Sec. 3.1) [37, 38], suggesting the connection between the KPZ class and the critical fluctuation of the directed

percolation transition. Since the DP transition is also characterized by a scale-invariant fluctuation, this let us anticipate that there is a relationship between the KPZ class and the DP class that is yet to be revealed. In Chapter 3, with an extensive simulation of the Langevin equation for the DP universality class, we establish a picture on the relationship between those classes in terms of the interface growth.

Finally, we conclude in Chapter 4 with discussing future perspectives.

Chapter 2

Kardar-Parisi-Zhang interfaces with curved initial conditions

Related publications by author:

- Y. T. Fukai and K. A. Takeuchi, "Kardar–Parisi–Zhang Interfaces with Inward Growth", Physical Review Letters **119**, 030602 (2017).
- Y. T. Fukai and K. A. Takeuchi, *in preparation.*

Contribution:

The author (Y. T. Fukai) conducted the experiments and the numerical simulations under advice and direction by the collaborator (Prof. K. A. Takeuchi). The theory (Sec. 2.4) mainly owe to a discussion between Prof. P. le Doussal and Prof. K. A. Takeuchi, with the author's contribution on its numerical evaluation.

2.1 Topical introduction

In the previous chapter, the universality of the $(1+1)$-D KPZ class in the sense of the scaling exponents has been discussed. In this section, we focus on the universality *beyond* the scaling exponents and the concept of the universality subclasses, which have recently been revealed by a synergy of theoretical, experimental and numerical efforts, and motivates the study in this chapter.

2.1.1 Overview of theoretical perspectives

In this subsection, I summarize theoretical progress on the geometry-dependent fluctuation of the (1+1)-D KPZ interfaces. I first note that, since the aim of this chapter is a brief overview, I leave more precise and comprehensive description to review articles such as Ref. [24, 28, 33, 39–43].

As well as the scaling exponents, the universal height distribution and correlation have long attracted attention. If the correlation length $\xi(t) \sim t^{2/3}$ is sufficiently larger than the system size (the total length of the interface) L (the stationary regime), the stationary height profile (1.10) is realized and the height fluctuation is governed by the Gaussian distribution. In contrast, for the cases where $\xi(t)$ is much smaller than L (growth regime), numerical works around 1990 revealed that the height distribution shows *non*-Gaussian distributions [44–46], contrary to earlier expectations [47–49]. Studies on this fluctuation in the growth regime have led to the concept of the geometry-dependent universal fluctuation and universality subclasses.

To discuss the statistical properties of the fluctuation, let us consider rescaling the height $h(x,t)$ of the interfaces by non-universal characteristic time and length scales of the interfaces. Following the method in in Ref. [17], we first define experimentally and numerically measurable parameters characterizing the typical time and length scales: the asymptotic growth speed v_∞, strength of the nonlinearity λ, and the amplitude of the stationary Brownian motion A, which are defined by

$$v_\infty := v_\infty(0) \tag{2.1}$$

$$\lambda := v_\infty''(0) \tag{2.2}$$

$$A := \lim_{l\to\infty}\lim_{t\to\infty}\lim_{L\to\infty} l^{-1}\left\langle [h(x+l,t)-h(x,t)]^2 \right\rangle, \tag{2.3}$$

where $\langle\cdot\rangle$ denotes the ensemble average and $v_\infty(s)$ is the asymptotic growth speed of the interfaces $h^{(s)}(x,t)$ with the initial condition $h^{(s)}(x,0) = sx$ with the global slope s,

$$v_\infty(s) := \lim_{t\to\infty, L\to\infty} \left\langle \partial_t h^{(s)}(x,t) \right\rangle. \tag{2.4}$$

Then, considering the dimensions of v_∞, λ and A, the KPZ scaling (1.11) suggests that one can write the height $h(x,t)$ in the growth regime in a form of

$$h(x,t) \simeq v_\infty t + (\Gamma t)^{1/3}\, \chi\left(x/\xi(t), t\right) \tag{2.5}$$

$$\xi(t) := \frac{2}{A}(\Gamma t)^{2/3}, \tag{2.6}$$

where $\Gamma := \frac{A^2|\lambda|}{2}$. $\chi(x',t)$ is a universal stochastic variable, that has been revealed to be geometry-dependent as we will see.

In 1992, the authors of Ref. [17] investigated the statistical properties characterizing $\chi(x',t)$ such as the cumulants $\left\langle \chi(x',t)^k \right\rangle_c$ of the one-point distribution [1], and numerically demonstrated its universality with several interface models and directed polymer models.

[1] The cumulants $\left\langle X^k \right\rangle_c$ of a random variable X with $k = 1, \ldots, 4$ can be written as: $\langle X \rangle_c = \langle X \rangle$ (mean), $\left\langle X^2 \right\rangle_c = \left\langle \delta X^2 \right\rangle$ (variance), $\left\langle X^3 \right\rangle_c = \left\langle \delta X^3 \right\rangle$, $\left\langle X^4 \right\rangle_c = \left\langle \delta X^4 \right\rangle - 3\left\langle \delta X^2 \right\rangle$, where $\delta X := X - \langle X \rangle$.

For interfaces with the flat initial condition, the cumulants values were estimated as

$$\left|\left\langle\chi^1\right\rangle_c\right| = 0.729(49),\ \left\langle\chi^2\right\rangle_c = 0.657(21),\ \left|\left\langle\chi^3\right\rangle_c\right| = 0.142(10),\ \left\langle\chi^4\right\rangle_c = 0.050(5), \tag{2.7}$$

indicating that the distribution has non-zero mean and is clearly different from Gaussian with the non-zero third and fourth cumulants, or equivalently, the skewness and kurtosis

$$\mathrm{Sk}[\chi] := \frac{\langle\chi^3\rangle_c}{\langle\chi^2\rangle_c^{3/2}} = 0.28(4) \neq 0,\ \mathrm{Ku}[\chi] := \frac{\langle\chi^4\rangle_c}{\langle\chi^2\rangle_c^2} \approx 0.12 \neq 0. \tag{2.8}$$

They also observed an initial condition dependence of χ, by investigating the fluctuation of interfaces in the stationary state, whose height $\bar{h}(x,t)$ is defined by

$$\bar{h}(x,t) := h(x,t) - h(x,0) \tag{2.9}$$

where $h(x,0)$ takes the stationary profile of the interface [analogous to Eq. (1.10) for each model]. The values of the mean, variance, third cumulant and the skewness

$$\langle\chi\rangle = 0 \text{ (by definition)},\ \left\langle\chi^2\right\rangle_c = 1.130(5),\ \left\langle\chi^3\right\rangle_c = 0.398(8),\ \mathrm{Sk}[\chi] \approx 0.33 \tag{2.10}$$

were found to be different from those of the flat interfaces. In particular, the difference in the skewness implied that the distribution shape itself is different from that for the flat interfaces.

Around the beginning of the 2000s, the exact statistical properties for the universal stochastic variable $\chi(x',t)$ have been revealed for models belonging to the KPZ class. This was accomplished for the totally asymmetric simple exclusion process (TASEP) by K. Johansson [27], and the polynuclear growth model (PNG) by M. Prähofer and H. Spohn [32, 50]. Notably, it was rigorously found that the statistical properties of stochastic variable $\chi(x',t)$ depend on the geometry, or initial condition of the interfaces. The circular (or droplet-shaped) PNG interfaces whose initial condition is a point, flat interfaces with infinite line initial condition, and stationary interfaces whose height is defined analogously to Eq. (2.9) showed different one-point height distributions. For example, the height distribution of the flat (circular) interfaces are found to be governed by the largest-eigenvalue distribution for random matrices called the Gaussian orthogonal (unitary) ensemble [GOE (GUE)] [51] [called the GOE (GUE) Tracy–Widom [GOE (GUE)-TW] distribution]. In other words, the one-point distribution of $\chi(x',t)$ is the same as the distribution of a random variable χ_1 (χ_2) following the GOE(GUE) distribution [2], whose cumulative distribution function can be written as [51–54]

$$\mathrm{Prob}\left[\chi_1 < s\right] = \det\left[\mathbb{I} - P_0 B_{2^{2/3}s} P_0\right] \tag{2.11}$$

$$\mathrm{Prob}\left[\chi_2 < s\right] = \det\left[\mathbb{I} - P_s K_{\mathrm{Ai}} P_s\right], \tag{2.12}$$

[2]We note here χ_1 is rescaled by the factor $2^{2/3}$ from the conventional definition of GOE-TW, in order to employ the same notation (2.5) for both of the flat and circular interfaces.

respectively, where we $\det[\mathbb{I}+\cdots]$ is the Fredholm determinant [52, 55], defined by

$$\det[\mathbb{I}+zK] := \sum_{n=0}^{\infty}\frac{z^n}{n!}\int_{-\infty}^{\infty}\det\left[K\left(x_i,x_j\right)\right]_{i,j=1}^{n}\mathrm{d}x_1\cdots\mathrm{d}x_n, \tag{2.13}$$

where P_x is the projection operator onto $[x,\infty)$, $K_{\mathrm{Ai}}(x,y) := \int_0^\infty \mathrm{d}\lambda \mathrm{Ai}(x+\lambda)\mathrm{Ai}(y+\lambda)$, and $B_s(x,y) := \mathrm{Ai}(x+y+s)$ where $\mathrm{Ai}(\cdot)$ is the Airy function [56]. Similarly, a different distribution called the Baik-Rains distribution was found for the stationary interfaces [32, 57]. The GUE-TW distribution was also found in the Johansson's exact solution for the TASEP with the initial condition that corresponds to a wedge shape in the interface picture, suggesting the universality of χ_2 for curved interfaces with point or wedge initial conditions. The values of the cumulants of the exact solutions are summarized in Table 2.1, which are close to those observed numerically [(2.7), (2.10)].

Subsequent studies further revealed the universality of the geometry-dependent distributions. For example, the GOE-TW and the Baik-Rains distributions are also found in the exact solutions for the TASEP with the initial conditions that corresponds to the flat and stationary interfaces, respectively [53, 54, 58]. Also, notably, the exact solutions were derived for the KPZ equation itself, despite its non-linear nature and its delicate mathematical definition [24, 42, 59, 60]. In 2010, T. Sasamoto and H. Spohn considered the KPZ equation with the narrow-wedge initial condition

$$h(x,0) = |x|/\delta,\ (\delta\to 0) \tag{2.14}$$

which corresponds to the delta-function initial condition

$$z(x,0) := \exp\left[\frac{\lambda}{2\nu}h(x,0)\right] = \delta(x) \tag{2.15}$$

in the sense of the stochastic heat equation (1.13), and found that the one-point distribution is asymptotic to the GUE-TW distribution [39, 59, 61]. The similar result was also derived independently by G. Amir, I. Corwin and J. Quastel rigorously [60]. Also, in the meanwhile, P. Calabrese, P. le Doussal and A. Rosso and independently V. Dotsenko succeeded to derive the GUE-TW for the wedge initial condition from a different approach, mapping to the Schrödinger equation of the Lieb-Linger model and using the Bethe ansatz [24, 62, 63]. Although the calculation involves a diverging sum which cannot be treated rigorously, the method is successfully extended to the flat [64] and the stationary [65, 66] interfaces to give the asymptotic distributions and correlations consistent with the other KPZ-class models. For the stationary case, the exact one-point distribution was later rigorously derived by A. Borodin, I. Corwin, P. Ferrari, and B. Vető [67].

The equal-time spatial correlations of $\chi(x',t)$ have also been derived exactly for several models with the flat, circular and stationary interfaces [3]. They are also found to take

[3]For the stationary case, we redefine the height by $\bar{h}(x,t)$ in (2.9).

Table 2.1: Three canonical subclasses of the KPZ universality class

name	flat	circular	stationary
initial condition	flat	point or wedge	stationary
one-pt. distribution $\chi(x',t)$	GOE-TW χ_1	GUE-TW χ_2	Baik-rains χ_0
$\langle\chi\rangle$	-0.76007	-1.77109	0
$\langle\chi^2\rangle_c$	0.63805	0.81320	1.15039
Sk$[\chi]$	0.2935	0.2241	0.35941
Ku$[\chi]$	0.1652	0.09345	0.28916
spatial correlation $\chi(x'_1,t),\ldots,\chi(x'_n,t)$	Airy_1 $\mathcal{A}_1(x)$	Airy_2 $\mathcal{A}_2(x)$	$\mathrm{Airy}_{\mathrm{stat}}$ $\mathcal{A}_{\mathrm{stat}}(x)$
temporal covariance $C_t(t,t_0)$	t^{-1}	$t^{-1/3}$	$t^{-1/3}$

geometry-dependent forms, $\mathcal{A}_1(x')$, $\mathcal{A}_2(x') - x'^2$, and $\mathcal{A}_{\mathrm{stat}}(x')$, where $\mathcal{A}_1(\cdot)$, $\mathcal{A}_2(\cdot)$, and $\mathcal{A}_{\mathrm{stat}}(\cdot)$ are called Airy_1, Airy_2, $\mathrm{Airy}_{\mathrm{stat}}$ processes (Table 2.1) [53, 66, 68–73].

Understanding the time correlation, on the other hand, has long been a challenging problem. As noted in the next subsection, indeed it was the experiments [36] that suggested the scaling laws for the time covariance [Eq. (2.20)] with geometry dependent exponents, which were later confirmed by exact solutions for the TASEP [74]. Recently, analytical forms of the two-time joint probability have been obtained from several approaches [75–79], including rigorous exact solutions [76, 77]. Particularly, the formula in [78, 79] was compared with the experimental results and found to be consistent [78].

2.1.2 Liquid crystal experiment

With the exact solutions, it is natural to ask if the geometry-dependent universal fluctuations are relevant also in real experimental systems, or is a consequence of a special feature of the solvable models. This question was clearly answered by experimental studies by K. A. Takeuchi, M. Sano and collaborators [34–36], which investigated an interface growth phenomena in electrically-driven chaotic convection of nematic liquid crystal (LC) confined in quasi-two-dimensional space.

In the experiments, they applied a voltage to the LC sample confined between electrodes separated by spacers [Fig. 2.1(a)], and investigated interface growth of a cluster of a turbulent state (or more precisely, spatiotemporal chaos with short-ranged spatial and temporal correlation) called the dynamic scattering mode 2 (DSM2), which invades another turbulent state, DSM1, with sufficiently high voltage [34, 80, 81] (See also Sec. 3.1.1). As shown in Fig. 2.1(c,d), the DSM1 and DSM2 can be distinguished by the difference in their light transmittances, which is due to high density of the topological defect threads in the DSM2 [Fig. 2.1(b)] [80, 82, 83] (also see [84]) accompanied by a breaking of the anchoring on the electrode [81, 85, 86]. They nucleated the initial DSM2 cluster by shooting ultraviolet (UV)

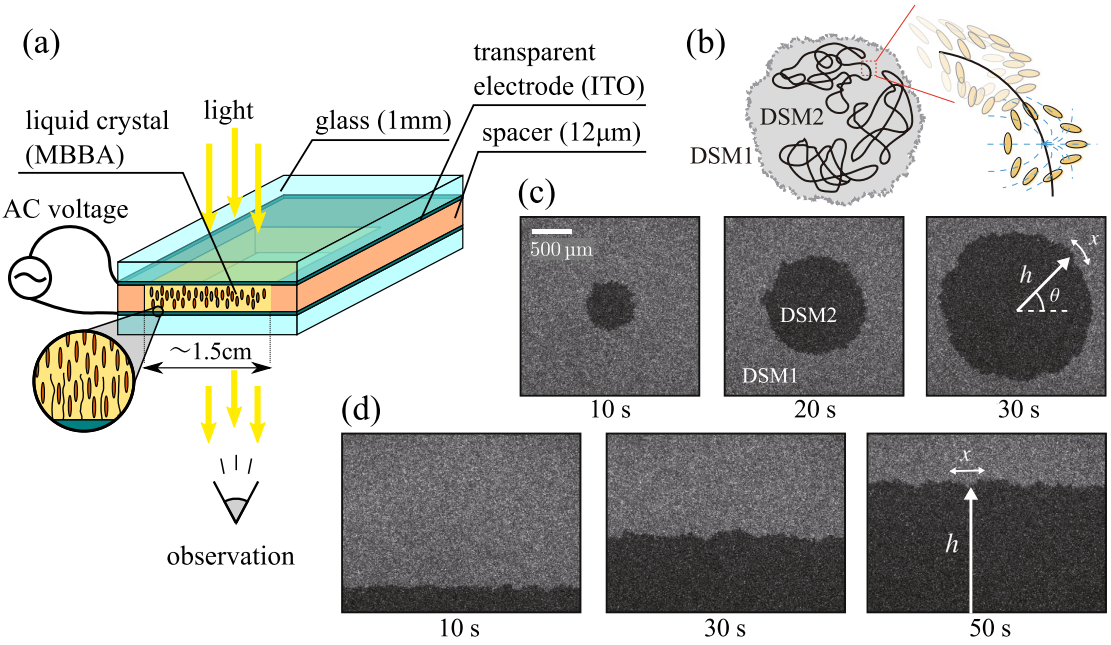

Figure 2.1: (a) Schematic of the LC cell. ITO: indium tin oxide, MBBA: *N*-(4-Methoxybenzylidene)-4-butylaniline, AC: alternative current. The ellipses illustrates the director field of the LC without voltage. The magnified view illustrates the homeotropic anchoring, which makes the director field perpendicular to the electrode. (b) Schematic of the difference between DSM1 and DSM2, illustrating that DSM2 consists of high density of topological defect in the LC sample. (c,d) Raw image of a circular (c) and flat (d) DSM2 interface growing in DSM1 [24, 35, 36]. The time after shooting the UV laser is indicated in each image. The definition of the height h and the position x is illustrated in the rightmost image. (b-d) are adopted from Ref. [24, 36] with permission of Springer and Elsvier with modifications.

laser pulses focused on a point (a line) and investigated circular (flat) interfaces, respectively.

As summarized in Fig. 2.2, these interfaces exhibited distinct geometry-dependent properties, which have been exactly derived for simple models as described [35, 36]. More precisely, they measured the rescaled height

$$q(x',t) := \frac{h(x,t) - v_\infty t}{(\Gamma t)^{1/3}} \simeq \chi(x',t) \tag{2.16}$$

$$x' = x/\xi(t) = \frac{Ax}{2}(\Gamma t)^{-2/3} \tag{2.17}$$

for the flat (circular) interfaces, and found that the one-point distributions of $q(x',t)$ agree with the GOE (GUE)-TW distributions [Fig. 2.2(a)], respectively, with the cumulants $\langle q^k \rangle_c$ ($k = 1, \ldots, 4$) converging to those of the exact values [Fig. 2.2(b); the convergence is algebraic as

shown in Ref. [36]]. Also, the spatial covariance of the flat and circular interfaces

$$C_s(\zeta, t) := \mathrm{Cov}[q(x' + \zeta, t), q(x', t)] \tag{2.18}$$

agreed with those of the Airy_1 and Airy_2 processes, $\mathrm{Cov}[\mathcal{A}_1(x' + \zeta), \mathcal{A}_1(x')]$ and $\mathrm{Cov}[\mathcal{A}_2(x' + \zeta), \mathcal{A}_2(x')]$, respectively [Fig. 2.2(c)]. They also found that the temporal covariance

$$C_t(t, t_0) := \mathrm{Cov}[q(x', t + t_0), q(x', t_0)] \tag{2.19}$$

has a scaling form

$$C_t(t, t_0) \simeq F(t/t_0) \sim (t/t_0)^{-\bar{\lambda}} \tag{2.20}$$

with a certain function $F(\cdot)$ and the different exponents $\bar{\lambda} = 1$ (flat), $\frac{1}{3}$ (circular). This difference in the exponents leads to the even qualitative difference between the flat and circular interfaces, with non-vanishing temporal correlation with

$$\tilde{C}_t(t, t_0) := \mathrm{Cov}[h(x, t + t_0), h(x, t)] \simeq \mathrm{const.} \tag{2.21}$$

for the circular interfaces [Fig. 2.2(d)], which can be regarded as weak ergodicity breaking [24, 36, 87]. The further difference between the flat and circular interfaces found in the experiments are described in Ref. [36].

The experimental results, overall, demonstrated that the geometry-dependent statistical properties are not only for theoretical models, but of great physical relevance as it appears in an experimental system, highlighting the universality of the geometry-dependent fluctuations.

2.1.3 Universality subclasses

The numerical, theoretical, and experimental evidence, overall, established the idea of the geometry-dependent flat and circular *universality subclasses* for the KPZ class [24, 33], which are defined by the same scaling exponents yet different universal stochastic variables $\chi(x', t)$ governing the asymptotic fluctuation. Especially, the flat, circular, and stationary subclasses (Table 2.1) are regarded as canonical subclasses [24, 33] [4].

The geometry-dependent universal fluctuations were also found in, e.g., universality class for interface growth called nonlinear molecular beam epitaxy class [96] and absorbing phase transitions [97], implying that the geometry dependence is a ubiquitous feature of some universality classes. We anticipate that the knowledge for the geometry-dependent fluctuation of the KPZ class help us understand other cases in future.

[4] We note that there are cases where $\chi(x', t)$ shows statistical properties which are not included in Table 2.1. For example, the Gaussian symplectic ensemble Tracy–Widom distribution can appear for KPZ interfaces typically with half-space boundary conditions [32, 88–95]

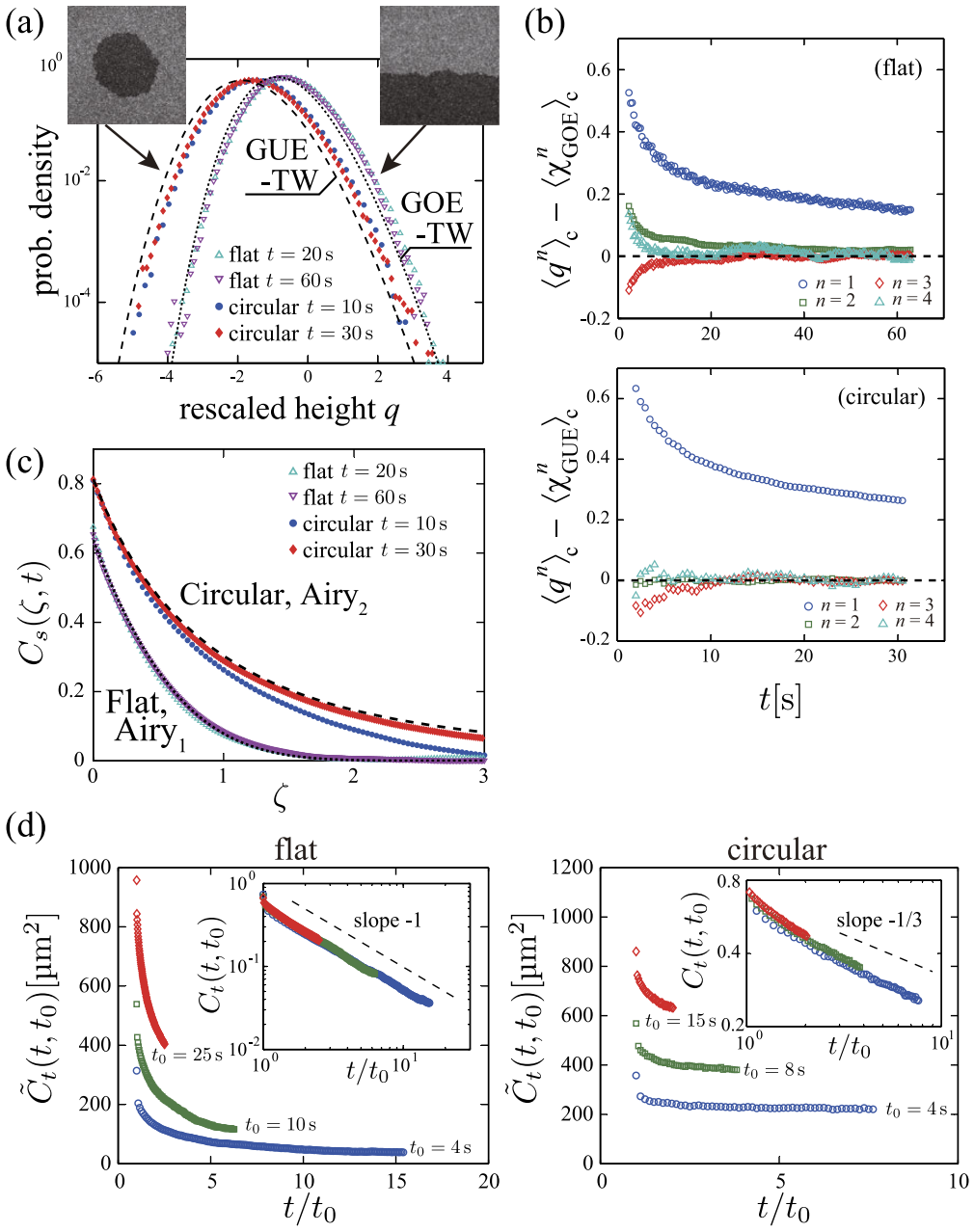

Figure 2.2: A part of the results of the LC experiments by K. A. Takeuchi *et. al.* [34–36], adopted from Ref. [36] with permission of Springer with modification of the notations. (a) The histogram of the rescaled height q. The exact solutions, GOE-TW (flat) and GUE-TW (circular) distributions are plotted by the broken and dotted lines, respectively. (b) The difference between the cumulants $\langle q^k \rangle_c$ $k = 1, \ldots, 4$ of the rescaled height of the flat/circular interfaces and those of the exact solutions $\langle \chi_1^k \rangle_c / \langle \chi_2^k \rangle_c$. (c) The spatial covariance of the rescaled height $C_s(\zeta, t)$. The exact solutions, Airy$_1$ covariance (flat) and Airy$_2$ covariance (circular) are plotted by the broken and dotted lines, respectively. (d) The temporal covariance of the rescaled height $C_t(t, t_0)$ (inset) and the covariance of the height $\tilde{C}_t(t, t_0)$ (main plot). The values of t_0 are indicated near the rightmost point of each series. In the insets, the guides for the eyes with the exponent $-\bar{\lambda}$ are indicated by the dashed lines.

2.1.4 Motivations

With the exact solutions and clear experimental realizations, the (1+1)D KPZ class can be regarded as a crucial example to reveal the origin and generality of the geometry-dependent universal fluctuations. In order to further integrate the knowledge obtained so far and acquire a comprehensive picture that can explain the geometry-dependent universality, we need to understand the fluctuations with a broader class of initial conditions, which, however, remains to be investigated in detail in contrast to the canonical cases described in the previous subsection.

In this study, we aimed to experimentally and numerically extend our knowledge toward interfaces with more general initial conditions than those investigated so far. With this aim, I constructed an experimental setup which enables us to investigate the interface fluctuation of a growing DSM2 cluster (see Sec. 2.1.2) with arbitrarily designed initial conditions. Using this system, we studied interfaces growing inward or outward from initial conditions with the shape of a circular ring (Fig. 2.4). These initial conditions are experimentally natural initial conditions appearing in, e.g., bacterial colony growth [8, 97, 98] and coffee rings [14], yet our knowledge on the properties of whose universal fluctuation is still limited [5]. I also carried out numerical Monte-Carlo simulations of an off-lattice model in the KPZ class [101] to elucidate universal properties of the KPZ interfaces with this initial condition. The following list further explains our motivations to study the ring-shaped initial conditions:

- Investigating the ingrowing interfaces provides as an opportunity to clarify whether the sign of the curvature is relevant for the asymptotic fluctuation, enabling us to infer relevant parameters that determine the universal subclasses.

- For the outgrowing interfaces, one can expect a temporal crossover (or a transition) connecting the Tracy-Widom distributions (and the corresponding spatial and temporal correlations of the flat and circular subclasses), which may be an interesting object even in a different field.

- Generally in experiments, a large number of samples enables us to elucidate detailed properties of $\chi(x', t)$ with accuracy. In this sense, investigating the cases with the circular ring-shaped initial conditions is a good starting point, since one can make use of the rotational invariance to take the positional average as well as ensemble average to achieve high accuracy.

In the course of study, we found that a representation of the height distribution called the variational formula [52, 102], which is recently developed with the aim of describing the general cases, can explain nontrivial behavior of the statistical properties of the interfaces we observed, (Sec. 2.4). This representation further allows us to predict the statistical properties of $\chi(x', t)$ for general interfaces with curved initial conditions.

[5] The skewness and kurtosis of the GUE-TW distribution have been reported in the coffee-ring experiment [14], in which the interfaces grow inward from a circular ring. Also, numerical studies on analogous geometries have been conducted almost simultaneously with our study [99, 100], as we note in Sec. 2.5

2.2 Experimental and numerical procedures

In order to investigate the interface fluctuations with the ring-shaped initial conditions, I conducted experiments with the LC electroconvection and simulations of the isotropic interface model called the off-lattice Eden model. In this section, I describe the experimental and numerical setups and procedures which we employed.

2.2.1 Experimental setup

Liquid-crystal cell preparation

As in the previous studies [34–36], I prepared LC cells consisting of two glass plates coated with transparent electrodes of made by a $\approx 100\,\mu$m layer of indium tin oxide, separated by spacers of $12\,\mu$m thickness [Fig. 2.1 (a)]. The electrodes were coated by *N*,*N*-dimethyl-*N*-octadecyl-3-aminopropyltrimethoxysilyl chloride to obtain the homeotropic alignment. The LC sample, *N*-(4-Methoxybenzylidene)-4-butylaniline (MBBA) doped with 0.01 wt % of tetra-*n*-butylammonium bromide, was introduced to a $1.5\,\text{cm} \times 1.5\,\text{cm}$ area enclosed by the spacers by the capillary effect.

I used different LC cells for the experiments investigating the ingrowing and outgrowing interfaces. In order to characterize properties of the cells, I measured the cutoff frequency f_c [103], the frequency characterizing the maximum timescale with which the ion flow can respond to the electric field. The values are found to be $f_c \approx 1.7 \times 10^3\,\text{Hz}$ for both cells used in the experiment. We also measured the minimum voltage with witch DSM2 can exists at 500 Hz, which was roughly 20 V for both of the cells. Though those parameters were not (at least apparently) different between the cells, we note that there are slight differences in the conditions between the cells as one can see in the difference in the non-universal parameters and the finite time effects for the interface growth (Sec. 2.3.2).

Laser holographic technique for arbitrary-shaped initial conditions

As demonstrated in Ref. [35, 36] (Sec. 2.1.2), the initial condition of the DSM2 interfaces can be controlled by controlling the amplitude profile of the UV laser at the LC cell. In this study, I constructed an optical setup [Fig. 2.3(a)] which enables us to design the amplitude profile of the UV laser at the LC cell into arbitrary shapes [as demonstrated in Fig.2.3(b)], using a device called the spatial light modulator (SLM).

The SLM is a device capable of spatially and temporally varying modulation of the light. One can find its application in various fields ranging from femtosecond laser pulse shaping [104] to optical tweezers [105]. In this study, we used the LCOS-SLM X10468-05 (Hamamatsu Photonics), which enables us to modulate the phase of the reflecting UV light with the wavelength $\lambda = 355\,\text{nm}$ at the resolution of 792×600 pixels by controlling the nematic alignment of the LC by a grid of electrodes. As shown in Fig. 2.3(a), UV laser beam [pulse beam with the width of 4-6ns, the third harmonics (the wavelength $\lambda = 355\,\text{nm}$) of the neodymium-doped yttrium aluminum garnet (Nd:YAG) laser beam, extracted by a

band-pass filter] was first expanded to $\approx \varnothing 1.5\,\mathrm{cm}$ by a beam expander and reflected by the SLM device, whose head size is $12\,\mathrm{cm} \times 16\,\mathrm{cm}$. The reflected beam is then focused at the LC cell by a convex lens with the focal length $f = 250\,\mathrm{mm}$.

We utilized this device as follows to realize the arbitrary initial condition of the DSM2. Let us denote the electric field of the laser light before the reflection at the position (x, y) by $E_0(x, y)e^{-\mathrm{i}\omega t}$, where the two-dimensional coordinate is defined perpendicularly to the light direction. The electric field after the phase modulation $E_0'(x, y)$ is approximately written as

$$E_0'(x, y) \propto E_0(x, y) \exp\left\{-\mathrm{i}\left[\omega t + \phi(x, y)\right]\right\} \tag{2.22}$$

where ω is the frequency of the laser light and $\phi(x, y)$ is the phase modulation by the SLM. Then, let us consider putting a convex lens with the focal length f and let the modulated light go through it. With the Fresnel approximation, the electric field we obtain at the focus of the lens is written as [106]

$$|E(x, y)| = \left| \frac{1}{\mathrm{i}\lambda f} \iint \mathrm{d}x_0 \mathrm{d}y_0 E_0'(x_0, y_0) \exp\left[\frac{2\pi\mathrm{i}}{\lambda f}(x x_0 + y y_0)\right] \right| \tag{2.23}$$

$$\propto \left| \iint \mathrm{d}x_0 \mathrm{d}y_0 E_0(x_0, y_0) \exp\left[-\mathrm{i}\phi(x_0, y_0)\right] \exp\left[\frac{2\pi\mathrm{i}}{\lambda f}(x x_0 + y y_0)\right] \right|, \tag{2.24}$$

where $\lambda = \frac{2\pi c}{\omega}$ is the wavelength of the light.

Equation (2.24) lets us expect that one can achieve a light profile with a desired amplitude by solving the optimization problem to adjust the modulation profile $\phi(x, y)$ so that the amplitude $|E(x, y)|$ is close to the designed one. Assuming that the incoming laser beam is a plain wave ($E_0(x_0, y_0) = \text{const.}$), this reduces to the problem to find $\phi(x, y)$ to give the desired $|E(x, y)|$ after the Fourier transformation, which can be efficiently solved by an algorithm called iterative Fourier transform algorithm (IFTA) [107, 108]. In this study, I performed the IFTA with 100 iterations to obtain the modulation profile $\phi(x, y)$ output to the SLM.

Technically, one needs to avoid the nucleation of the DSM2 by light reflected without the phase modulation, e.g., that reflected at the surface of the device where the refractive index largely changes. In our study, this problem was solved by shifting the effective focal distance of the lens only for the phase-modulated light, by superimposing a phase difference equivalent to a convex Fresnel lens at the SLM.

Initial conditions

With the constructed experimental setup, we studied the interfaces growing inward or outward from the ring-shaped initial conditions, as exemplified in Fig. 2.4(a). I conducted two sets of the experiments, using different LC cells, in each of which I investigated either of the ingrowing and outgrowing growth as summarized in Table 2.2. In the first set of the experiments, the interfaces with the radius of the initial condition of $R_0 = 1342\,\mu\mathrm{m}$, $1241\,\mu\mathrm{m}$ and $826\,\mu\mathrm{m}$, and flat interfaces with a line-shaped initial condition was investigated. The length of the line for the flat interfaces was $\approx 8\,\mathrm{mm}$ and we observed the region around the center

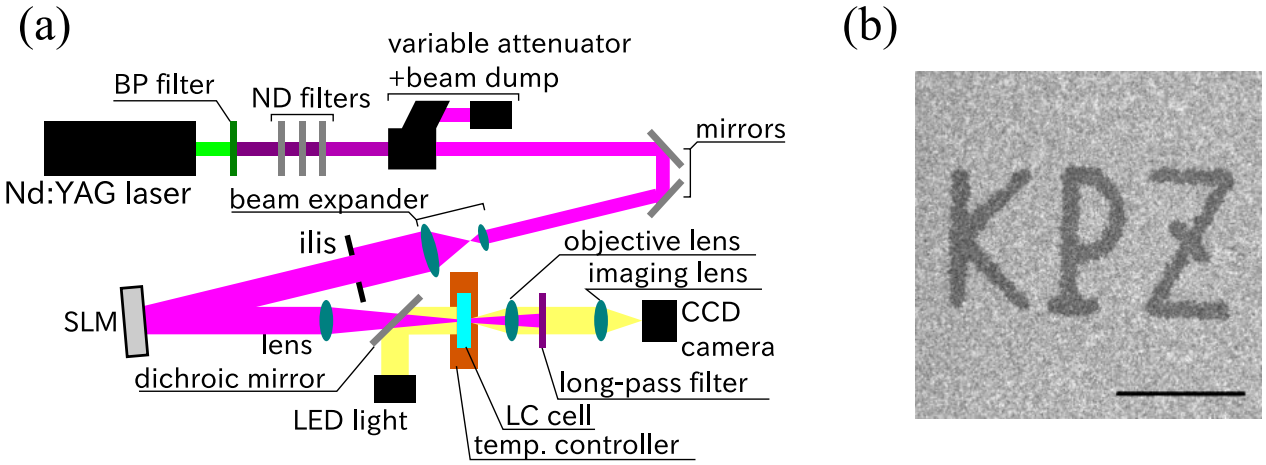

Figure 2.3: (a) Schematic of the optical setup. Nd:YAG: neodymium-doped yttrium aluminum garnet, SLM: spatial light modulator, CCD: charge-coupled device camera, LED: light-emitting diode. The whole setup is placed in an isothermal chamber as described in the text. (b) An image of DSM2, growing from a "KPZ" initial condition as a demonstration of the holographic technique. The scale bar is 1 mm.

of the line with the span-wise length $\approx 4\,\mathrm{mm}$. In the second set of the experiments, the interfaces with the radius $R_0 = 219\,\mu\mathrm{m}$ and $366\,\mu\mathrm{m}$, flat interfaces with the same condition as the first set of the experiments, and the circular interfaces with the point initial condition was investigated. We automated the experiment and observed $\gtrapprox 1000$ realizations for each initial condition (Table 2.2). The shape of generated DSM2 clusters had a deviation from the designed shape in the order of $10\,\mu\mathrm{m}$, but we think this deviation is irrelevant for the asymptotic height fluctuation [6].

Image acquisition

For each realization, I applied 500 Hz 31 V AC voltage to the cell, shot UV laser pulses to generate the initial DSM2 cluster, and recorded the images of the LC cell through the transmitted light at 5 frames per second by a charge-coupled device (CCD) camera (IGV-B1620M, Imperx) equipped with a 4x objective lens (UPlanFLN 4X,Olympus) and an imaging lens with the focal length $f = 120\,\mathrm{mm}$ [Fig. 2.3(a)] [7]. After the acquisition, the voltage was turned off and the LC cell relaxed to the initial state. The observation area was about $3\,\mathrm{mm} \times 4\,\mathrm{mm}$ and the resolution was $2.68\,\mu\mathrm{m}$/pixel. The energy of the laser pulse was adjusted so that it is as low as possible while sufficient to create the DSM2 cluster ($\lessapprox 0.7\,\mathrm{mJ}$ for the ingrowing and flat interfaces, and $\lessapprox 0.4\,\mathrm{mJ}$ for the outgrowing and circular interfaces). During the experi-

[6] Intuitively, because the fluctuation amplitude and the correlation length diverge, the fluctuation of the initial conditions are overwhelmed by the growing spontaneous fluctuation. Indeed, the variational formula (Sec. 2.4.1) suggests that the initial fluctuation with a fixed amplitude is irrelevant for the asymptotic fluctuation.

[7] A dichroic mirror (HOTM-25.4C3.3, Sigma Koki) was placed in front of the CCD camera in order to cut the UV laser to avoid the damage to the camera.

Table 2.2: Experimental conditions and non-universal parameters.

initial condition	# of samples	v_∞(μm/s)	Γ(μm^3/s)
flat(ingrowing experiment)	1273	31.08(1)	$1.74(8) \times 10^3$
$R_0 = 1342\,\mu$m, ingrowing interfaces analyzed	1721	31.75(5)	$1.52(8) \times 10^3$
$R_0 = 1241\,\mu$m, ingrowing interfaces analyzed	2235	33.52(5)	$1.43(7) \times 10^3$
$R_0 = 826\,\mu$m, ingrowing interfaces analyzed	1830	33.23(4)	$1.45(7) \times 10^3$
line (outgrowing experiment)	1417	30.84(2)	$1.25(2) \times 10^3$
point (outgrowing experiment)	941	29.68(3)	$1.31(4) \times 10^3$
$R_0 = 366\,\mu$m, outgrowing interfaces analyzed	1936	30.84(2)*	–
$R_0 = 219\,\mu$m, outgrowing interfaces analyzed	1521	30.60(2)*	–

* Estimated by fitting the last point of the mean rescaled velocity $\langle p \rangle$ against the result of the Eden model (see the main text).

ment, the cell was placed in a temperature controller, which is an aluminum block whose size is 12 cm × 8 cm × 2.2 cm equipped with a thermistor and Peltier devices. The temperature of the block was maintained at 25 °C by the PID control with the temporal fluctuation of $\approx \pm 0.01$ °C. The whole experimental setup, including the optics, was contained in an isothermal chamber covered by heat insulating material, in which the temperature is maintained at 25 °C by circulating temperature-controlled water in copper pipes in the chamber.

Image processing and definition of height

The shape of the interface was extracted by thresholding. In order to reduce the effect of the illumination inhomogeneity, I used position-dependent thresholds. At each pixel (i, j), I obtained the probability distribution function of the intensity $I_{\rm DSM1}(i, j)$ and $I_{\rm DSM2}(i, j)$ for the DSM1 and DSM2, respectively [Fig. 2.5 (a)], using the images before shooting the UV laser (for DSM1) and those after the DSM2 occupies the whole area of the observation (for DSM2). There is an overlap between the probability distribution functions, which inevitably leads to a non-zero probability of misclassification [Fig. 2.5 (b,c)]. However, I empirically found that by choosing the threshold $I_{\rm th}$ so that $\mathrm{Prob}\,[I_{\rm DSM1}(i, j) < I_{\rm th}] = r\mathrm{Prob}\,[I_{\rm DSM2}(i, j) > I_{\rm th}]$ where r is a constant manually adjusted to 0.5 and smoothing out the structures smaller than the typical length scale of the DSM2 $\approx 12\,\mu\mathrm{m}/\sqrt{2}$ [37, 80, 82], one can extract the boundary between the DSM2 and DSM1 which is reasonably close to that distinguished by one's eyes, with small amount of artifact fluctuation by misclassification [Fig. 2.5 (b,d)]. The small change in the value of r did not change our conclusions.

The height $h(x, t)$ for the interfaces with the ring-shaped initial conditions was defined as follows. I first determined the center of the initial ring, using the ensemble average of the images taken at the first frame used in the analysis. Then, $h(x, t)$ was defined as the radial displacement from the initial ring and x was measured along the circumference whose radius is equal to the mean radius of the interfaces at time t [Fig. 2.4(a)]. If there is an overhang [Fig. 1.2(a)], the height is defined as the averaged distance between the pixels on the interface and the center. The time t was defined as the elapsed time after shooting the

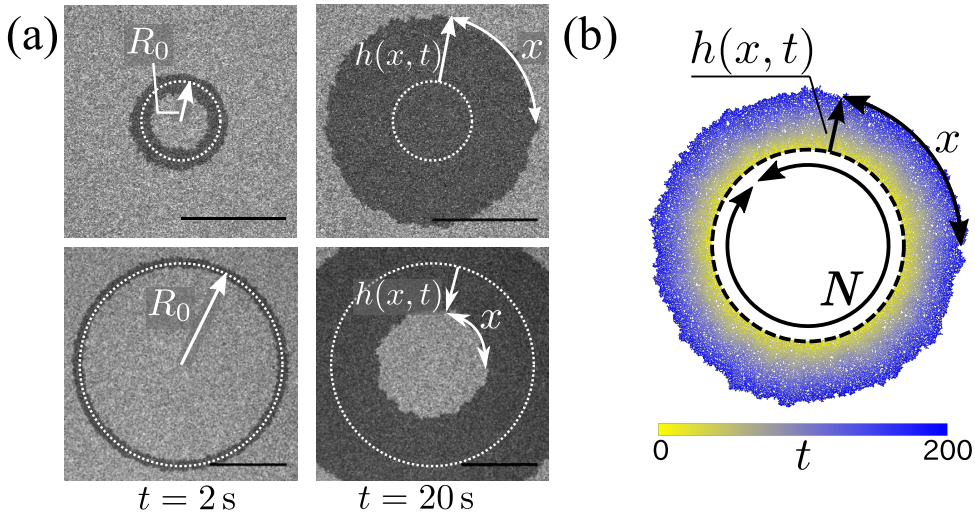

Figure 2.4: The examples of the interfaces and the definition of the heights. (a) The LC experiment. Images of DSM growing from $R_0 = 366\,\mu\mathrm{m}$ and $R_0 = 1342\,\mu\mathrm{m}$, whose heights of the outgrowing and ingrowing interfaces are measured, are shown in the upper and lower rows, respectively. The elapsed times after shooting the laser is indicated below each columns. The dotted lines indicate the initial ring estimated as described in the text. The scale bars are 1 mm. (b) The Eden model. A cluster growing outward from a ring with the initial number of the cells $N = 1000$ is shown. The time step of the cell creation is indicated by the color. The dotted line indicates the initial condition.

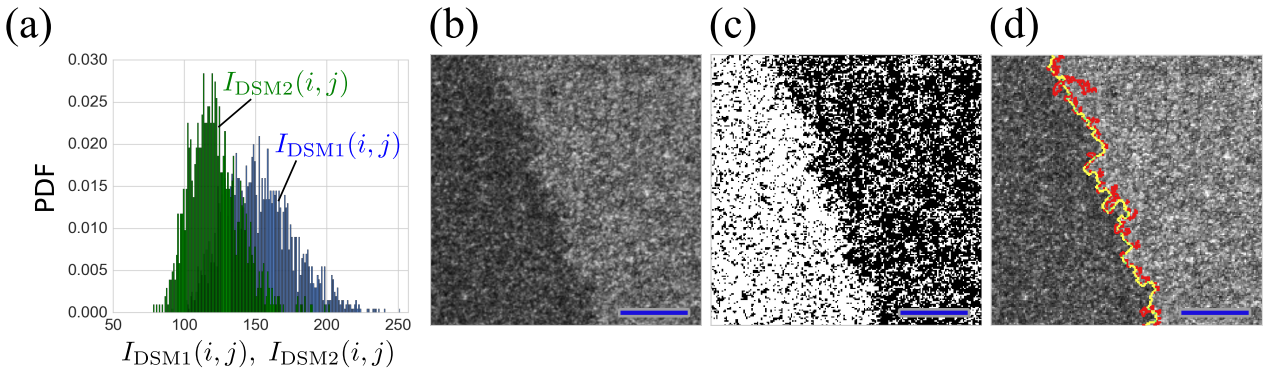

Figure 2.5: The example of the thresholding. (a) Probability distribution function (PDF) for the transmitted light intensity of the DSM1 $I_{\mathrm{DSM1}}(i,j)$ and the DSM2 $I_{\mathrm{DSM2}}(i,j)$. (b) Original image before thresholding. (c) Image after thresholding. (d) The interface detected by thresholding with (yellow line) and without (red line) the smoothing. For (b-d), the scale bar is 50px $\approx 134\,\mu\mathrm{m}$.

Table 2.3: Parameters for the Eden model.

growth direction	outgrowing						
N	100	500	1000	4000	10000	20000	40000
# of samples	16000	7200	3600	10400	1000	3200	3200
growth direction	ingrowing						
N	8000	16000	32000	100000			
# of samples	2400	3200	3200	1600			

UV laser initiating the DSM2 cluster. The height was analogously defined for the flat and circular interfaces.

2.2.2 Numerical model

In order to avoid anisotropy induced by the background lattice structures [109, 110], I used an off-lattice version of the Eden model introduced in Ref. [101], growing inward or outward from the ring-shaped initial conditions [Fig. 2.4(b)]. In the simulations, circular particles (with the diameter one) were stochastically added to form a cluster. The simulations were initiated with a circular ring formed by N particles, and proceeded as follows:

1. Randomly choose a parent particle at the interface of the cluster.
2. Put a new particle in a random direction in touch with the parent particle, only if there are no overlapping particles with the new particle.
3. Increase the time by 1/(the number of the particles at the interface).

The interface was defined as the loop of the connected particles wrapping the cluster, where two particles are regarded as connected if the distance between them is smaller than $\sqrt{3}$, since the particles inside the loop cannot interfere the particles outside the loop [101]. As in the experiments, the height $h(x,t)$ was measured as the radial displacement of the particles at the interface from the initial circle, and the position x was measured along the circumference whose radius is the same as the averaged distance between the origin and the particles at the interface [Fig. 2.4(b)]. The initial radius R_0 is defined as $R_0 := N/2\pi$. The parameters used in the simulations are summarized in Table 2.3. For the flat interfaces, I simulated the growth of the same model, with the initial condition of a line formed by 25000 particles with the periodic boundary condition in the spanwise direction, with the number of the samples set to be 3200.

In order to efficiently conduct the simulations for large clusters, I optimized the algorithm in several ways. For example, each particle was equipped with a list of the intervals of the direction in which a new daughter particle can grow, which is updated at a time a new particle is added nearby the particle. Also, a particle has a list of particles closer than $\sqrt{3}$, stored with their relative orientations, which enables us to identify the interface effectively. The stored particle positions P_i were sorted by $\theta_i := \angle P_i O X$, where O is the origin $(0,0)$ and

$X = (1, 0)$, and when a new particle is added to the position P, the distance with a particle P_i is evaluated only if the angle $|\angle POP_i|$ is sufficiently small to avoid unnecessary computations. The particles that cannot contribute to the further growth process were excluded from the simulation every time when the interface is identified.

2.3 Results and analysis

2.3.1 Cumulants, skewness and kurtosis

To investigate how the fluctuation amplitude grows, I first evaluated the k-th cumulant of the height $\left\langle h(x,t)^k \right\rangle_c$ for $k = 1, 2, 3, 4$. Figure 2.6 and 2.7 show the experimental and numerical results, respectively. For the flat and circular interfaces, the scaling laws $\left\langle h(x,t)^k \right\rangle_c \sim t^{k/3}$ expected from the scale invariance of the KPZ class (1.11), are clearly observed for the flat and circular interfaces, consistent with the earlier results [34–36]. On the other hand, for the interfaces growing from the ring-shaped initial conditions, the slopes for the variance $\langle h^2 \rangle_c$ are slightly but clearly different from those of the flat and circular interfaces. As shown in the following, we think this does not mean that the height is no longer described by Eq. (2.5), but is due to the temporal change of the stochastic variable $\chi(x', t)$ itself.

To further elucidate the statistical properties of the one-point height distribution of $\chi(x', t)$, I then evaluated the skewness $\mathrm{Sk}[h(x,t)] := \langle h^3 \rangle_c / \langle h^2 \rangle_c^{3/2}$ and the kurtosis $\mathrm{Ku}[h(x,t)] := \langle h^4 \rangle_c / \langle h^2 \rangle_c^2$ (Fig. 2.8), which converge to $\mathrm{Sk}[\chi(x,t)]$ and $\mathrm{Ku}[\chi(x,t)]$ assuming (2.5), respectively. In the LC experiments, the values for the flat and circular interfaces were close to those for the corresponding exact solutions, χ_1 (flat) and χ_2 (circular) [Fig. 2.8(a,b)] consistently to the earlier results [34–36]. Similarly, in the Eden model, the values for the flat interfaces were asymptotic to those of χ_1 as expected [Fig. 2.8(c,d)].

For the interfaces with the ring-shaped initial conditions, despite the large statistical error in the experimental results, one can observe clear trends common in the experimental and numerical results: First, in the ingrowing cases [Fig. 2.8(a,c)], the values do not approach to those of χ_2 (circular), but instead follow those of χ_1 (flat) at early time. The numerical data suggests that the values deviate from the result of the flat interfaces at timescale growing with N. The consistent behavior can also be observed in the experimental results. In contrast, in the outgrowing cases [Fig. 2.8(b,d)], the values of the skewness and kurtosis take the values between those of χ_1 and χ_2. In the numerical results, the values deviate from those of the flat interfaces at a timescale growing with N as in the ingrowing cases, and then approaches to the values of χ_2. Again, the experimental result was consistent with the numerical results, except the fact that the short-time values of the skewness and kurtosis of the outgrowing interfaces does not overlap on those of the flat interfaces. We avoid to draw a conclusion about this difference between the experimental and numerical results here, but this might be consequence of the relatively small diameter compared with the ingrowing experiments, assuming that the finite-time fluctuation itself is affected by the initial radius.

To summarize, the skewness and kurtosis suggest two distinct behaviors of the stochastic

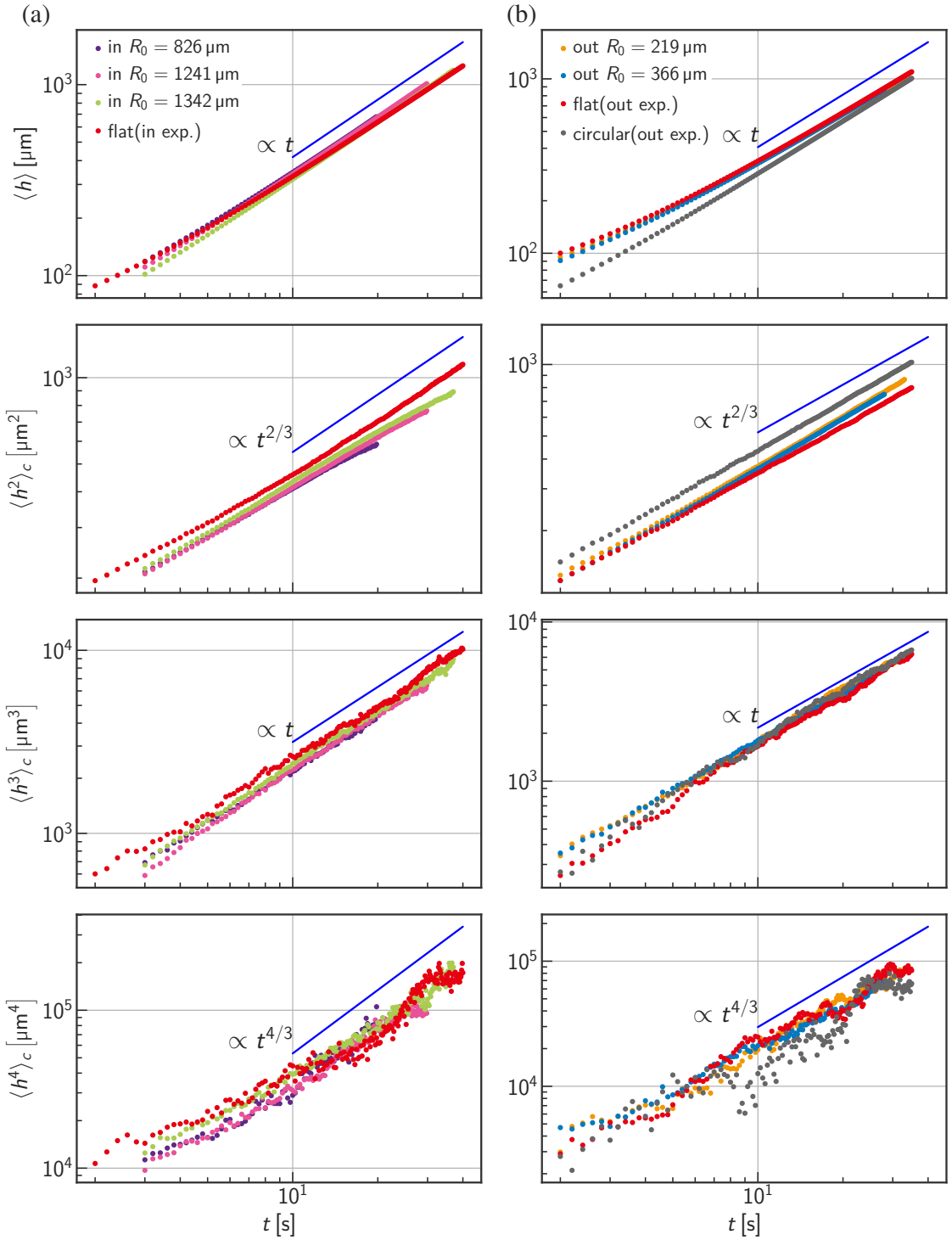

Figure 2.6: The cumulants of the height $h(x,t)$ one-point distribution for the LC experiment. The data for the ingrowing and outgrowing experiments are shown in (a) and (b), respectively. (Note that I conducted independent experiments with the flat initial conditions for the ingrowing and outgrowing cases.) The solid lines are guides for the eyes with the slope 1 for the mean $\langle h \rangle$ and the KPZ class exponents $k/3$ for the higher-order cumulants $\langle h^k \rangle_c$ $(k \geq 2)$.

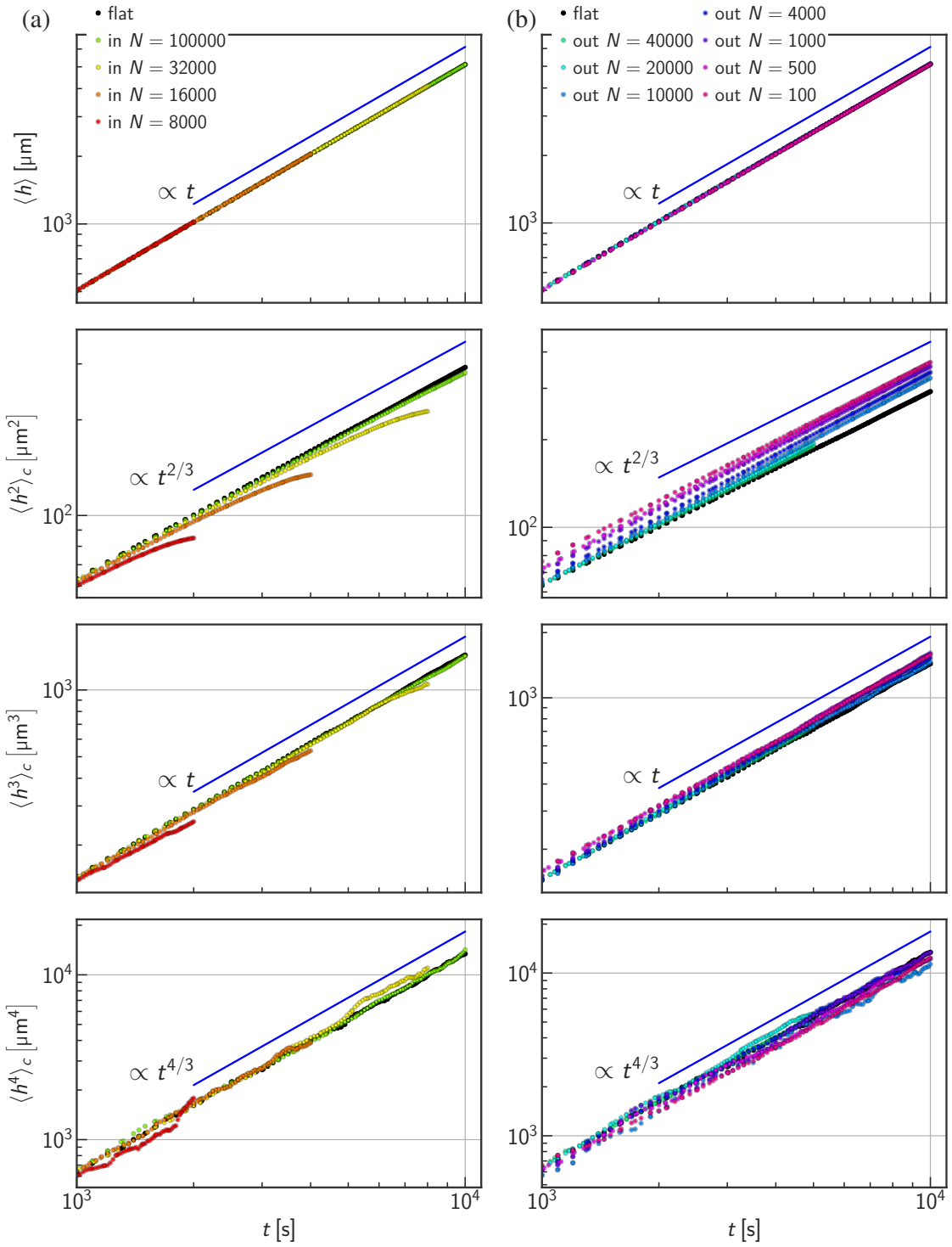

Figure 2.7: The cumulants of the height $h(x,t)$ one-point distribution for the Eden model. The data for the ingrowing and outgrowing experiments are shown in (a) and (b), respectively. The solid lines are guides for the eyes with the slope 1 for the mean $\langle h \rangle$ and the KPZ class exponents $k/3$ for the higher-order cumulants $\langle h^k \rangle_c$ $(k \geq 2)$.

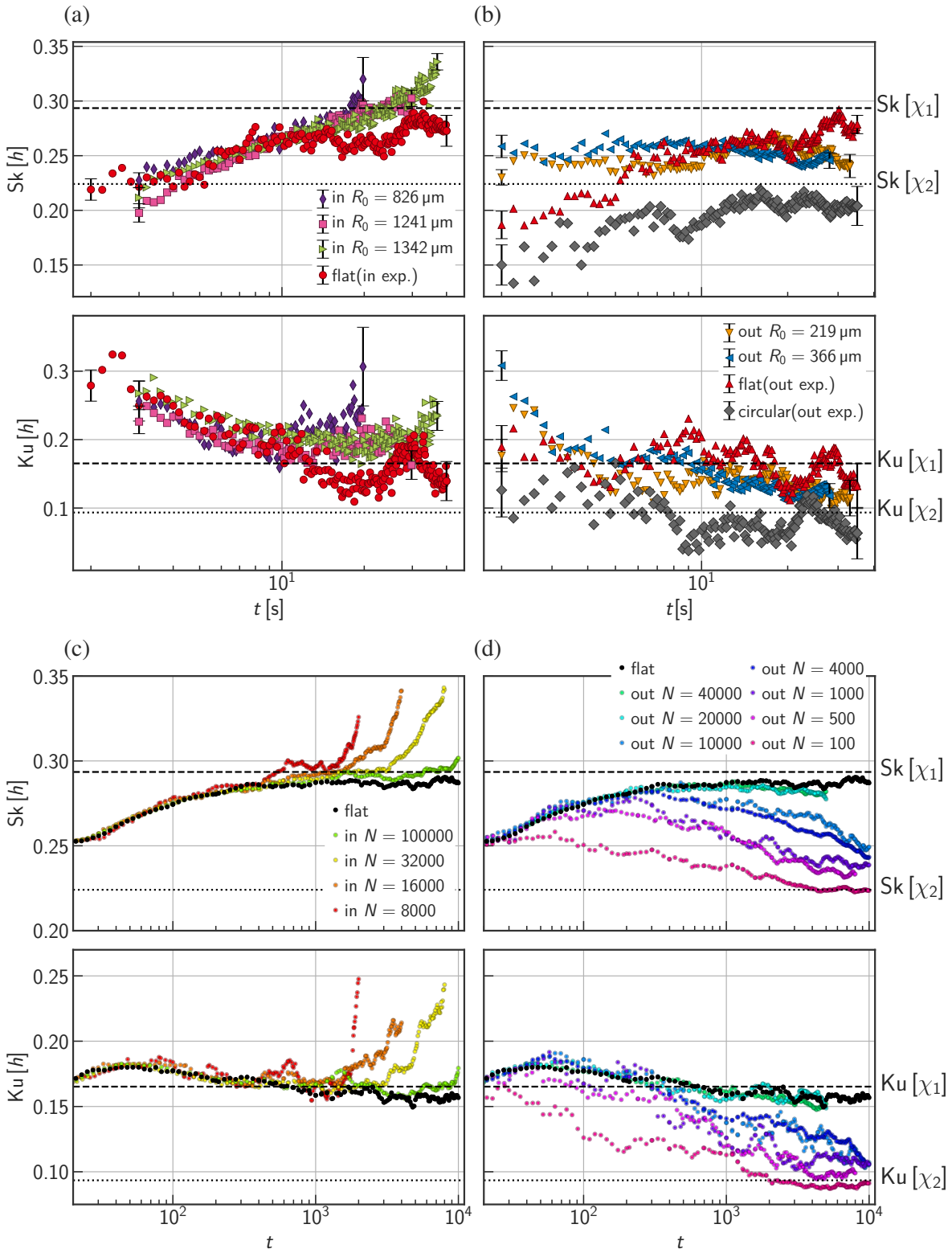

Figure 2.8: The skewness and kurtosis of the height $h(x,t)$ one-point distribution for (a,b) the LC experiment and (c,d) the Eden model. The values for the ingrowing and outgrowing interfaces are shown in (a,c) and (b,d), respectively. The values for χ_1 (flat) and χ_2 (circular) are shown by the dashed and dotted lines, respectively. For the experimental data (a,b), the statistical standard error is indicated by the error bars on the first and the last points.

variable $\chi(x,t)$ for the ingrowing and outgrowing interfaces. Those of the ingrowing interfaces show the deviation from the values of the flat interfaces at a characteristic time with no sign of the circular-subclass fluctuation χ_2. On the other hand, those of the outgrowing interfaces also seems to depart from the values for the flat interfaces at a characteristic timescale and approach to that of the circular interfaces. We compare the experimental and numerical results quantitatively in Sec. 2.3.4.

In the following subsections, to draw clearer conclusions, I turn our attention to the quantities with more statistical accuracy to elucidate the interface fluctuations with the ring-shaped initial conditions.

2.3.2 Estimation of the non-universal parameters

In order to access properties of the universal stochastic variable $\chi(x',t)$ with more statistical accuracy, one needs to estimate the non-universal parameters v_∞, Γ and A to rescale the height according to Eq. (2.5). In this section, I describe how I estimated the non-universal parameters in this study.

Isotropy and non-universal parameters

Though one needs to estimate the three independent parameters to rescale the scales of the time, length and height as noted in Sec. 2.1.1, only two parameters are necessary in an isotropic system, because of the relationship between the parameters [36, 111]

$$A = \sqrt{\frac{2\Gamma}{v_\infty}}. \tag{2.25}$$

This is because of the relation $v_\infty(s) = v_\infty\sqrt{1+s^2}$ for an isotropic system (Eq. (2.4)), which leads to $\lambda = v_\infty$. This relationship has been confirmed for the LC experiments [36, 111] and for the Eden model [101, 111].

Liquid crystal experiment

Flat and circular interfaces For the flat and circular interfaces, one can employ methods already developed to estimate v_∞ and Γ [17, 34–36], with assuming the asymptotic height is written as Eq. (2.5) with $\chi(x',t) = \chi_1(x')$ and $\chi_2(x')$, respectively. The results of the skewness and kurtosis (Fig. 2.8) suggests the validity of using this method. First, I estimated v_∞ by plotting $\partial_t \langle h(x,t)\rangle$ against $t^{2/3}$ and regressing by a line [Fig. 2.9 (a,b; left)], since

$$\partial_t \langle h\rangle \simeq v_\infty + \frac{\Gamma^{1/3}}{3}\langle\chi(x')\rangle\, t^{-2/3} \tag{2.26}$$

is expected from Eq. (2.5). We varied the upper limit of the fitting range $t_0^{-2/3}$, and found a range of t_0 in which the values of the intercept show a plateau [region between the broken

lines in Fig. 2.9 (a,b, right)]. We estimated the value of the v_∞ by averaging the value in the plateau, and the uncertainty δv_∞ as the maximum difference between the estimated value and the values in the plateau (Table 2.2).

For the other parameter, I estimated the parameter Γ by

$$t^{-2/3} \left\langle h(x,t)^2 \right\rangle_c \simeq \left\langle \chi^2 \right\rangle_c \Gamma^{2/3} , \tag{2.27}$$

expected from Eq. (2.5) [35, 36], where χ is χ_1 and χ_2 for the flat and circular interfaces, respectively [8]. More specifically, with expecting the finite-time effect (l.h.s.) $\simeq \langle\chi^2\rangle_c \Gamma^{2/3} + \mathcal{O}\left(t^{-2/3}\right)$ as observed in Ref. [36], I plotted $t^{-2/3} \langle h(x,t)^2 \rangle_c$ against $t^{-2/3}$ [Fig. 2.9(c-e)] and estimated the value of Γ as the intercept of the linear fitting, which is denoted by $\Gamma_{\rm ft}$ with the statistical uncertainty $\delta\Gamma_{\rm ft}$. I also estimated Γ just by averaging the value of $t^{-2/3} \langle h(x,t)^2 \rangle_c$ for $t \geq 30\,\mathrm{s}$, because it was not clear whether the slope I fitted is the true asymptotic one as one can see in Fig. 2.9(c-e). The value and the uncertainty estimated in this method is denoted by $\Gamma_{\rm ave}$ and $\delta\Gamma_{\rm ave}$. Finally, I simply estimated the value and the uncertainty Γ, $\delta\Gamma$ as

$$\Gamma = \Gamma_{\rm ft},\ \delta\Gamma = \max\left(\delta\Gamma_{\rm ft}, |\delta\Gamma_{\rm ft} - \delta\Gamma_{\rm ave}| + \max\left(\delta\Gamma_{\rm ave}, \delta\Gamma_{\rm ft}\right)\right) . \tag{2.28}$$

The estimated values are summarized in the Table 2.2.

The estimated values of v_∞ and Γ for each experiment are slightly different beyond the uncertainty. This may be because of the slight difference of the temperature, the material parameter or cell thickness depending on the position in the LC cell, or aging of the material as discussed in Ref. [36].

Interfaces with ring-shaped initial conditions As for the interfaces with the ring-shaped initial conditions, one cannot use the same method as the flat and circular interfaces because of the temporal change of the cumulant values $\left\langle \chi(x',t)^k \right\rangle_c$ discussed in Sec. 2.3.1. Therefore, I employed *ad hoc* methods to estimate the parameters on the basis of experimental observation.

As for the ingrowing interfaces, the short-time values of the skewness and kurtosis overlap on those of the flat interfaces [Fig. 2.8(a)], letting us expect that the cumulant values itself is close to those for the flat interfaces. With this observation, I estimated the values of v_∞ and Γ for the ingrowing interfaces so that the values of the cumulants at early time agree with those of the flat interfaces [9]. The estimated values are summarized in Table 2.2.

For the outgrowing interfaces, the short-time values of the skewness and kurtosis did not overlap on those of the flat interfaces (Fig. 2.8), making us doubt about the validity to use the same method as for the ingrowing interfaces. Thus, I simply used the value of v_∞ and Γ

[8] In principle, one can estimate the value for A directly from the definition (2.3) [17, 34]. However, the accurate estimation is challenging practically in the LC experiments [34], due to the slow convergence to the asymptotic height profile $\left\langle \left(h(x+l) - h(x)\right)^2 \right\rangle \simeq Al$ with respect to l.

[9] More precisely, first I defined a non-dimensional quantity

$$\alpha(\Gamma, t) := \left\langle h(x,t)^2 \right\rangle_c (\Gamma t)^{-2/3} \tag{2.29}$$

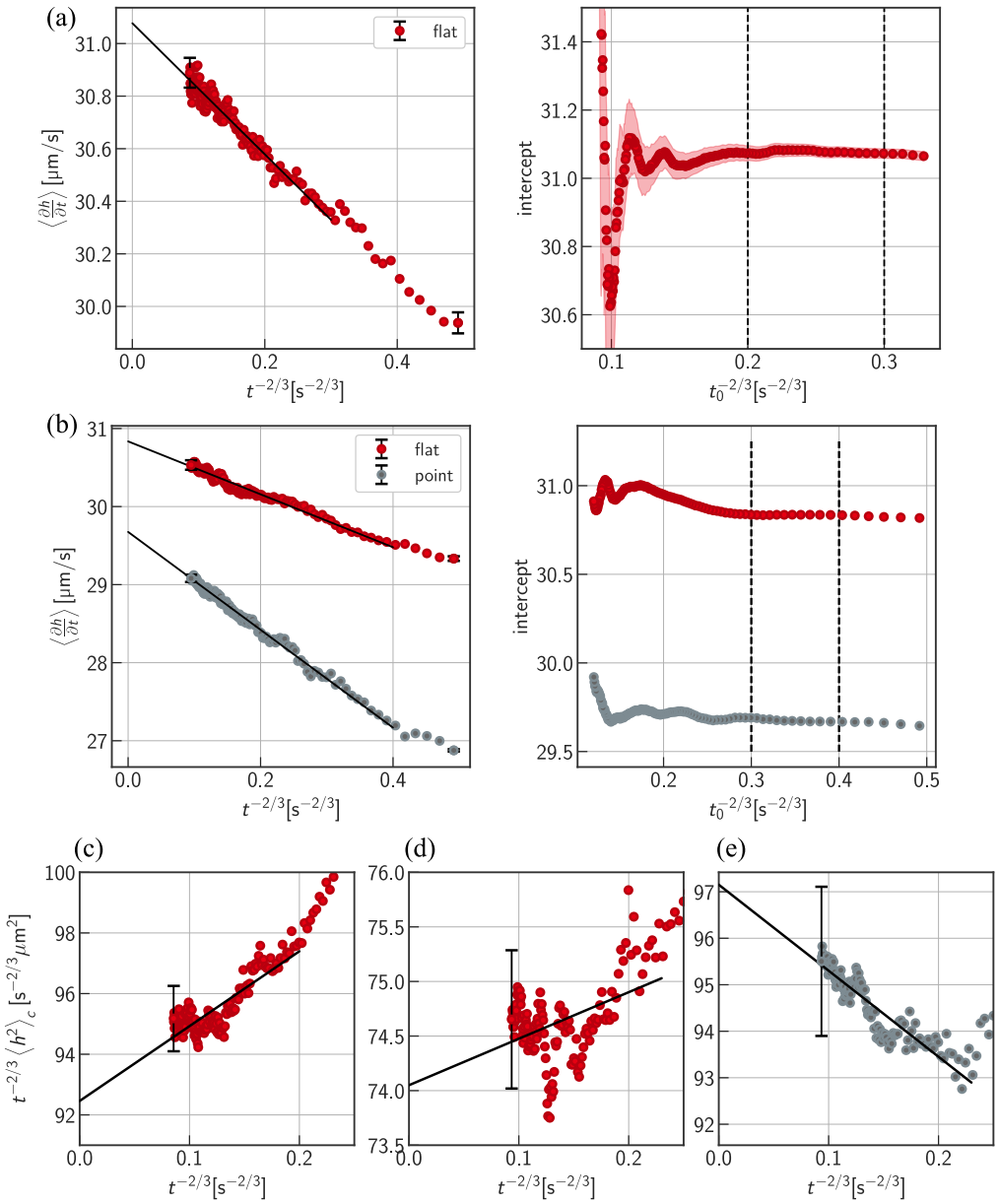

Figure 2.9: Non-universal parameter estimation for the LC experiment. (a,b) Estimation of v_∞ for the (a) ingrowing and (b) outgrowing interfaces. In the left plot, the velocity of the mean height $\left\langle \frac{\partial h}{\partial t} \right\rangle$ averaged for 2.25 s is plotted against $t^{-2/3}$. The statistical standard error is indicated by the error bars on the first and the last points. v_∞ is estimated as the value of the intercept of the line, regressed against the data with $t \leq t_0$ (see the main text). The black solid line is the regressed line. In the right plot, the value of the intercept with varied t_0 is plotted. The uncertainty of the v_∞ is estimated by the variation of the intercept with varied t_0 between the vertical broken lines. (c-e) Estimation of Γ for the (c) ingrowing and (d,e) outgrowing interfaces. The rescaled cumulant of the variance of the height $t^{-2/3} \langle h^2 \rangle_c$ is plotted against $t^{-2/3}$. The value of Γ assuming the finite time effect ($\Gamma_{\mathrm{finite-time}}$, see the main text) is estimated as the value of the intercept of the line, regressed against the data with $t \leq 0.2$ and $t \leq 0.23$ for the ingrowing and outgrowing interfaces, respectively. The black solid line is the regression line.

estimated for the flat interfaces. With considering the possible drift of the parameters, I estimated the uncertainty as $\delta v_\infty = \sqrt{\delta v_{\infty,\mathrm{drift}}^2 + \delta v_{\infty,\mathrm{flat}}^2}$ and $\delta\Gamma = \sqrt{\delta\Gamma_{\mathrm{drift}}^2 + \delta\Gamma_{\mathrm{flat}}^2}$, respectively, where $\delta v_{\infty,\mathrm{drift}}$ and $\delta\Gamma_{\mathrm{drift}}$ represents the difference of the values of v_∞ and Γ between the flat and circular interfaces, and $\delta v_{\infty,\mathrm{flat}}$ and $\delta\Gamma_{\mathrm{flat}}$ are the uncertainty for the flat interfaces. This estimation led to relatively large uncertainty in the estimation of v_∞, and I discuss the improvement with a further assumption in the Sec. 2.3.4.

Eden model

For the Eden model, I used the values estimated in Ref. [109] with large-scale simulation of circular interfaces, $v_\infty = 0.51371(2)$, $\Gamma = 1.00(1)$ and $A = \sqrt{2\Gamma/v_\infty} = 1.97(1)$ while using the values estimated in Ref. [101] does not alter our conclusions.

2.3.3 Rescaled cumulants

With the estimated parameters in the previous subsection, I calculated the rescaled height

$$q(x',t) := \frac{h(x,t) - v_\infty t}{(\Gamma t)^{1/3}} \simeq \chi(x',t) \tag{2.16}$$

$$x' = x/\xi(t) = \frac{Ax}{2}(\Gamma t)^{-2/3} \tag{2.17}$$

for the experimental and numerical results, and evaluated the cumulants $\left\langle q(x',t)^k \right\rangle_c$ for $k = 1, 2, 3, 4$.

The numerical results are shown in Fig. 2.10(a). Except for $\left\langle q(x',t)^4 \right\rangle_c$ which is too scattered to distinguish χ_1 and χ_2, behaviors analogous to those of the skewness and kurtosis (Fig. 2.8) is observed; The values of the cumulants for the interfaces with the ring-shaped initial conditions first follow those of the flat interface, and then depart at a characteristic timescale which increases as $N = 2\pi R_0$ increases. After the departure, the values for the

---

and determined the value of Γ so that it minimizes the deviation from the flat data at early times:

$$\int_{t_0}^{t_M} \left(\alpha(\Gamma,t) - \alpha_{\mathrm{flat}}(\Gamma_{\mathrm{flat}},t)\right)^2 \mathrm{d}t. \tag{2.30}$$

Here, the quantities with subscript $_{\mathrm{flat}}$ take the values for the flat case, t_0 is the first observation time, and I chose $t_M = 5\,\mathrm{s}$ because the skewness and kurtosis were found to be close to those for the flat interfaces for $t \lessapprox 5\,\mathrm{s}$ [Fig. 2.8(a)]. Similarly, I defined another non-dimensional quantity

$$\beta(v_\infty,\Gamma,t) := \Gamma^{-1/3} t^{2/3} \left(\langle \partial_t h\rangle - v_\infty\right) \tag{2.31}$$

and estimated v_∞ as the minimizer of

$$\int_{t_0}^{t_M} \left(\beta(v_\infty,\Gamma,t) - \beta_{\mathrm{flat}}(v_{\infty_{\mathrm{flat}}},\Gamma_{\mathrm{flat}},t)\right)^2 \mathrm{d}t \tag{2.32}$$

In both cases, the uncertainty was determined from the uncertainty of the parameters for the flat interfaces, and the variation of the estimated value with varying t_M.

outgrowing interfaces approaches to those of χ_2, circular interfaces, whereas the values for the ingrowing interfaces moves in the opposite direction.

The experimental results of the $\langle q(x',t)\rangle$ and the variance $\langle q(x',t)^2\rangle_c$ are shown in Fig. 2.11(a,b). Consistently with the Eden model (Fig. 2.10), the variance $\langle q(x',t)^2\rangle_c$ show departure from the values for the flat interfaces. The values move toward that for the circular interfaces $\langle\chi_2^2\rangle$ in the cases of the outgrowing interfaces [Fig. 2.11(b)], while they showed a deviation to the opposite direction in the ingrowing cases [Fig. 2.11(a)]. On the other hand, the values of the mean $\langle q(x',t)\rangle$ has large finite-time effects. By plotting the difference from the asymptotic values $\langle\chi_1\rangle$ and $\langle\chi_2\rangle$ for the flat and circular interfaces, respectively, the difference from the asymptotic value decreases as $t^{-1/3}$ as observed in the previous experiments [36] [Fig. 2.13(a,b; upper plots inset)].

The exponent $-1/3$ for the finite-time difference in the mean rescaled height $\langle q(x',t)\rangle$ indicates that the term contributing this effect is $\mathcal{O}(1)$ in terms of $h(x,t)$. Also, the uncertainty of the initial position of the interfaces $h(x,0)$ leads to $\mathcal{O}(1)$ effect on $h(x,t)$. In order to avoid the effects of those terms, we defined a quantity using the derivative $\partial_t h(x,t)$

$$\langle p(x',t)\rangle := \left\langle \frac{3t^{2/3}}{\Gamma^{1/3}}\left[\partial_t h(x,t) - v_\infty\right]\right\rangle \tag{2.33}$$

$$\simeq \langle\chi(x',t)\rangle + t\partial_t\langle\chi(x',t)\rangle\,, \tag{2.34}$$

that we call the mean rescaled velocity [10].

The numerical and experimental results for $\langle p(x',t)\rangle$ are plotted in Fig. 2.12(b) and Fig. 2.13(c,d), respectively. For the numerical results [Fig. 2.12(b)], the behavior of the cumulants described above are also observed in $\langle p(x',t)\rangle$; Again the values of the ingrowing and outgrowing interfaces is close to that of the flat interfaces for short time, and then departs at a characteristic time which increases as R_0 increases. For the outgrowing interface, the clear approach to the circular value $\langle\chi_2\rangle$ was observed. For the experimental results, although the relatively large uncertainty of the non-universal parameters makes it challenging to draw a conclusion for the outgrowing interfaces [Fig. 2.13(d)], the behavior of the other quantities including those for the ingrowing interfaces show (at least qualitative) agreement with the result of the Eden model. We conduct more quantitative comparison between the experimental and numerical results in the next section.

2.3.4 Characteristic timescale and scaling functions

In the previous subsections, we observed that the statistical properties of the interfaces growing from ring-shaped initial conditions seemingly depart from those of the flat interface at a timescale which increases as R_0 increases. Then, one natural interest is the characteristic timescale for the departure, and whether one can understand the statistical properties of the interfaces with different R_0 in a unified way. One candidate of the characteristic timescale

[10] We noticed a similar quantity is used in Ref. [17].

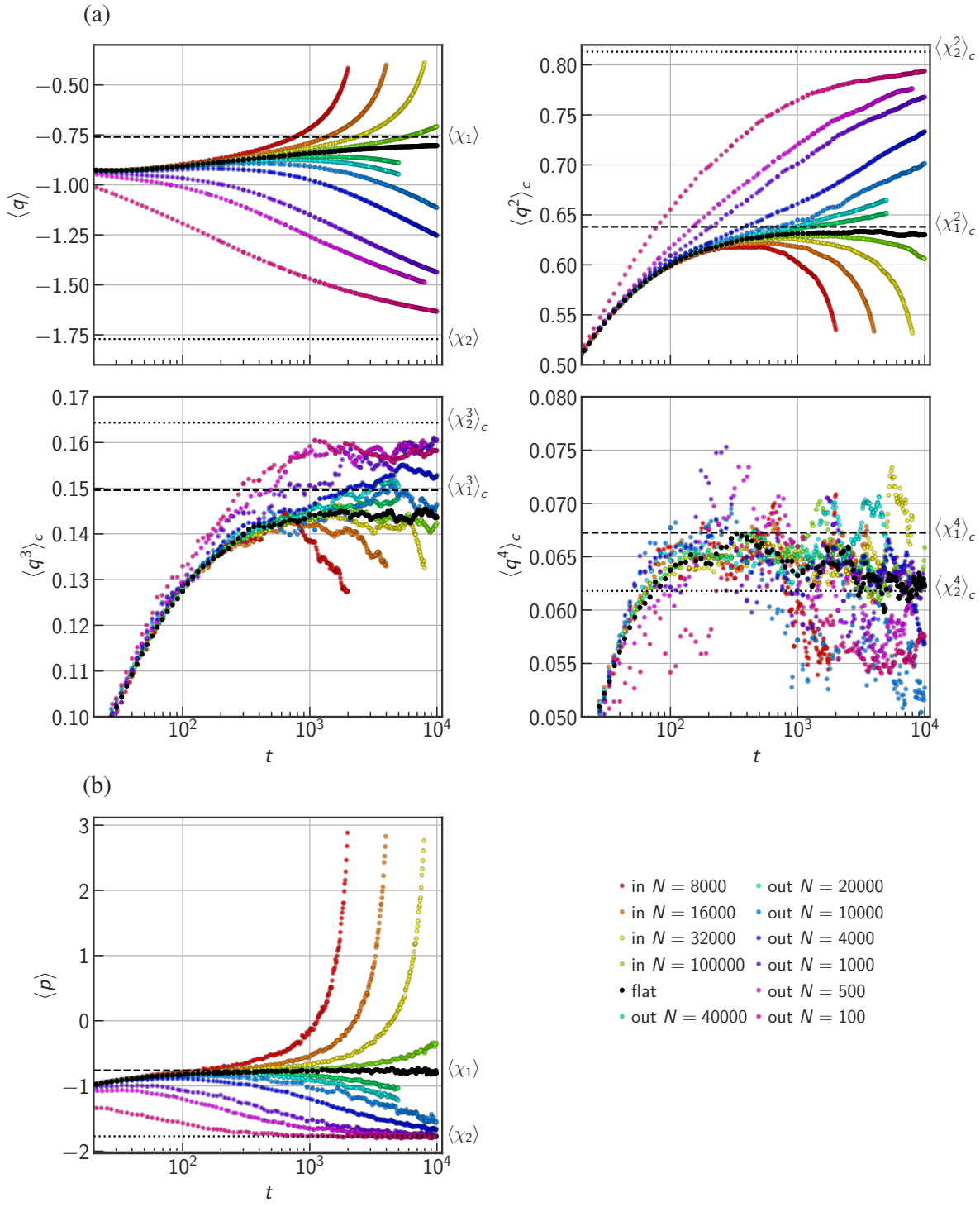

Figure 2.10: (a) The cumulants of the rescaled height $q(x', t)$ and (b) the mean rescaled velocity $p(x', t)$ for the Eden model. The values for χ_1 (flat) and χ_2 (circular) are shown by the dashed and dotted lines, respectively.

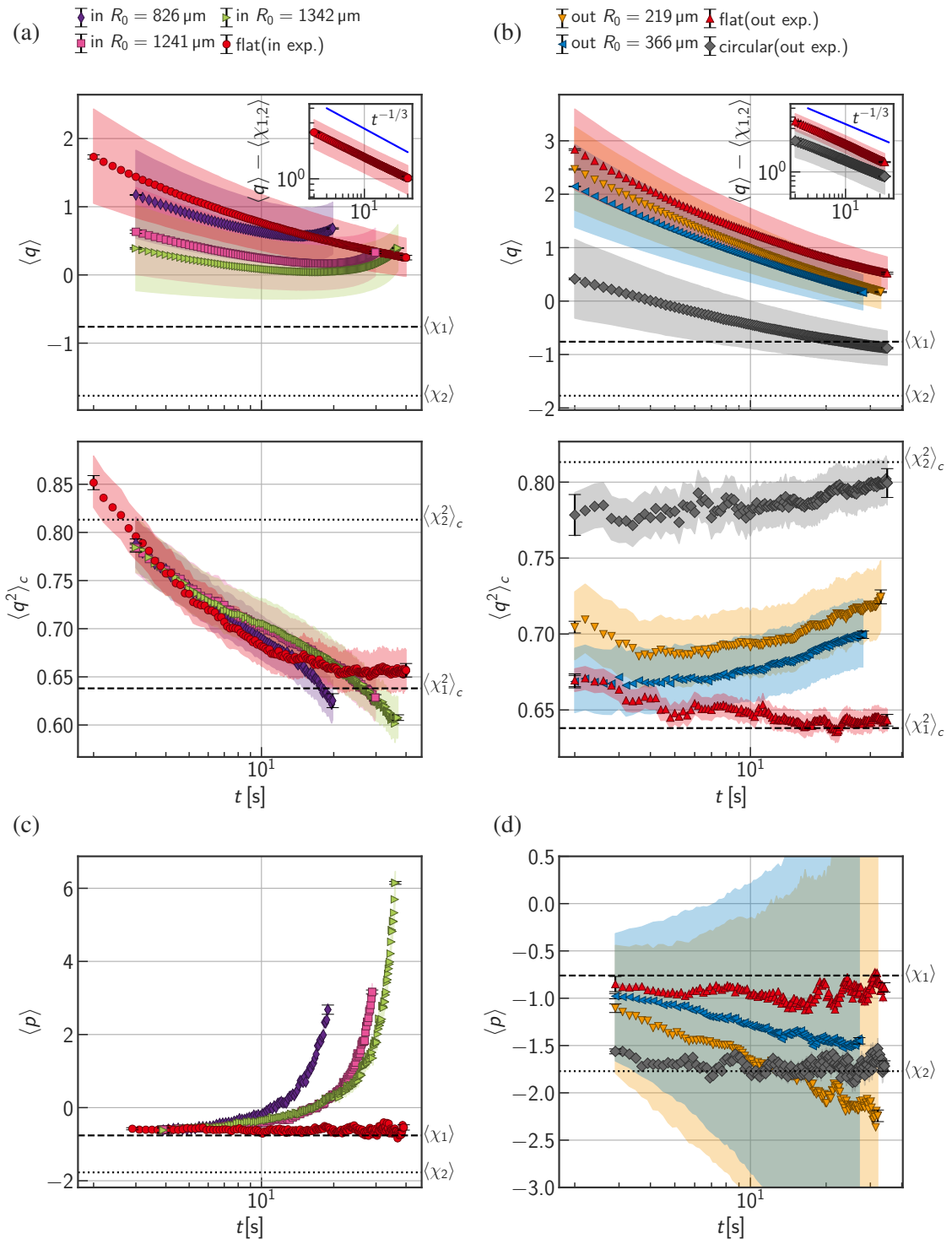

Figure 2.11: (a) The cumulants of the rescaled height $q(x', t)$ and (b) the mean rescaled velocity $p(x', t)$ for the LC experiment. The statistical standard errors are shown by the error bars on the first and the last points. The systematic error due to the uncertainty of the non-universal parameters v_∞ and Γ are indicated by the shaded area with the corresponding color of the markers. The values for χ_1 (flat) and χ_2 (circular) are shown by the dashed and dotted lines, respectively. For the mean $\langle q(x', t) \rangle$, the difference between the values for the flat and circular interfaces and their asymptotic values $\langle \chi_1 \rangle$ (flat) and $\langle \chi_2 \rangle$ (circular) are plotted in the insets with a guide to eye with the slope $-1/3$.

is $t_c := R_0/v_\infty$, which is identical to the collapse time for the ingrowing interfaces. We will demonstrate that rescaling the time by this timescale indeed rescales the statistical properties of the fluctuation with different R_0 onto scaling functions.

In Fig. 2.12 and Fig. 2.13, I plot the numerical and experimental results for the mean, variance, skewness, kurtosis and the mean rescaled velocity $\langle p(x,t)\rangle$ with the rescaled timescale

$$\tau := t/t_0 = v_\infty t/R_0 \,, \tag{2.35}$$

respectively. As for the Eden model (Fig. 2.12), the long-time values of all the quantities plotted collapsed onto scaling functions. Notably, the long-time values of the variance $\langle q(x',t)^2\rangle_c$ (the outgrowing case), the skewness $\mathrm{Sk}[q(x',t)]$, kurtosis $\mathrm{Ku}[q(x',t)]$ and the mean rescaled height $\langle p(x',t)\rangle$ for the LC experiment are rescaled onto the same scaling function as the Eden model within the uncertainty [Fig. 2.13].

For the mean rescaled velocity $\langle p(x',t)\rangle$ for the outgrowing interfaces in the LC experiment, the uncertainty of v_∞ significantly affects the values [Fig. 2.13(b; inset)]. However, by re-estimating the values of v_∞ so that the value of $\langle p(x',t)\rangle$ at the final measured time overlaps on the values of the Eden model, the whole range of the data of $\langle p(x',t)\rangle$ overlapped on the values of the Eden model [Fig. 2.13(b; main plot)], suggesting that $\langle p(x',t)\rangle$ is also rescaled onto the same scaling function as the Eden model. The estimated values of v_∞ here are shown in Table 2.2.

One may notice that the mean rescaled height $\langle q(x',t)\rangle$ and the variance $\langle q(x',t)^2\rangle_c$ for the ingrowing interfaces do not overlap on those for the Eden model. However, we believe this is due to the finite-time effect, since (1) the values even for the flat/circular interfaces are distant from the asymptotic values within our time window, and (2) the curves seemingly approaches to the results of the Eden model with larger R_0, implying they might overlap on the result of the Eden model in the limit of $R_0 \to \infty$.

To summarize the results, let us denote the rescaled height $q(x',t)$ with the initial radius R_0 by $q(x',t;R_0)$. Then, the results imply the existence of the crossover stochastic variable $\chi_c(x',\tau)$ parameterized by τ as $q(x',t;R_0) \simeq \chi_c(x',\tau)$ in the long-time limit. More precisely, with fixed $\tau = v_\infty t/R_0$, we expect

$$\lim_{R_0,t\to\infty} \langle q(x',t;R_0)^n\rangle_c = \langle \chi_c(x',\tau)^n\rangle_c \,, \tag{2.36}$$

where $\chi_c(x',\tau)$ is a stochastic variable parameterized by τ which satisfies

$$\lim_{\tau\to 0} \langle \chi_c(x',\tau)^n\rangle_c = \langle \chi_1^n\rangle_c \,,\ \lim_{\tau\to\infty} \langle \chi_c(x',\tau)^n\rangle_c = \langle \chi_2^n\rangle_c \,. \tag{2.37}$$

2.3.5 Spatial correlation

Figure 2.14 shows the experimental and numerical results of the spatial covariance

$$C_s(\zeta,t) := \mathrm{Cov}[q(x'+\zeta,t), q(x',t)] \,. \tag{2.38}$$

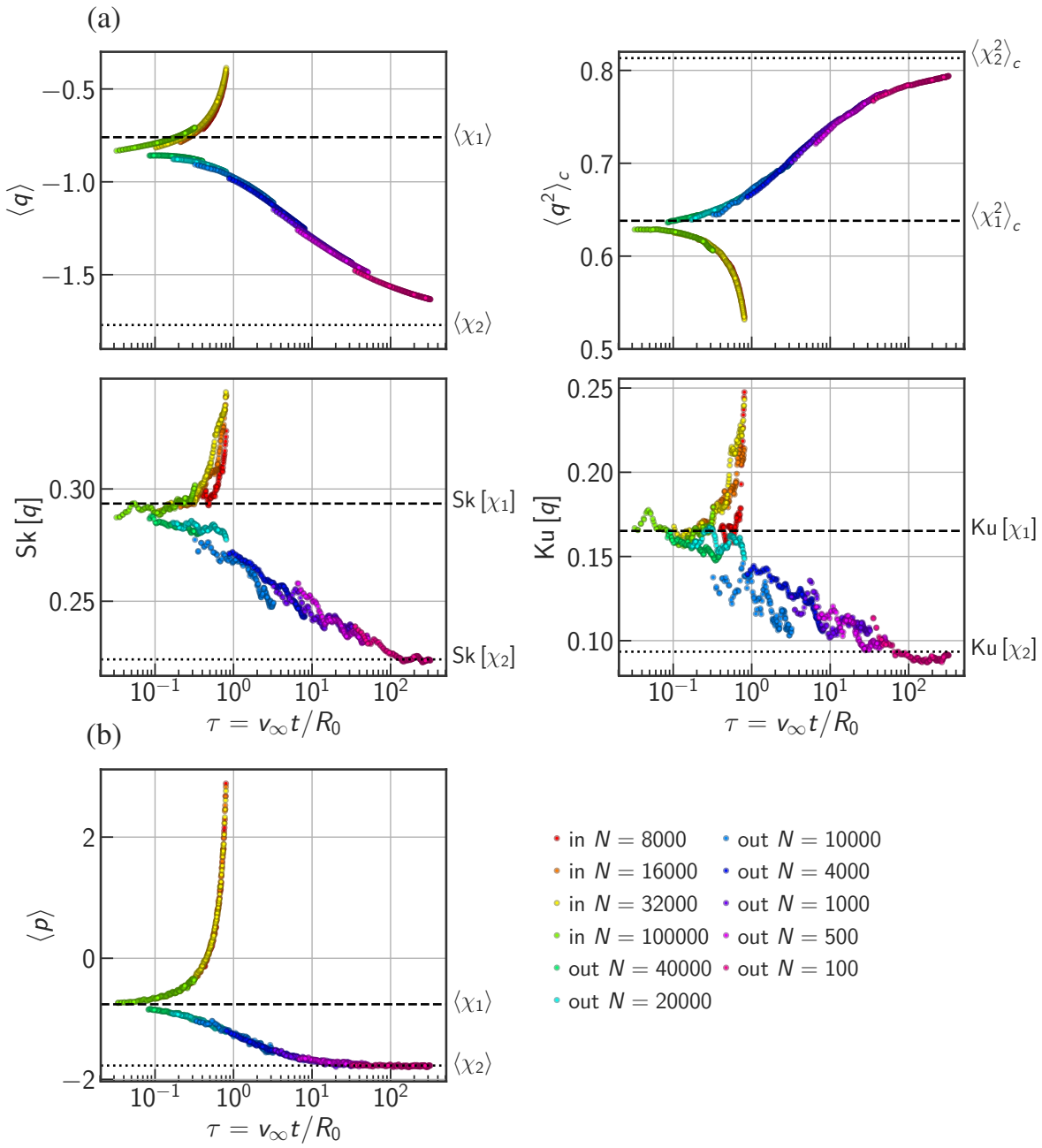

Figure 2.12: (a) The cumulants of the rescaled height $q(x', t)$ and (b) the mean rescaled velocity $\langle p(x', t) \rangle$ for the Eden model, plotted against the rescaled timescale $\tau = v_\infty t / R_0$. For the sake of visualization, only the data with $t \geq 10^3$ are plotted. The values for χ_1 (flat) and χ_2 (circular) are shown by the dashed and dotted lines, respectively.

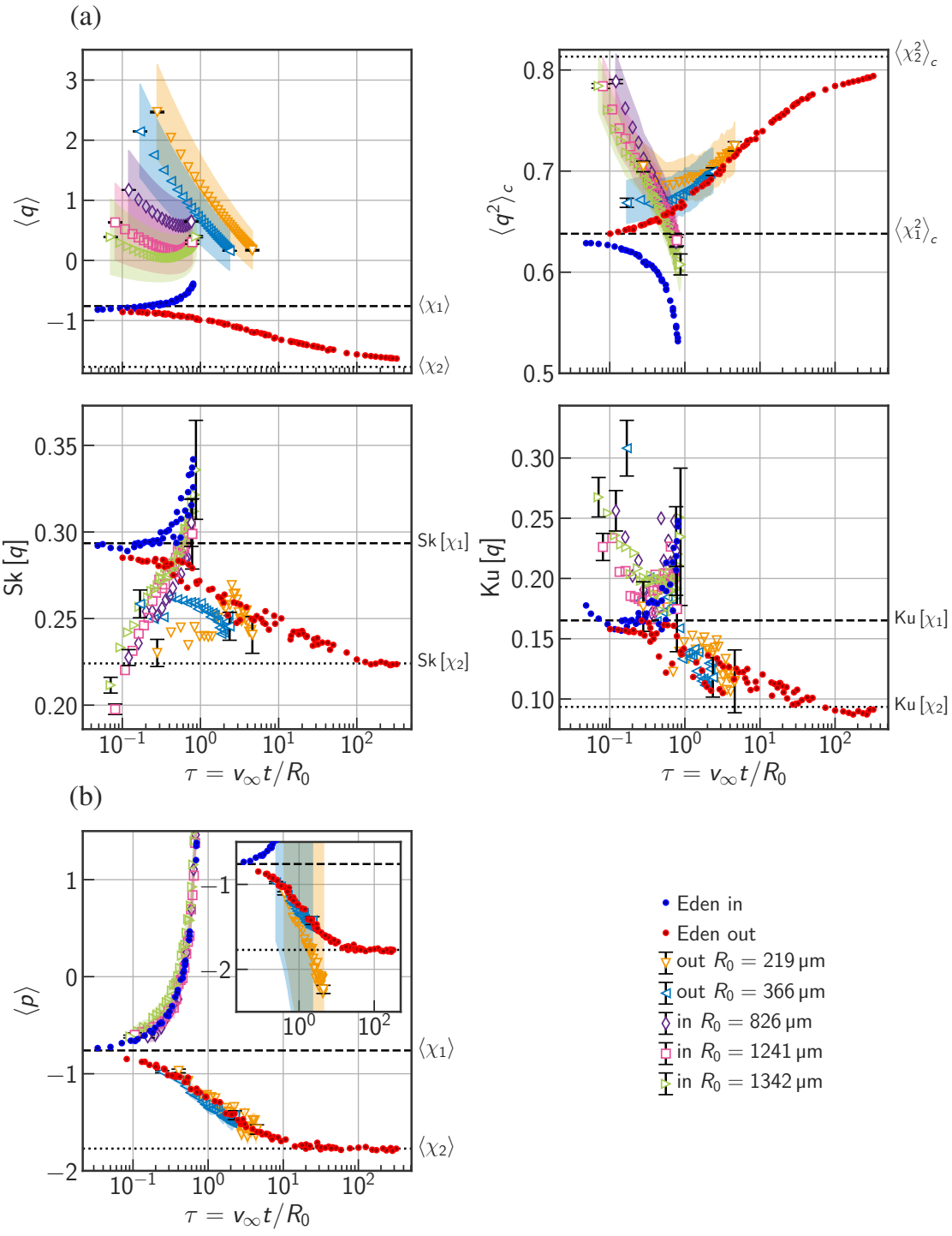

Figure 2.13: (a) The cumulants of the rescaled height $q(x', t)$ and (b) the mean rescaled velocity $\langle p(x', t) \rangle$ for the LC experiment, plotted against the rescaled timescale $\tau = v_\infty t/R_0$. As for the outgrowing interfaces, values rescaled with the same v_∞ as the flat interfaces are shown in the inset, with the uncertainty defined in Sec. 2.3.2. The main plot is with the value of v_∞ estimated by comparing with the result of the Eden model (see the main text). The data for the Eden model (Fig. 2.12) is replotted with the same colors for the sake of comparison. The exact values for χ_1 (flat) and χ_2 (circular) are shown by the dashed and dotted lines, respectively.

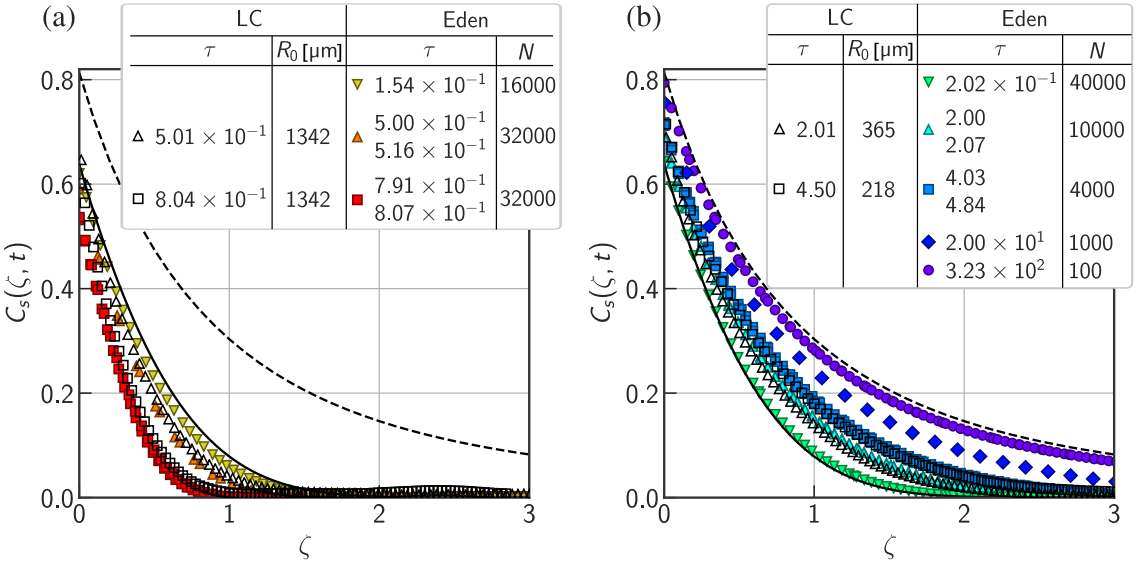

Figure 2.14: Spatial covariance $C_s(\zeta, t)$, plotted against the normalized length ζ, for the ingrowing (a) and outgrowing (b) interfaces. τ and R_0 (or N) or the data points are indicated in the legend. The solid and dashed lines indicate the Airy_1 (flat) and Airy_2 (circular) correlation function, respectively.

One can observe, as τ is varied, that the function moves simultaneously with the values of the cumulants; For the ingrowing interfaces [Fig. 2.14(a)], $C_s(\zeta, t)$ is first close to the Airy_1 covariance, the exact solution for the flat interfaces, and then deviates toward the lower direction as τ becomes larger. For the outgrowing ones [Fig. 2.14(b)], it crossovers between the Airy_1 and Airy_2 covariance, the exact solution for the flat and circular interfaces. The overlap of the experimental and numerical results suggests the universality of the spatial correlation of the crossover fluctuation.

2.4 Theory and generality

Why it was possible to rescale the statistical properties of the fluctuation only by scaling the timescale as $\tau = v_\infty t/R_0$, and are there any theoretical expression for the crossover fluctuation? In this section, we demonstrate that we can answer these questions using a representation of the height distribution of the KPZ interfaces called the variational formula [52, 102].

2.4.1 Variational formula for curved initial conditions

Short summary on variational formula

For the one-point distribution of KPZ interfaces $h(x,t)$ with the initial height $h(x,0) =: h_0(x)$, the *variational formula* conjectured in Ref. [52] reads

$$\frac{h(x,t) - v_\infty t}{(\Gamma t)^{1/3}} \simeq \sup_{Y\in\mathbb{R}} \left[\mathcal{A}_2\left(X - Y\right) - (X-Y)^2 + H_0(Y)\right], \tag{2.39}$$

where

$$X := x/\xi(t) \tag{2.40}$$

$$H_0(Y) := (\Gamma t)^{-1/3} h_0(\xi(t)Y), \tag{2.41}$$

the correlation length $\xi(t)$ defined by Eq. (2.6), and $\mathcal{A}_2(\cdot)$ is a stochastic variable called the Airy_2 process [52, 68, 69]. The formula is conjectural for, e.g., the KPZ equation, but proved to be valid for the TASEP [112, 113].

Roughly speaking, one can derive this formula as follows [112]. With the Hopf-Cole transformation

$$z(x,t) := \exp\left[\frac{\lambda}{2\nu} h(x,t)\right], \tag{1.12}$$

let us consider the stochastic heat equation

$$\partial_t z(x,t) = \nu \partial_x^2 z(x,t) + \frac{\lambda\sqrt{D}}{2\nu} z(x,t)\eta(x,t) \tag{1.13}$$

and denote its solution with the initial condition $z(x,0) := \delta(x)$ by $z_\delta(x,t)$. Considering the linearity of the stochastic heat equation, one can expect that the solution $z(x,t)$ with the initial condition $z(x,0) = z_0(x) = \exp\left[\frac{\lambda}{2\nu} h_0(x)\right]$ is written as

$$z(x,t) = \int_{-\infty}^{\infty} z_\delta(x-y,t) z_0(y) \mathrm{d}y. \tag{2.42}$$

Here, the exact solution for the narrow wedge initial condition (2.14) reads

$$z_\delta(x,t) = \exp\left\{\frac{\lambda}{2\nu}\left[v_\infty t + (\Gamma t)^{1/3} A_t(X) - X^2\right]\right\}, \tag{2.43}$$

where X is that defined in (2.40), $v_\infty = -3^{-1}2^{-7}\nu^{-4}\lambda^3 D^2$, $\Gamma = \frac{\lambda A^2}{2}$, $A = \frac{D}{2\nu}$ and $A_t(\cdot)$ is a stochastic variable called the crossover Airy process [52, 60], which has the conjectural asymptotic limit

$$A_t(X) \to \mathcal{A}_2(X) \ (t \to \infty). \tag{2.44}$$

Substituting Eq. (2.43) into (2.42) and assuming Eq. (2.44) leads to

$$z(x,t) = \int_{-\infty}^{\infty} \exp\left\{\frac{\lambda}{2\nu}\left[v_\infty t + (\Gamma t)^{1/3}\left(\mathcal{A}_2(X-Y) - (X-Y)^2 + H_0(Y)\right)\right]\right\} \mathrm{d}y, \tag{2.45}$$

where $H_0(Y)$ is defined in (2.41). Finally, in order to obtain the fluctuation of $z(x,t)$ in the limit $t \to \infty$, we approximate (2.45) by the saddle point to obtain

$$h(x,t) := \frac{2\nu}{\lambda}\log|z(x,t)| \tag{2.46}$$

$$\simeq v_\infty t + (\Gamma t)^{1/3} \sup_{Y\in\mathbb{R}}\left[\mathcal{A}_2(X-Y) - (X-Y)^2 + H_0(Y)\right] + \mathcal{O}(t^{1/3}), \tag{2.47}$$

which is identical to Eq. (2.39). Here we note that this formula is only valid in the sense of the one-point distribution [112]; To obtain the multi-point correlation, one needs to consider another variational formula including a conjectural two-parameter process called the Airy sheet [112, 114]. In this dissertation, I only focus on the one-point distribution with Eq. (2.39).

Variational formula for curved initial conditions

Now we are ready to compute the variational formula (2.42) in the case of the curved initial conditions. Let us consider an initial condition in a general form

$$h_0(x) = R_0 g\left(\frac{x}{R_0}\right) \tag{2.48}$$

where $g(z)$ is a function which can be Taylor-expanded near the origin as [11]

$$g(z) = \sum_{n=2}^{\infty} \frac{c_n}{n!} z^n. \tag{2.49}$$

For example, one can take $g(z) = \pm\left(\sqrt{1-z^2}-1\right)\mathbb{1}_{|z|<1}$ for the cases with the ring-shaped initial conditions.

[11] Note that the terms with $n = 0, 1$ can be eliminated by translation and rotation.

Substituting (2.48) and (2.49) into (2.41), one obtains

$$H_0(X) = (\Gamma t)^{-1/3} h_0(\xi(t)X) \tag{2.50}$$

$$= \sum_{n=2}^{\infty} \frac{c'_n}{n!} R_0^{1-n} t^{(2n-1)/3} X^n \tag{2.51}$$

$$= \sum_{n=2}^{\infty} \frac{c''_n}{n!} \left(\frac{v_\infty t}{R_0}\right)^{n-1} t^{-(n-2)/3} X^n, \tag{2.52}$$

where $c'_n := 2^n \Gamma^{(2n-1)/3} A^{-n} c_n$ and $c''_n = c'_n / v_\infty^{n-1}$. Let us consider the limit $R_0, t \to \infty$ with fixed $\tau = v_\infty t / R_0$. Then, the terms in (2.52) with $n \geq 3$ vanish as $\sim t^{-(n-2)/3}$. Thus we obtain

$$H_0(X) \simeq \frac{2c_2\Gamma}{A^2 v_\infty} \tau X^2, \tag{2.53}$$

and substituting into (2.39) and setting $x = 0$ yields

$$\frac{h(x,t) - v_\infty t}{(\Gamma t)^{1/3}} \simeq \sup_{Y \in \mathbb{R}} \left[\mathcal{A}_2(Y) - \left(1 - \frac{2c_2\Gamma}{A^2 v_\infty}\tau\right) Y^2 \right], \tag{2.54}$$

where we used the property of the Airy$_2$ process $\mathcal{A}_2(-Y) = \mathcal{A}_2(Y)$, which is intuitively clear from the symmetry of the interface fluctuation with respect to $x \to -x$. In the isotropic cases, by using the relationship (2.25), one can further simplify the formula as

$$\frac{h(x,t) - v_\infty t}{(\Gamma t)^{1/3}} \simeq \sup_{Y \in \mathbb{R}} \left[\mathcal{A}_2(Y) - (1 - c_2\tau) Y^2 \right]. \tag{2.55}$$

Finally, let us consider the cases with the ring-shaped initial conditions $g(z) = \sigma\left(\sqrt{1-z^2} - 1\right) \mathbb{1}_{|z|<1}$, where $\sigma = -1$ for the ingrowing interfaces and $+1$ for the outgrowing interfaces. Since $\sqrt{1-z^2} = 1 - \frac{1}{2}z^2 + \mathcal{O}(z^4)$, one finds

$$\frac{h(x,t) - v_\infty t}{(\Gamma t)^{1/3}} \simeq \chi_{\mathrm{parbl}}^{(\hat{\tau})} := \sup_{Y \in \mathbb{R}} \left[\mathcal{A}_2(Y) - (1 + \hat{\tau}) Y^2 \right], \tag{2.56}$$

where $\hat{\tau} := \sigma\tau$. The formula (2.56) explains the observation in Sec. 2.3.4, with suggesting that the one-point distribution of $\chi_c(x', \tau)$ [Eq. (2.37)] is indeed given by $\chi_{\mathrm{parbl}}^{(\hat{\tau})}$. Also, the discussion in this section suggests that the fluctuation described by Eq. (2.53) generally appears for the initial conditions described by (2.48) and (2.49), such as ellipses.

2.4.2 Numerical evaluation of variational formula

In order to compare the formula with the experimental and numerical results, one needs to evaluate the formula (2.56) [or more generally, (2.39)] numerically. Here I consider three

candidates of the methods to evaluate (2.56):

1. Using the explicit Fredholm-determinant formula presented in Eq. (1.49) in Ref. [102] for the variational problem Eq. (2.55) (in a different context):

$$\mathrm{Prob}\left[\sup_Y \left[\mathcal{A}_2(Y) - (1+\tau)Y^2\right] < r\right] = \det\left[\mathbb{I} - K_{\mathrm{Ai}} + A\bar{P}_0 \mathcal{S}^{\tau,\tau}_{\mathrm{parbl}} \bar{P}_0 A^*\right] \ (\tau > 0), \tag{2.57}$$

   where A, $\bar{P}_0$ and $\mathcal{S}^{\beta_1,\beta_2}_{\mathrm{parbl}}$ are integral operators defined in Ref. [102].

2. Using the Fredholm-determinant formula for the general initial condition presented in Thm. 8 in Ref. [52]:

$$\mathrm{Prob}\left[\mathcal{A}_2(Y) \le g(Y) \text{ for } t \in [-L.L]\right] = \det\left[\mathbb{I} - K_{\mathrm{Ai}} \Theta^g_H e^{2LH} K_{\mathrm{Ai}}\right], \tag{2.58}$$

   where $H := -\triangle + x$ and Θ^g_H is an operator that maps a function $f(\cdot)$ to a function $u(L,\cdot)$ where $u(t,x)$ satisfies the partial differential equation (PDE) $\partial_t u + Hu = 0$ with an appropriate boundary condition involving f (see Ref. [52] for details).

3. Directly evaluating the variational formula (2.56) through a Monte-Carlo (MC) simulation of the Airy_2 process.

Though the methods 1 and 2 are attractive in a sense that they directly provide the cumulative distribution function $\mathrm{Prob}\left[\chi^{(\tau)}_{\mathrm{parbl}} < r\right]$, we think the numerical evaluation of those representations are still challenging practically. For the method 1, this is because $\mathcal{S}^{\tau,\tau}_{\mathrm{parbl}}$ includes an infinite sum and nested integrals in its representation. For the method 2, the difficulty is due to, for example, the lack of knowledge on the accuracy of the numerical evaluation of the PDE, and the computational cost to evaluate $e^{2LH}K_{\mathrm{Ai}}$ for the boundary condition for the PDE. With these reasons, here I evaluated Eq. (2.56) by the method 3 in this study as follows.

I approximated the Airy process $\mathcal{A}_2(Y)$ by the largest eigenvalue $\lambda^N(u)$ in the Dyson's Brownian motion of $N \times N$ GUE random matrices [51], the time-evolving Hermite random matrices $\mathbf{H}(u) = \{H_{jk}(u)\}_{j,k=1,\ldots,N}$, whose elements follow the Ornstein-Uhlenbeck processes as

$$\frac{\mathrm{d}H_{jk}(u)}{\mathrm{d}u} = \begin{cases} -H_{jk}(u) + \eta^{(1)}_{jk}(u) & (j=k) \\ -H_{jk}(u) + \sqrt{\frac{1}{2}}\left[\eta^{(1)}_{jk}(u) + \mathrm{i}\eta^{(2)}_{jk}(u)\right] & (j>k) \end{cases} \tag{2.59}$$

where $\eta^{(m)}_{jk}(u)$ is the Gaussian noise satisfying

$$\left\langle \eta^{(m)}_{jk}(u) \right\rangle = 0, \ \left\langle \eta^{(m')}_{j'k'}(u')\eta^{(m)}_{jk}(u) \right\rangle = \delta_{j'j}\delta_{k'k}\delta_{m'm}\delta(u'-u), \tag{2.60}$$

since it is known that $\lambda^N(u)$ converges to the Airy_2 process with $N \to \infty$ with so-called the

edge scaling

$$\tilde{\lambda}^N(\tilde{u}) := \sqrt{2}N^{1/6}\left(\lambda^N(N^{-1/3}\tilde{u}) - \sqrt{2N}\right) \tag{2.61}$$

as

$$\lim_{N\to\infty} \tilde{\lambda}^N(\tilde{u}) = \mathcal{A}_2\left(\tilde{u}\right), \tag{2.62}$$

in the sense of the convergence of finite-dimensional distributions [52, 69, 115].

The detailed steps for the MC evaluation are as follows:

1. We first prepared the initial Hermite random matrix drawn from the stationary distribution of Eq. (2.59),

$$H_{jk}(0) = \begin{cases} \sqrt{\frac{1}{2}}\mathcal{N}_{jk}^{(1)} & (j=k) \\ \frac{1}{2}\left[\mathcal{N}_{jk}^{(1)} + \mathrm{i}\mathcal{N}_{jk}^{(2)}\right] & (j>k) \end{cases}, \tag{2.63}$$

   where $\mathcal{N}_{jk}^{(m)}$ are mutually independent random variable following the normal distribution with the mean 0 and the variance 1.

2. We then simulated the Ornstein-Uhlenbeck process (2.59) for each element, using the exact formula presented in Ref. [116] with the timestep Δu. We compute the largest eigenvalues $\lambda_j^N := \lambda^N(j\Delta u)(j = 0, \ldots, j_{\max})$ for each timestep $j\Delta u$. Following Eq. (2.61), the values were rescaled as

$$\tilde{\lambda}_j^N := \sqrt{2}N^{1/6}\left(\lambda_j^N - \sqrt{2N}\right) \tag{2.64}$$

$$\Delta\tilde{u} := N^{1/3}\Delta u. \tag{2.65}$$

3. We approximated the variational formula by

$$\chi_{\mathrm{parbl}}^{(\hat{\tau})} = \sup_Y \left[\mathcal{A}_2\left(Y\right) - (1+\hat{\tau})Y^2\right] \approx \max_k \left[\tilde{\lambda}_{j+k}^N - (1+\hat{\tau})\left((j+k)\Delta\tilde{u}\right)^2\right], \tag{2.66}$$

   where $j = L, \ldots, j_{\max} - L$ and L is taken sufficiently large to avoid the effect of the boundaries. The cumulants $\left\langle (\chi_{\mathrm{parbl}}^{(\hat{\tau})})^k \right\rangle_c$ were evaluated by taking the average of the right-hand side with respect to j and independent realizations of the random matrices.

We used the matrix size of $N = 256$, which has been shown to be sufficiently large to reproduce, e.g., the covariance of the Airy_2 process $\mathrm{Cov}[\mathcal{A}_2\left(X\right), \mathcal{A}_2\left(0\right)]$ [117]. The other parameters are set to be $\Delta u = 10^{-3}N^{-1/3}$ and $j_{\max} = 10^6$. We simulated 320 independent series of random matrices. In the following section, we present the result of the MC evaluation of (2.55), and compare it with the fluctuation of the interfaces with the ring-shaped initial conditions.

2.4.3 Comparison with interfaces with ring-shaped initial conditions

In Fig. 2.15(a), we plot the mean, variance, skewness and kurtosis of $\chi_{\rm parbl}^{(\hat{\tau})}$ evaluated by the variational formula for several points (indicated by the triangular markers) together with the result of the Eden model replotted from Fig. 2.12 (circular markers, in the same way as 2.13). The uncertainty of each cumulant (the shaded area) for the MC result of the variational formula was estimated by calculating the standard error (standard deviation of the results each of which was estimated using single sequence of the random matrices, divided by the square root of the number of the sequence of the random matrices). Note that the statistical error can be correlated for different points because we used the same random matrices to evaluate the values for different τ. Also, the rescaled mean

$$\left\langle \phi_{\rm parbl}^{(\hat{\tau})} \right\rangle := \left\langle \chi_{\rm parbl}^{(\hat{\tau})} \right\rangle + 3\partial_\tau \left\langle \chi_{\rm parbl}^{(\hat{\tau})} \right\rangle \tag{2.67}$$

corresponding to the mean rescaled velocity $\langle p(x',t)\rangle$ (Eq. (2.33)) was evaluated by interpolating $\left\langle \chi_{\rm parbl}^{(\hat{\tau})} \right\rangle$ by Lagrange polynomials at 10 Chebyshev points for each of the $\tau > 0$ and $\tau < 0$ branches, and analytically calculating the derivative of the interpolating polynomials [Fig. 2.15(b)].

The values of the cumulants calculated by the variational formula is consistent with those of the rescaled height $\left\langle q(x',t)^k \right\rangle_c$ and the mean rescaled velocity $\langle p(x',t)\rangle$ of the Eden model (and also those of the LC experiments as we saw in Fig. 2.13) with the ring-shaped initial conditions, respectively. These results corroborate the idea that the one-point distribution of $\chi_c(x',\tau)$ [Eq. (2.37)] is identical to $\chi_{\rm parbl}^{(\hat{\tau})}$. The small but systematic deviation between the values for the variational formula and that for the Eden model was, however, observed. This deviation may be attributed to the estimation error of the non-universal parameters, or the "finite R_0 effect", since the formula (2.56) was derived in the limit of $R_0 \to \infty$ with fixed τ. Considering the next order term in the expansion (2.52) might help us understand the corrections due to finite R_0.

2.5 Summary and discussions

To summarize, we constructed an experimental setup which enables us to investigate the growth of DSM2 cluster with arbitrary designed initial conditions. Experimentally using this setup as well as numerically, we investigated interfaces growing inward or outward from the ring-shaped initial conditions. We found that the cumulants of the rescaled height $\left\langle q(x',t)^k \right\rangle_c$ and the spatial covariance $C_s(\zeta,t)$ seem to be parametrized only by the rescaled timescale $\tau = v_\infty t/R_0$ for large t suggesting the existence of the universal fluctuation $\chi_c(x',\tau)$ satisfying $q(x',t;R_0) \simeq \chi_c(x',\tau)$. For both of the ingrowing and outgrowing cases, the statistical properties of the flat subclass were observed with small values of τ, whereas the behavior for large τ was distinct between the ingrowing and outgrowing cases. The outgrowing interfaces

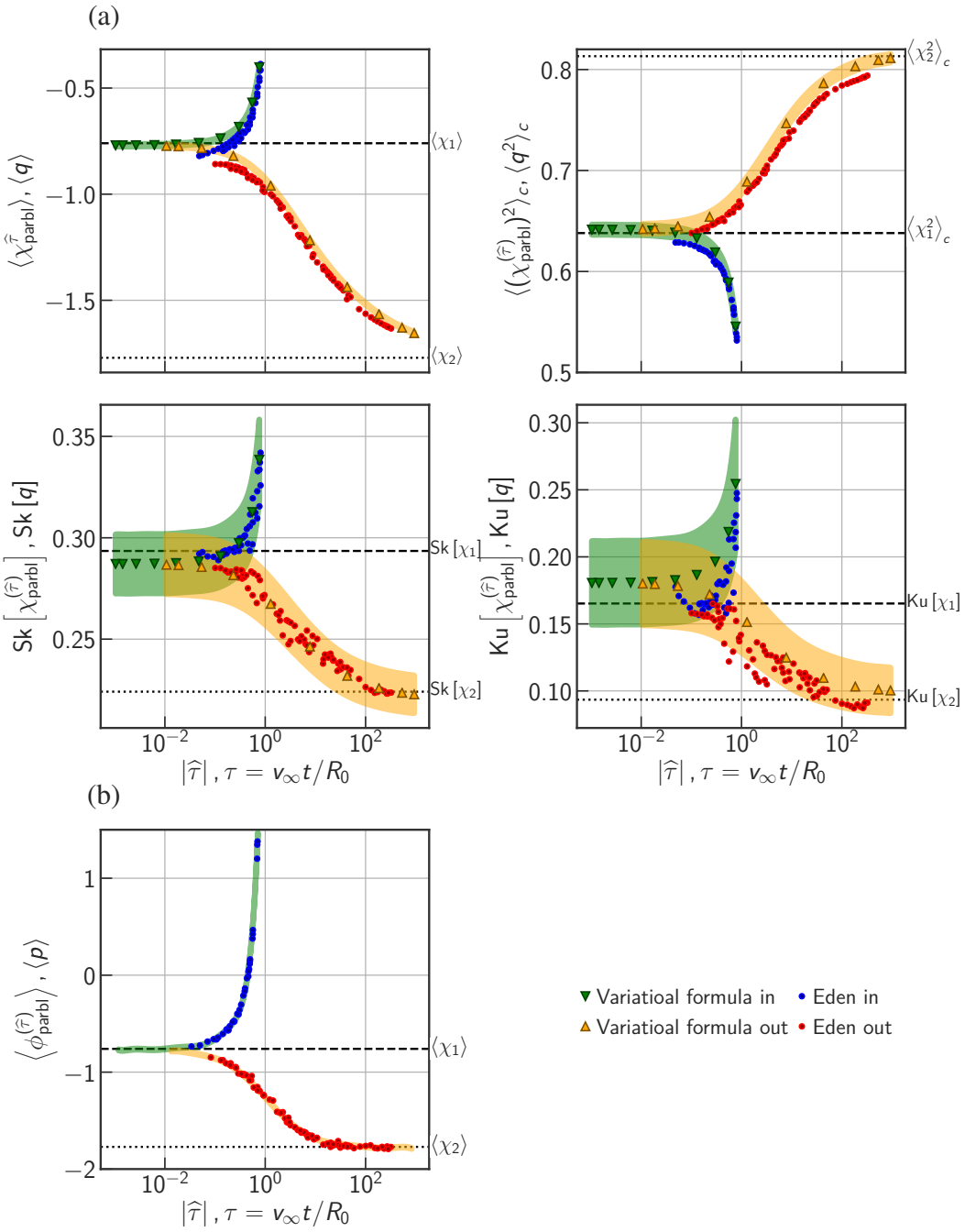

Figure 2.15: (a) The mean, variance, skewness and kurtosis of $\chi^{(\hat{\tau})}_{\mathrm{parbl}}$ and (b) the rescaled mean $\left\langle \phi^{(\hat{\tau})}_{\mathrm{parbl}} \right\rangle$ evaluated by the MC simulation for the variational formula (2.55). The triangular markers indicate the values of the formula evaluated at the Chebyshev points, and the shaded areas indicate the statistical uncertainty estimated by the doubled standard error. (Note that the error is not necessarily independent for the different points.) The cumulants of the rescaled height $\left\langle q(x',t)^k \right\rangle_c$ and the mean rescaled velocity $\langle p(x',t)\rangle$ for the Eden model (Fig. 2.12) is replotted as in Fig. 2.13. The values for χ_1 (flat) and χ_2 (circular) are shown by the dashed and dotted lines, respectively.

show the crossover to the circular subclass as $\tau \to \infty$, while statistical properties of the ingrowing interfaces deviate from those of the flat subclass with no sign of the circular subclass. This result demonstrates that the sign of the curvature is relevant to determine the subclasses.

In order to understand the observed behaviors, we constructed a formula for the one-point distribution of the rescale height, on the basis of the variational formula for general initial conditions (2.39). Our formula naturally explains why the asymptotic fluctuation seems to be parametrized by τ, and suggests that the same behavior can be found in the limit we considered for *any* interfaces with locally-parabola initial conditions. The values of the cumulants numerically evaluated by our variational formula were consistent with those for the interfaces with the ring-shaped initial conditions, suggesting that our experiment is in the regime explained by the formula we derived.

We anticipate that the method we employed provides us an intuitive perspective to understand interface fluctuations with more general initial conditions. For example, from the formula (2.55), the formula suggests that for interfaces with locally-flat initial conditions such as polygons, one needs to consider a different time rescaling to observe a nontrivial behavior such as the crossover to the circular subclass.

We note that the spatial covariance $C_s(\zeta, t)$ for the curved interfaces is still not numerically evaluated from the variational formula. We find it interesting to consider whether one can numerically evaluate (or approximate) the Airy sheet and compare the result of the spatial covariance of the variational formula to the experimental results. We also note that our evaluation of the variational formula (2.55) is by the rather naïve Monte-Carlo method in this dissertation. Numerically tractable explicit formula (e.g. Fredholm determinant formula) for Eq. (2.55) may help further studies.

Finally, we briefly remark several potentially related studies.

- The spatial crossover of the fluctuation between the flat and circular subclasses, the crossover of $\chi(x', t)$ depending on the position x' in the limit of $t \to \infty$, has been found in e.g., the half-flat initial condition [33, 118, 119]. It might be interesting to investigate if there are similarities between those cases and the temporal crossover appeared in this study.

- Numerically, interfaces on a substrate enlarging or shrinking with time have been investigated [99, 100], for which the statistical properties of the fluctuations are similar to those with the curved initial conditions. Our results suggest that the variational formula may also describe fluctuations found in this system. It may be interesting to study how the variational formula can be extended for those cases.

- The geometry-dependent fluctuations are found not only for the $(1 + 1)$-dimensional interfaces, but also for the $(2 + 1)$-dimensional KPZ interfaces [20]. Considering that the variational formula relies on the linearity of the stochastic heat equation (1.13), it is natural to expect that a similar variational formula describes the interface fluctuation with general initial conditions also in the case of $(2 + 1)$-D, where the Airy_2 process is

replaced by the solution of the $(2+1)$-D KPZ equation with the "sharp needle" initial condition

$$h(x,0) = \begin{cases} 0 & (x = (0,0)) \\ -\infty & (\text{otherwise}) \end{cases}, \tag{2.68}$$

which corresponds to the delta-function initial condition in terms of the stochastic heat equation.

Chapter 3

Relationship between directed percolation and Kardar-Parisi-Zhang universality classes

Related publications by author:

- *in preparation.* (in collaboration with K. Tamai, H. Yamaguchi and T. Hiraiwa)

Contribution:

The author (Y. T. Fukai) conducted the numerical simulations and analyzed the results under discussion with the collaborators (K. Tamai, H. Yamaguchi and T. Hiraiwa).

3.1 Topical introduction

In this section, first I introduce the directed percolation (DP) universality class, which is one of the fundamental classes for an absorbing state phase transition: a phase transition into a state from which the escape is not possible. Then I remark the relationship between the DP class and the partial differential equation known as the Fisher–Kolmogorov–Petrovsky–Piscounov (FKPP) equation which describes the front propagation. Finally, I briefly review the studies on the relationship between the stochastic version of the FKPP equation and the interface fluctuation and state our motivation.

3.1.1 Brief overview on directed percolation universality class

In order to review the idea of the absorbing state phase transition and the DP universality class, let us begin with a simple model called the contact process on an infinitely large d-dimensional lattice [120–123] as an example. In the model, each lattice site takes either of the two states called the "active" or "inactive" state which obeys the following two processes [Fig. 3.1(a)]:

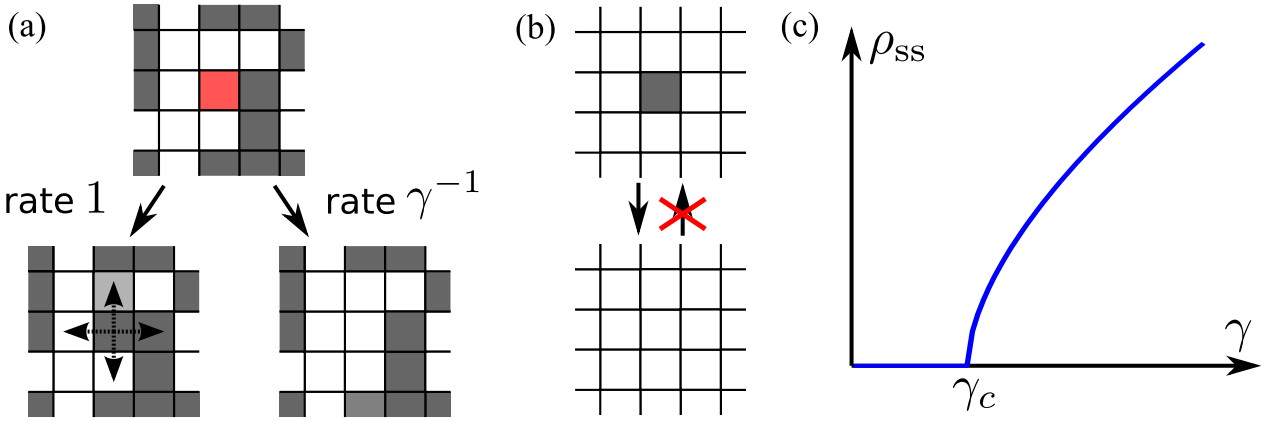

Figure 3.1: Schematic illustration of the contact process. (a) The evolution rule. The gray and white squares denotes the active sites and the inactive sites, respectively. One of the active sites is marked by red in the top figure in order to illustrate the dynamics it can follow. The site can either divide to the nearest neighbor site or deactivate with the rate 1 and γ^{-1}, respectively. (b) Illustration of the absorbing state. If all of the sites become inactive, the state of the system does not change furthermore. (c) Qualitative behavior of the steady-state density of the active sites $\rho_{\rm ss}$ with respective to the inactivation timescale γ for a sufficiently large system.

- Active sites turn one of its adjacent site active at a constant rate of 1.
- Active sites inactivate at a constant rate of γ^{-1}.

One can regard this model as, for example, a simple model for epidemics where the active sites correspond to an infected individual [122], or a population dynamics model of two spices including mutations [97]. As one can imagine, small inactivation timescale γ leads to the state in which all the sites are in the inactive state [Fig. 3.1(b)]. This state is the one example of the *absorbing state* from which the system cannot escape to other states, since there are no spontaneous nucleations of an active site in the model.

Let us consider the stationary density of the active sites $\rho_{\rm ss}(\gamma)$ realized with the initial condition such that, for example, all of the sites are active. It is known that there is a critical value γ_c above which $\rho_{\rm ss}(\gamma)$ takes a non-zero value as illustrated in Fig. 3.1(c) [120, 121, 123]. Regarding $\rho_{\rm ss}(\gamma)$ as the order parameter, transition from the active state $\rho_{\rm ss}(\gamma) > 0$ to the absorbing state $\rho_{\rm ss}(\gamma) = 0$ at $\gamma = \gamma_c$ exemplify the absorbing phase transition, which is a nonequilibrium phase transition by its nature since the detailed balance of the dynamics is broken due to the existence of the absorbing state [Fig. 3.1(b)].

The continuous singularity at the transition point [Fig. 3.1(c)] reminds us of the second-order phase transition and critical phenomena in equilibrium systems. Indeed, the correlation time and correlation length diverge at the critical point, leading to the universal phenomena. More specifically, defining the distance from the transition point ϵ by $\epsilon := (\gamma - \gamma_c)/\gamma_c$, theoretical and numerical observations are consistent with the following *scaling ansatz*: The

Table 3.1: The critical exponents for the DP class.

	$d = 1$ [124]	$d = 2$ [125]	$d = 3$ [125]
$\beta_{\rm DP}$	0.276486(8)	0.580(4)	0.818(4)
$\nu_\parallel$	1.733847(6)	1.287(2)	1.106(3)
$\nu_\perp$	1.096854(4)	0.729(1)	0.582(2)
$z_{\rm DP} := \nu_\parallel/\nu_\perp$	1.580745(10)	1.7665(2)	1.8990(4)
$\alpha_{\rm DP} := \beta_{\rm DP}/\nu_\parallel$	0.159464(6)	0.4510(4)	0.7398(10)

large-scale configuration of the active sites are invariant under the following multiplicative variable scaling

$$\epsilon \to b\epsilon, \quad \rho \to b^{\beta_{\rm DP}}\rho, \quad t \to b^{-\nu_\parallel}t, \quad x \to b^{-\nu_\perp}x, \tag{3.1}$$

where $b > 0$, ρ, t and x are characteristic scales of the density, time and length. The values of the exponents β, $\nu_\parallel$, $\nu_\perp$ (summarized in Table 3.1 [1]), which take nontrivial values different from the mean-field theory with the dimension less than $d_c = 4$, are found to be universal in various systems [120, 121], suggesting that the concept of the universality classes can also be applied to the absorbing state transitions. The transitions characterized by the same exponents as the contact process on a d-dimensional lattice are called to belongs to the (d+1)-D *directed percolation* (DP) universality class.

The DP class is known to be quite robust in theoretical contexts, leading to the *DP conjecture* [120, 121], which is attributed to the works by H. K. Janssen and P. Grassberger [126, 127], stating that a model generally falls into the DP class if:

1. The model displays a continuous phase transition from a fluctuating active phase into a unique absorbing state.

2. The transition is characterized by a positive one-component order parameter.

3. The dynamic rules involve only short-range processes.

4. The system has no unconventional attributes such as additional symmetries or quenched randomness.

According to Ref. [120, 121], no counterexamples for the conjecture have been found, while even a model which does not fulfill the above conditions can fall into the DP class.

In contrast to the theoretical situation, it had not been fully confirmed whether the DP class behavior is experimentally observed, until the (2+1)-D critical behavior of the DP class was found in the LC electroconvection (Sec. 2.1.2) in 2007 by K. A. Takeuchi and the collaborators [37, 38]. In the experiment, they investigated the dynamics of the DSM2 patches, which coexist with the DSM1 [Fig. 3.2(a,b)] at a voltage lower than the

[1] We use $\alpha_{\rm DP}$, $\beta_{\rm DP}$, and $z_{\rm DP}$ instead of the standard notations α, β and z in order to avoid possible confusions with the KPZ exponents.

interface-growth experiment (Sec. 2.1.2). Since the DSM2 is barely created from the DSM1 spontaneously, they regarded the DSM2 as the active sites. They identified 12 exponents, 5 scaling functions and 8 scaling relations confirming that the DSM1-DSM2 transition indeed belongs to the (2+1)-D DP universality class [Fig. 3.2(c,d)]. Recently, the DP-class behaviors are identified in the shear-induced laminar-turbulent transition of a Newtonian fluid [128, 129]. This finding supported the Y. Pomeau's conjecture that laminar-turbulent transition through the spatiotemporal intermittency belongs to the DP universality class [130], and provided us a clear characterization of the transition which has been a long-standing problem from the experiment by Reynolds [131].

Before proceeding, let us present the consequence of the scale invariance (3.1) in a convenient manner. As an example, let us consider a quantity $f(\rho, t, x; \epsilon)$ which depends on the normalized control parameter $\epsilon = (\gamma - \gamma_c)/\gamma_c$ and the parameters ρ, t and x which scale in the same way as the steady-state density, the correlation time and the correlation length. Assuming (3.1), one can see that $f(\rho, t, x; \epsilon)$ is a generalized homogeneous function [132] satisfying

$$f(\rho, t, x; \epsilon) = b^{-l} f(b^{\beta_{\rm DP}}\rho, b^{-\nu_\parallel}t, b^{-\nu_\perp}x; b\epsilon) \tag{3.2}$$

for any $b > 0$, where the exponent l can be inferred either from the physical dimension of f or consistency with other scaling laws.

As an illustration, let us consider the mean density of the active particles $\bar{\rho}(t)$ in a system evolving from the initial condition such that all the sites are active. Then, the scaling form

$$\bar{\rho}(t) = b^{-\beta_{\rm DP}} g(b^{-\nu_\parallel}t, b\epsilon) \tag{3.3}$$

can be inferred from the scale invariance (3.1). By setting $b = t^{1/\nu_\parallel}$, one finds

$$\bar{\rho}(t) = t^{-\alpha_{\rm DP}} g(1, t^{1/\nu_\parallel}\epsilon) \tag{3.4}$$

where $\alpha_{\rm DP} := \beta_{\rm DP}/\nu_\parallel$. In particular, at the critical point $\epsilon = 0$, one obtains the power law

$$\bar{\rho}(t) = t^{-\alpha_{\rm DP}} g(1, 0) \sim t^{-\alpha_{\rm DP}}. \tag{3.5}$$

In order to compare results for different systems, it is convenient to further define characteristic scales of the density ρ_0, the time t_0 and the length x_0 (called the *metric factors*) and write (3.2) in the nondimensional form

$$\tilde{f}(\rho/\rho_0, t/t_0, x/x_0; \epsilon) = b^{-l} \tilde{f}(b^{\beta_{\rm DP}}\rho/\rho_0, b^{-\nu_\parallel}t/t_0, b^{-\nu_\perp}x/x_0; b\epsilon). \tag{3.6}$$

With this form, one can expect that the function $\tilde{f}(\tilde{\rho}, \tilde{t}, \tilde{x}; \epsilon)$ itself is universal for systems in the DP class, if one uses the same definition for ρ_0, t_0 and x_0 [120, 121].

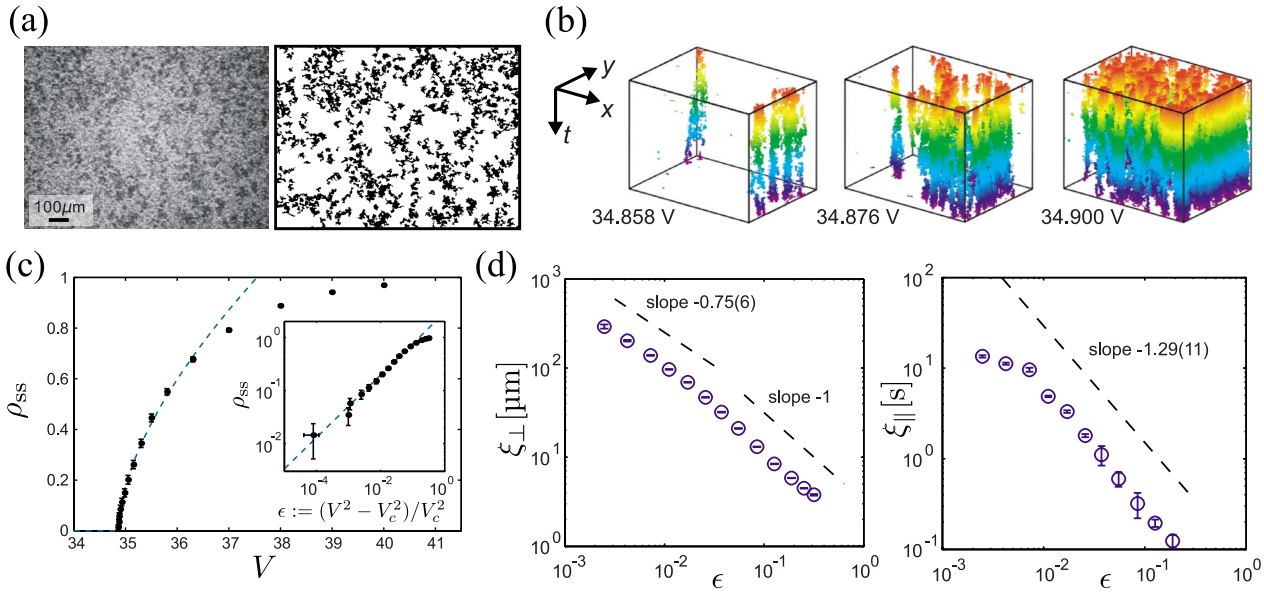

Figure 3.2: Observation of DP critical behavior in the DSM1-DSM2 transition in LC electroconvection [37, 38]. (a) (left) An image taken at 35.153 V. DSM2 patches appears darker in the relatively brighter DSM1. (right) A binarized image. Black patches correspond to the DSM2. (b) Temporal dynamics of the DSM2 patches near the critical voltage $V_c = 34.856(4)$ V. Branching and disappearance of DSM2 patches are observed. The size of the box is 1206 μm × 899 μm in the x and y directions and 6 s in time. (c,d) A part of the results confirming the scaling exponents for the DP class. (c) The steady-state density of the DSM2 ρ_{ss} plotted against the voltage. The blue broken line is the fitting curve by the function $\rho_{ss} = \epsilon^{\beta_{DP}}$ with $\epsilon := (V^2 - V_c^2)/V_c^2$ where V is the applied voltage and V_c is the critical voltage (fitting parameter), which yielded $\beta_{DP} = 0.59(4)$ consistently with the (2+1)-D DP class exponent $\beta_{DP} = 0.580(4)$. (inset) The same data in the log-log scale with the horizontal axis set to ϵ. (d) The correlation length (left) and the correlation time (right) in the steady state plotted against ϵ. The correlation length was measured in the direction of the director field without voltage. The broken lines are guides for the eyes showing the estimated exponents. The estimated values of the exponents are consistent with the (2+1)-D DP class exponents $\nu_\parallel = 1.287(2)$ and $\nu_\perp = 0.729(1)$. The figures are adopted from Ref. [38] with permission.

3.1.2 Directed percolation, interface growth and stochastic Fisher–Kolmogorov–Petrovsky–Piscounov equation

Let us consider a situation where a cluster of the active sites is invading the inactive phase. The following two observations let us conjecture that the interface fluctuation of the (1+1)-D KPZ class appears in models showing the (2+1)-D DP class transition.

- First, let us reconsider the contact process on a two-dimensional lattice we discussed at the beginning of the previous subsection. In the case where the inactivation rate is negligible as $\gamma \to \infty$, the dynamics is similar to that of an interface growth model called Eden model [4, 6, 133, 134] which belongs to the KPZ class.
- Next, as remarked in [135], both of the DP transition and the KPZ interface growth appears with the DSM2 in LC electroconvection. Although one needs to be careful about the fact that they were conducted with the different alignment of LC director fields, those results imply a relationship between the (2+1)-D DP and (1+1)-D KPZ classes.

In order to obtain a more transparent viewpoint on the interface growth observed in the DP class, let us turn our attention to the standard Langevin equation for the DP class [120, 121], describing the local density of the active site $\rho(\mathbf{x}, t)$ at position $\mathbf{x}$ and time t, which reads

$$\partial_t \rho(\mathbf{x}, t) = \kappa\rho - \lambda\rho^2 + \bar{D}\triangle\rho + \bar{\Gamma}\sqrt{\rho}\eta(\mathbf{x}, t), \tag{3.7}$$

where $\eta(\mathbf{x}, t)$ is the white Gaussian noise satisfying

$$\langle\eta(\mathbf{x}, t)\rangle = 0,\ \langle\eta(\mathbf{x}', t')\eta(\mathbf{x}, t)\rangle = \delta(\mathbf{x}' - \mathbf{x})\delta(t' - t), \tag{3.8}$$

and the multiplicative noise is defined by the Itô product. The Langevin equation can be derived by taking a continuous limit of the contact process [126, 136], and the multiplicative noise $\propto \sqrt{\rho}$ can be understood as the consequence of the central limit theorem, since the density fluctuation depends on the density $\rho(\mathbf{x}, t)$ itself [120, 121].

When one considers the phase transition in $d < d_c = 4$, it is convenient to non-dimensionalize Eq. (3.7) into

$$\partial_T R(\mathbf{X}, T) = AR - R^2 + \triangle R + \sqrt{R}\eta(\mathbf{X}, T) \tag{3.9}$$

$$R(\mathbf{X}, T) := \frac{\rho(\mathbf{x}, t)}{\rho^*},\ X := \frac{x}{x^*},\ T := \frac{t}{t^*},\ A := \kappa t^* \tag{3.10}$$

where $x^* := \left(\bar{\Gamma}^2\lambda/\bar{D}^2\right)^{\frac{-1}{4-d}}$, $t^* := \left(\bar{\Gamma}^4\lambda^2/\bar{D}^d\right)^{\frac{-1}{4-d}}$, $\rho^* := (t^*)^{-1}\lambda^{-1}$, and the parameter A acts as the control parameter. There is the critical value A_c, such that the absorbing state $R_{\rm ss} = 0$ and the active phase $R_{\rm ss} > 0$ are realized for $A < A_c$ and $A > A_c$, respectively, where $R_{\rm ss}$

denotes the steady-state mean value of $R(\mathbf{X}, T)$ in a sufficiently (or precisely, infinitely) large system. One can control the noise amplitude instead of the coefficient of the linear term. With the proper scaling of the variables, the equation

$$\partial_T R(\mathbf{X}, T) = R - R^2 + \triangle R + B\sqrt{R}\,\eta(\mathbf{X}, T) \tag{3.11}$$

can be mapped to (3.10) with $A = B^{-\frac{4}{4-d}}$, indicating that the active phase is realized with sufficiently small noise amplitude $B < B_c$ where $B_c := A_c^{\frac{4}{4-d}}$.

It is instructive to see that the deterministic part of the DP Langevin equation (3.11)

$$\partial_T R(\mathbf{X}, T) = R - R^2 + \triangle R \tag{3.12}$$

is identical to the equation called Fisher–Kolmogorov–Petrovsky–Piscounov (FKPP) equation [137, 138] describing front propagation. In the one-dimensional case, Kolmogorov proved [138] that the solution of the FKPP equation

$$\partial_t f(x,t) = f(1-f) + \partial_x^2 f \tag{3.13}$$

with the step initial condition

$$f(x,0) = \begin{cases} 1 & (x < 0) \\ 0 & (x \geq 0) \end{cases} \tag{3.14}$$

converges to the traveling wave solution [Fig. 3.3(a)]

$$f(x,t) = g(x - 2t) \;\; (t \to \infty), \tag{3.15}$$

where the function $g(z)$ is determined by solving an associated ordinary differential equation with appropriate boundary conditions [139] [2]. Even for a higher (e.g. two-) dimensional case of (3.12), one can easily see that the traveling wave solution is realized with the initial condition such as

$$R(X,0) = \begin{cases} 1 & (x < 0) \\ 0 & (x \geq 0) \end{cases}, \; X =: (x, y). \tag{3.16}$$

Beyond the deterministic cases, it has long attracted attention how noise affects the growth of the front propagation of the FKPP equation. The natural form of the noise can be inferred by taking the continuous limit of a reaction model. We already found one example

[2] The convergence to the traveling wave solution has been proved for more general initial conditions in [140].

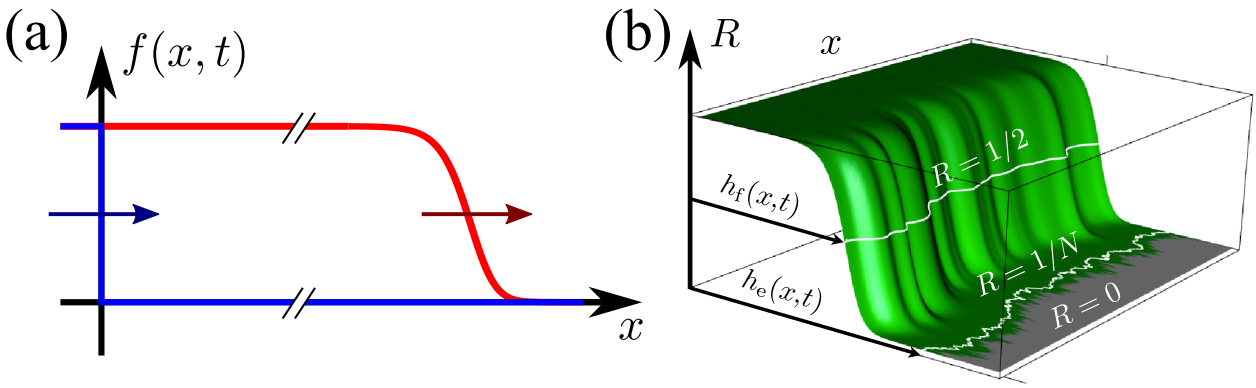

Figure 3.3: (a) Schematic illustration of the traveling-wave solution for FKPP equation 3.13. With the step initial condition (the blue line), the solution converges to the traveling-wave solution $g(x-2t)$ (the red line) moving with the velocity 2. (b) Numerically evaluated solution of the stochastic FKPP equation (3.18) in two-dimensional space [141]. The equipotential lines with $\rho = 1/2$ and $\rho = 1/N := B^{-2}$ are shown by the white lines. The figure is adopted from [141] with modifications with permission of American Physical Society.

$\propto \sqrt{R}\eta$ with the contact process. Another choice of the noise term is the form of

$$\partial_T R(\mathbf{X},T) = A(R-R^2) + D\triangle R + \sqrt{R-R^2}\eta(\mathbf{X},T) \tag{3.17}$$

or equivalently (with proper rescaling of the variables and $B \propto D^{-d/4}A^{(d-2)/2}$),

$$\partial_T R(\mathbf{X},T) = R - R^2 + \triangle R + B\sqrt{R-R^2}\eta(\mathbf{X},T) \tag{3.18}$$

which naturally arises from, for example, coarse-graining a reaction $a \rightleftarrows 2a$ of a particle a with spatial diffusion [142, 143]. This Langevin equation can be regarded as the standard equation for the absorbing phase transition called compact directed percolation class (CDP) characterized by two symmetric absorbing states $R = 0$ and $R = 1$, whose critical point is $A = 0$ [121]. Here we call Eq. (3.17) and (3.18) the CDP Langevin equation.

The FKPP equation with the noise term such as Eq. (3.11) and (3.18) [stochastic FKPP (sFKPP) equation] has been studied in various contexts. Especially, the asymptotic velocity of the traveling wave in the one-dimensional cases has been extensively studied. For example, the exact velocity is known for the weak-noise limit $B \to 0$ (far from the critical point) in the DP and CDP Langevin equations [Eq. (3.11) and (3.18)] [144, 145] and the strong-noise limit in the CDP Langevin equation [146, 147]. For the two-dimensional case, which is relevant for this study, several numerical studies have been conducted in the context of the interface growth. S. Nesic and the collaborators numerically demonstrated that the interface of the solution of the 2-D CDP Langevin equation (3.18) in the weak noise limit $B \to 0$ [$h_e(x,t)$ and $h_f(x,t)$ in Fig. 3.3(b)] belongs to the KPZ class with the fluctuation amplitude and characteristic lengthscale scaling as $\sim (-\log B)^{1/2}$ and $\sim -\log B$, respectively [141], which are generally not negligible even with small B. Also, E. Moro investigated a discrete model

whose continuous limit is the CDP Langevin equation (3.17) and observed that the stationary interface fluctuation agrees with that of the KPZ interfaces in the case of $d = 2$ [143]. They also investigated a model which corresponds to the DP Langevin equation (3.10) far above the transition threshold $A \gg A_c$, where they also observed the KPZ stationary fluctuation [143].

3.1.3 Motivation

Although the examples presented above suggest that the KPZ fluctuation appears in the systems which belong to the DP class far from the critical point, to our knowledge no study has elucidated the interface fluctuation that appears near the transition point, where the universality in a sense of the DP class arises. In particular, it is still not known whether the KPZ fluctuation survives in the situation where the system is near the transition point, and if it does, how the fluctuations of the DP class and the KPZ class are related to each other.

In this study, we aim to explicitly answer those questions by extensive simulations of the two-dimensional DP Langevin equation with the active boundary condition, a boundary condition such that $\rho(\mathbf{x}, t)$ at the boundary is always set to active. We investigate the interface fluctuation of the active phase growing from the boundary, with the interface height being intuitively defined as the maximum distance between an active site and the boundary. We describe the statistical properties of the interfaces in terms of the scaling functions of the DP transition, which are expected to be observed universally for systems in the DP universality class. We finally remark a conjecture arose from our study about a universal relationship between the non-universal parameters for the DP class and the KPZ class.

3.2 Methods

In this section, we explain the numerical scheme we used for the simulation of the DP Langevin equation, and describe the conditions we used to investigate the interface fluctuation.

3.2.1 Splitting-step method for directed percolation Langevin equation

We simulated the non-dimensionalized version of the DP Langevin equation

$$\partial_t \rho(x, y, t) = A\rho - \rho^2 + \triangle\rho + \sqrt{\rho}\eta(x, y, t) \tag{3.10}$$

with varied A, where $\eta(x, y, t)$ is a white Gaussian noise satisfying $\langle \eta(x, y, t) \rangle = 0$, $\langle \eta(x', y', t'), \eta(x, y, t) \rangle = \delta(x - x')\delta(y - y')\delta(t - t')$. We approximated the spacial deriva-

tive by the finite difference method to obtain

$$\frac{\mathrm{d}}{\mathrm{d}t}\rho_{i,j}(t) = A\rho_{i,j} - \rho_{i,j}^2 + \triangle\rho_{i,j} + \frac{1}{\Delta x}\sqrt{\rho_{i,j}}\eta_{i,j}(t) \tag{3.19}$$

where $\rho_{i,j}(t) := \rho(i\Delta x, j\Delta x, t)$, $\triangle\rho_{i,j}(t) := \frac{1}{(\Delta x)^2}\left[\left(\sum_{k=-1,1}\sum_{l=-1,1}\rho_{i+k,j+l}(t)\right) - 4\rho_{i,j}(t)\right]$ and $\eta_{i,j}(t)$ is a white Gaussian noise satisfying $\langle\eta_{i,j}(t)\rangle = 0$, $\langle\eta_{i',j'}(t')\eta_{i,j}(t)\rangle = \delta_{i',i}\delta_{j',j}\delta(t'-t)$. The prefactor $\frac{1}{\Delta x}$ in the last term is placed so that the stochastic term is stochastically the same as the spatially averaged noise term of the continuous version $\frac{1}{(\Delta x)^2}\int_x^{x+\Delta x}\mathrm{d}x'\int_y^{y+\Delta x}\mathrm{d}y'\eta(x',y',t)$.

Regarding the time discretization, it is known that the naïve Euler-type time discretization with approximating the noise term by a Gaussian random variable $\mathcal{N}_{i,j}(t)$ with the zero mean and the unit variance as

$$\rho_{i,j}(t+\Delta t) = \rho_{i,j}(t) + \left[A\rho_{i,j} - \rho_{i,j}^2 + \triangle\rho_{i,j}\right]\Delta t + \frac{(\Delta t)^{1/2}}{\Delta x}\sqrt{\rho_{i,j}}\mathcal{N}_{i,j}(t), \tag{3.20}$$

is not appropriate, since there is a finite probability of breaking the non-negativity condition $\rho(x,y,t) \geq 0$ that is a crucial property for the solution of the DP Langevin equation. To avoid this problem, we used a scheme proposed in Ref. [148] which is the operator splitting method [149] that splits the terms into groups each of which can be exactly treated and integrate the terms group by group. The steps of the algorithm for a single timestep Δt are conducted as follows:

1. In Eq. (3.19), we first integrate the terms $A\rho_{i,j} + \triangle\rho_{i,j} + \frac{1}{\Delta x}\sqrt{\rho_{i,j}}\eta_{i,j}(t)$ by integrating the stochastic differential equation (SDE)

$$\frac{\mathrm{d}}{\mathrm{d}t}\rho(t) = \beta\rho + \alpha_{i,j} + \frac{1}{\Delta x}\sqrt{\rho}\eta_{i,j}(t) \tag{3.21}$$

with the initial condition $\rho(0) = \rho_{i,j}(t)$ for the timestep Δt, where $\alpha_{i,j} := (\Delta x)^{-2}\sum_{k=-1,1}\sum_{l=-1,1}\rho_{i+k,j+l}(t)$ is treated as a constant and $\beta := A - \frac{4}{(\Delta x)^2}$. This step is conducted by using the exact solution for the Fokker-Plank equation of the SDE (3.21), which leads to the expression for $\rho^* := \rho(\Delta t)$ [148],

$$\rho^* = \mathrm{Gamma}\left[\mu + 1 + \mathrm{Poisson}\left[\lambda\omega\rho(0)\right]\right]/\lambda \tag{3.22}$$

where $\mathrm{Gamma}[z]$ is a random variable following the gamma distribution with the shape parameter z and the scale parameter 1, $\mathrm{Poisson}[w]$ is a random variable following the Poisson distribution with the mean w, $\mu := -1 + 2\alpha_{i,j}(\Delta x)^2$, $\lambda := \frac{2\beta(\Delta x)^2}{\omega - 1}$ and $\omega := \mathrm{e}^{\beta t}$.

2. We then integrate the remaining part $-\rho_{i,j}^2$ for the timestep Δt by solving $\mathrm{d}_t\rho(t) = -\rho^2$ with the initial condition $\rho(0) = \rho^*$ to obtain

$$\rho_{i,j}(t+\Delta t) = \rho(\Delta t) = \frac{\rho^*}{1+\rho^*\Delta t}. \tag{3.23}$$

It has been shown that this algorithm preserves the non-negativity of the solution, and that the result of this algorithm converges to the solution of the original SDE as the timestep Δt is sent to 0 with the error in the order of $\mathcal{O}(\Delta t)$ [148, 150].

3.2.2 Numerical setup and parameters

Quench simulation

In order to confirm the basic properties of the DP critical phenomena and estimate the system-dependent geometric factors, we first conducted the quench simulation [120, 121], in which the system evolved from the initial state such that the value of $\rho(x, y, 0)$ was uniformly set to a constant 1. The system size was set to 8192×8192 with the periodic boundary condition (PBC), and the Δx and Δt was varied as described later in Sec. 3.3.1. at least 10 independent simulations were conducted for each set of parameter values.

Interface growth simulation

We then simulated the Langevin equation with the active boundary condition with the geometry illustrated in Fig. 3.4(a). The length of the interface L_x is set to $\geq 2^{17}$ (in most of the cases, 2^{18}) so that it is sufficiently larger than the correlation lengths in the sense of the DP and KPZ classes. The PBC was imposed with respect to x. For each simulation, $\rho(x, y, t)$ of the sites except those at the boundary was initially set to 0, and the growth of the active phase from the boundary was simulated. L_y is determined so that the value of ρ at sites $y = L_y$ are always zero in order to avoid the effect from the boundary. The value of ρ at the boundary $y = 0$ is always set to a fixed value ρ_{bo}, which was varied as described in Sec. 3.4. 4 independent simulations were conducted for each set of parameter values.

Since y such that $\rho(y, t) > 0$ is proved to be finite almost surely for the one-dimensional DP Langevin equation [151] for a class of initial conditions, we assumed that the region $\rho(x, y, t) > 0$ is bounded with respective to y also in the two-dimensional cases, and defined the height of the interface $h(x, t)$ as

$$h(x, t) := \arg\max_{y} [\rho(x, y, t) > 0] \tag{3.24}$$

where $\arg\max_{y} f(y)$ means the value of y such that $f(y)$ takes the maximum value [3]. The configurations of the active sites satisfying $\rho(x, y, t) > 0$ and the shape of the interfaces are exemplified in Fig. 3.4(b).

[3] Defining the interface by thresholding with a non-zero value of ρ did not alter our results significantly, while the systematic investigation is ongoing.

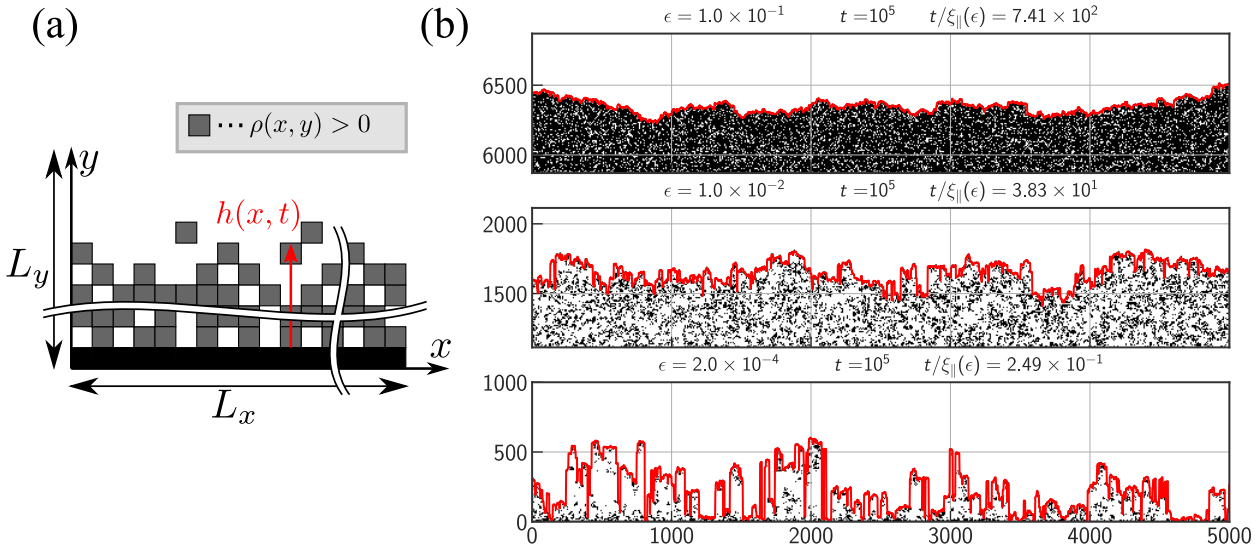

Figure 3.4: (a) The configuration for the simulation. The DP Langevin equation is simulated in a lattice of the size $L_x \times L_y$. The value of $\rho(x, y, t)$ is always set to $\rho_{\rm bo}$ at $y = 0$ (active boundary condition). The interface height $h(x, t)$ is defined as the maximum distance between the boundary and the site (x, y) satisfying $\rho(x, y, t) > 0$. (b) Snapshots of the interfaces (red lines) and the configuration of the active sites satisfying $\rho(x, y, t) > 0$ (black patches) plotted together. The value of ϵ and the time t is denoted above the images, respectively.

3.3 Quench simulation and validation of basic properties

In this section, we describe the results for the quench simulation conducted in order to estimate the basic properties such as the transition point, the correlation time and correlation length.

3.3.1 Estimation of transition point

Figure 3.5(a) shows the mean value of rho $\langle \rho(x, y, t) \rangle$ in the quench simulation for various values of A with $\Delta t = 0.25$, $\Delta x = 3$. In agreement with the knowledge of the DP-class transitions [120, 121], there is a critical value A_c of A (red curve) above which $\langle \rho(x, y, t) \rangle$ converges to a constant value and below which it decreases superalgebraically. The slope at $A = A_c$ was consistent with the prediction by the DP scaling ansatz, $\sim t^{-\alpha_{\rm DP}}$ where $\alpha_{\rm DP} := \beta_{\rm DP}/\nu_\parallel$ [120, 121].

The precise value of A_c was estimated by plotting $t^{\alpha_{\rm DP}} \langle \rho(x, y, t) \rangle$ against the time and finding the value of A such that the curve becomes parallel to the horizontal axis [Fig. 3.5(b)]. We found

$$A_c = 0.18136(1). \tag{3.25}$$

By rescaling the density $\langle\rho(x,y,t)\rangle$ and the time t according to the DP scaling ansatz as $|\epsilon|^{-\beta_{\rm DP}}\langle\rho(x,y,t)\rangle$ and $|\epsilon|^{\nu_\parallel} t$, respectively, all the curves were collapsed onto the scaling functions [Fig. 3.5(c)] confirming that the DP scaling ansatz is valid for this simulation.

It should be remarked that one needs to be careful about the fact that the value of A_c depends on the choice of Δt and Δx as shown in Fig. 3.6. While the dependence on Δt was rather small and in the order of $\mathcal{O}(\Delta t)$ consistently with the results shown in [148, 150], we found rather large ($\approx 50\%$) change of the value of A_c with respect to Δx as we varied Δx form 1 to 4. In this study, since we are interested in the universal feature generally applicable for a model in the DP class, we just used $\Delta t = 0.25$ and $\Delta x = 3$ with remarking that it might be necessary to use finer spatial lattice if one is interested in the behavior in the continuous limit.

3.3.2 Estimation of non-universal parameters for directed percolation Langevin equation

For the sake of writing our results as a nondimensional scaling functions (3.6) that is expected to be universal for systems in the DP class, we further defined and estimated the metric factors for the density, correlation length and correlation time from the result of the quench simulations.

We first defined the metric factor for the density ρ_0 so that the steady-state density $\rho_{\rm ss}$ above the critical point satisfies $\rho_{\rm ss} \simeq \rho_0 \epsilon^{\beta_{\rm DP}}$. We plotted $\epsilon^{-\beta_{\rm DP}}\langle\rho(\mathbf{x},t)\rangle$ for the data with sufficiently large $\epsilon^{\nu_\parallel} t$ and empirically found the line regression

$$\epsilon^{-\beta_{\rm DP}}\langle\rho(\mathbf{x},t)\rangle \simeq \rho_0 + \rho_1\epsilon \quad (\epsilon^{\nu_\parallel} t \gg 1) \tag{3.26}$$

$$\rho_0 = 0.168(1),\ \rho_1 = 0.17(3) \tag{3.27}$$

well describes the data within the uncertainty [Fig. 3.7(a)]. Hereafter we define $\rho_{\rm ss}(\epsilon) := \epsilon^{\beta_{\rm DP}}(\rho_0 + \rho_1\epsilon)$

Also, the metric factors t_0 and x_0 for the timescale and the length scale was defined so that the correlation time $\xi_\parallel(\epsilon) := t_0 |\epsilon|^{\nu_\parallel}$ and the correlation length $\xi_\perp(\epsilon) := x_0 |\epsilon|^{\nu_\perp}$ satisfies

$$\langle\rho(\mathbf{x},t)\rangle \sim \exp\left(-\frac{t}{\xi_\parallel(\epsilon)}\right) \quad (\epsilon < 0, |\epsilon|^{\nu_\parallel} t \gg 1) \tag{3.28}$$

$$\mathrm{Cov}[\rho(\mathbf{x}',t),\rho(\mathbf{x},t)] \sim \exp\left(-\frac{|\mathbf{x}'-\mathbf{x}|}{\xi_\perp(\epsilon)}\right) \quad (\epsilon > 0, |\epsilon|^{\nu_\parallel} t \gg 1). \tag{3.29}$$

Our estimation led $t_0 = 6.97(8)$ and $x_0 = 1.5(2)$ [Fig. 3.7(b-d)]. We note that it is possible to define the correlation length and the correlation time in other ways [120, 121], but the values can be converted to each other by multiplying universal constants that we can estimate from numerical simulation of a model in the DP class.

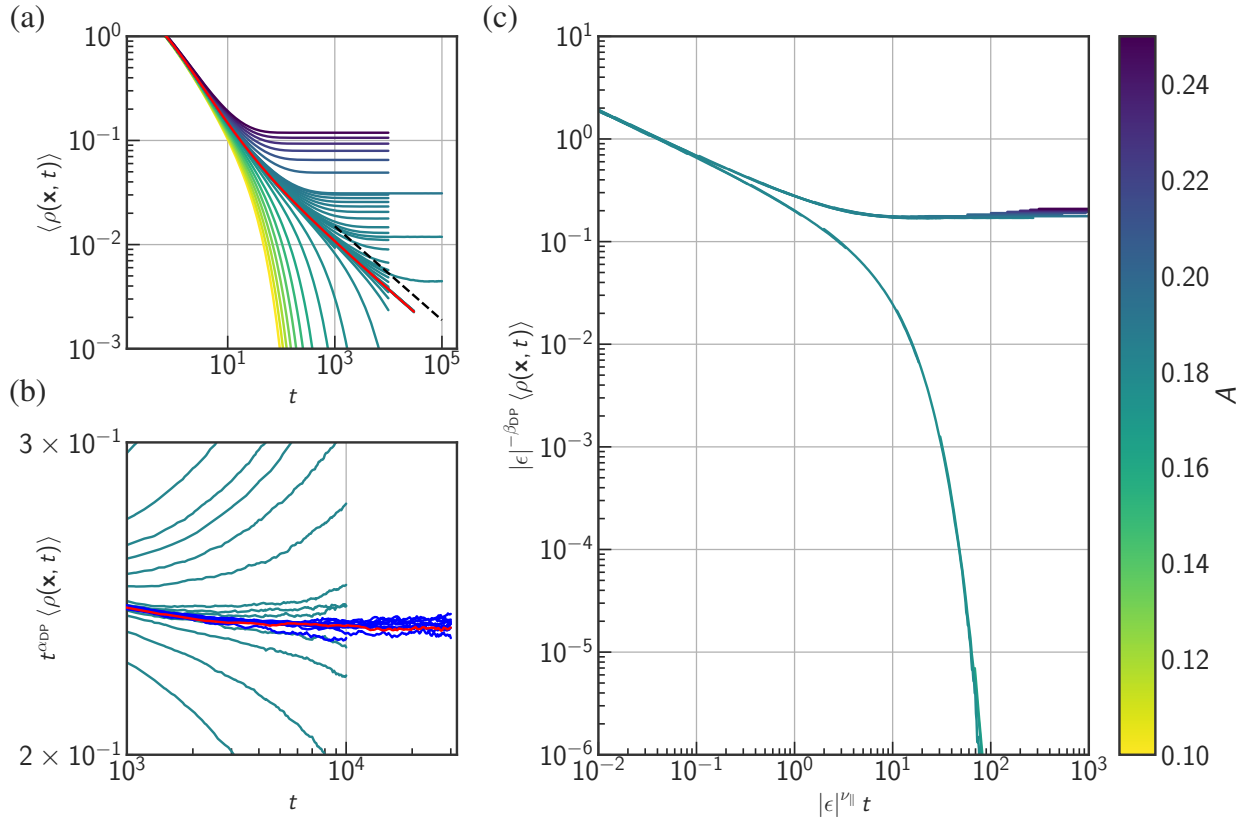

Figure 3.5: The estimation of the transition point for the DP Langevin equation by a quench simulation with $\rho(x, 0) = 10$. The values of A is indicated by the color as color bar at the right of the plots. (a) The mean order parameter $\langle \rho(\mathbf{x}, t) \rangle$ plotted with time. The red line is the values with the critical control parameter $A = A_c$. the broken line is a guide for the eyes with the DP exponent $\propto t^{-\alpha_{\rm DP}}$. (b) The same data as (a), with the vertical axis rescaled by $t^{\alpha_{\rm DP}}$. The red line is the values with the critical control parameter $A = A_c$ and the blue lines are those with $|A - A_c| \leq \delta A$, where δA is the uncertainty of A. (c) The rescaled mean order parameter $|\epsilon|^{-\beta_{\rm DP}} \langle \rho(\mathbf{x}, t) \rangle$ plotted with the rescaled time $|\epsilon|^{\nu_\parallel} t$. The curves in (a) are rescaled onto a scaling function.

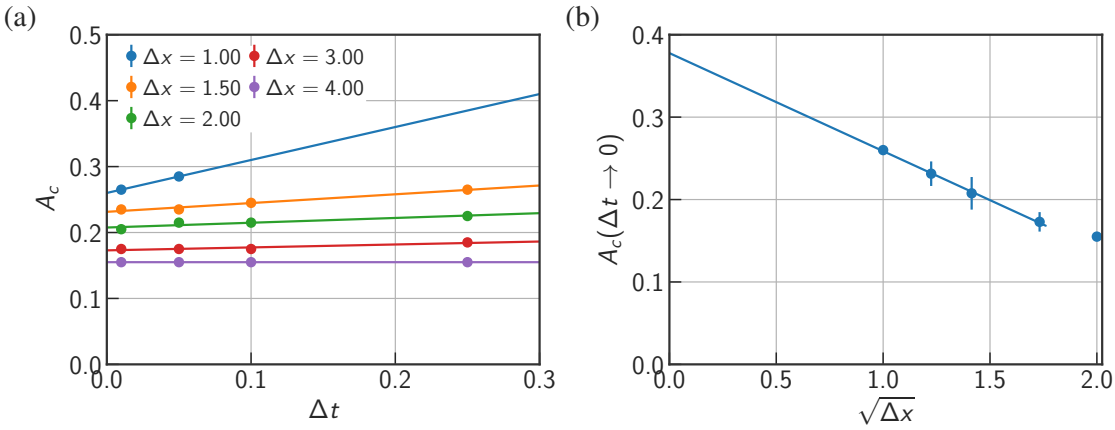

Figure 3.6: The dependence of the transition point A_c on Δt (a) and Δx (b). (a) The value of A_c plotted with Δt with varied Δx. The solid line is the result of the line regression, the color of which is the same as the color for the fitted data. (b) The value of the intercepts in the plot (a), $A_c(\Delta t \to 0)$ plotted with $\sqrt{\Delta x}$. It was empirically found that the values of A_c can be fitted by a linear function with respective to $\sqrt{\Delta x}$. The solid line is the result of the line regression.

3.4 Results and Analysis

In this section, we describe the results of the simulation investigating the growth of the active phase from the active boundary (Sec. 3.2.2).

3.4.1 Qualitative observation and spanwise averaged density

The examples of the configuration of the sites satisfying $\rho(x, y, t) > 0$ and the associated interface at time $t = 10^5$ are shown in Fig. 3.4(b). One can observe that the interface profile at the same time t is quite different for different values of ϵ. The interface appears to be rather continuous with a compact cluster behind it for the case where $\epsilon = 1.0 \times 10^{-1}$, whereas many apparent discontinuities are observed for the smaller value of $\epsilon = 1.0 \times 10^{-4}$.

Considering the spanwise averaged density

$$\bar{\rho}_x(y, t) := \left\langle \frac{1}{L_x \Delta x} \int_0^{L_x \Delta x} \rho(x, y, t) \mathrm{d}x \right\rangle \tag{3.30}$$

helps one to understand this change in the morphology. Figure 3.8 exemplifies the result of the simulation with $\rho_{\mathrm{bo}} = 1$. In the critical case $\epsilon = 0$, the density profile approaches to a power law. In the supercritical cases $\epsilon > 0$, the density profile deviates from that for the critical case at some timescale comparable to the correlation time $\xi_{\parallel}(\epsilon)$, and make a plateau whose density is close to ρ_{ss}. The edge of the plateau proceeds with time analogously to the traveling wave solution for the FKPP equation [Fig. 3.3(a)]. It is natural to expect that the qualitative change of the interface shape is accompanied by this crossover. We will confirm this statement later.

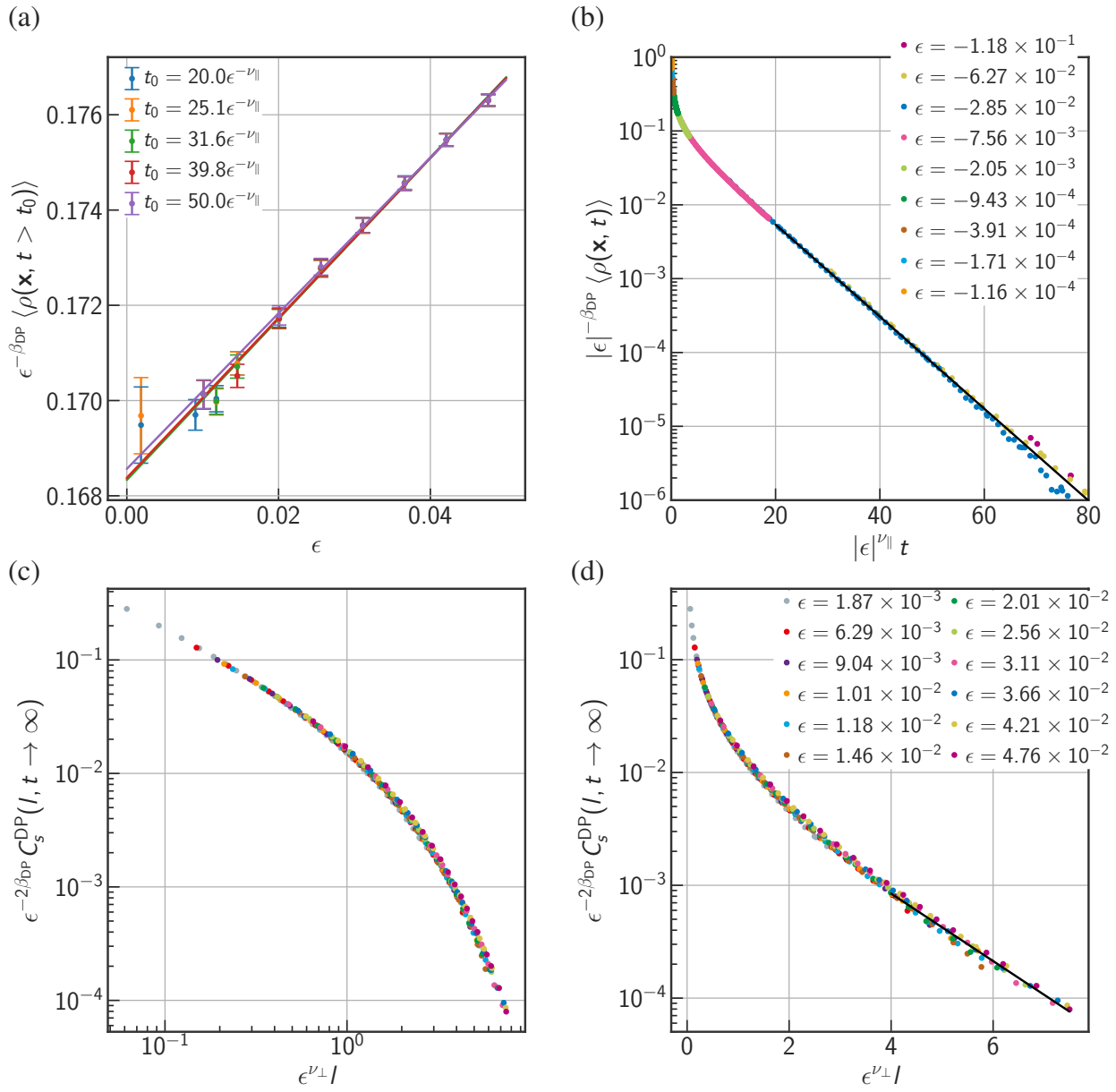

Figure 3.7: Estimation of the characteristic scales of the order parameter, time and length scales for the DP Langevin simulation. (a) The estimation of the characteristic scale of the order parameter. The mean order parameter $\langle \rho(x,t) \rangle$ averaged for data points with $t > t_0$, where t_0 is varied as shown in the legend of the plot. The solid line is the result of the line regression, where the color corresponds to the color of the fitted data points. (b) The estimation of the characteristic timescale. The rescaled mean order parameter $|\epsilon|^{-\beta_{\rm DP}} \langle \rho(\mathbf{x}, t) \rangle$ is plotted against the rescaled time $|\epsilon|^{\nu_\parallel} t$ for $A < A_c$ (the lower branch of Fig. 3.5(c)), in the semi-log scale. The black line is the result of the line regression. (c,d) The estimation of the characteristic length scale. The two-point covariance $\epsilon^{-2\beta_{\rm DP}} C_s^{\rm DP}(l,t)$ at sufficiently long time $\epsilon^{-\nu_\parallel} t > 10$ is plotted against the rescaled length $\epsilon^{\nu_\perp} l$, in the log-log scale (c) and semi-log scale (d). The black line in (d) is the result of the line regression.

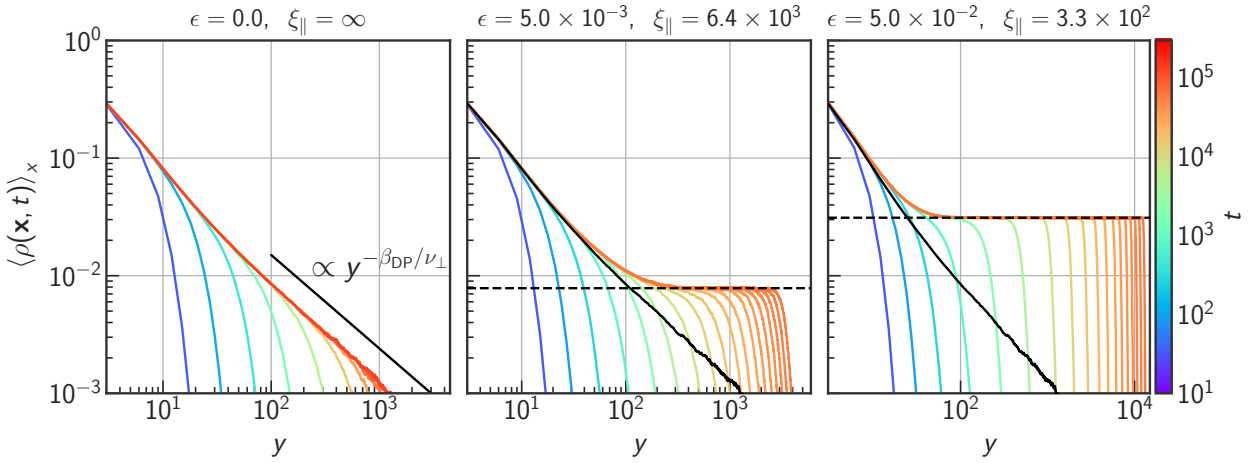

Figure 3.8: The order parameter $\rho(\mathbf{x}, t)$, averaged in the spanwise direction. The normalized control parameter ϵ and the correlation time $\xi_\parallel(\epsilon)$ is indicated upon each plot. The values of t is indicated by the color as color bar at the right of the plots. The black solid line in the left plot is a guild for the eyes with the exponent $\propto y^{-\beta_{\rm DP}/\nu_\perp}$. The black broken lines in the center and right plots indicate the values of the steady state density $\rho_{\rm ss}(\epsilon)$. The black lines in the center and the right plot is the data for the critical point $\epsilon = 0$ with $t = 290000$.

The behavior of the spanwise averaged density can be explained by the DP scaling ansatz. From Eq. (3.6), one can expect that $\bar{\rho}_x(y, t)$ is written in the scaling form [120, 121]

$$b^{\beta_{\rm DP}} \tilde{\bar{\rho}}_x(y, t) = f_{\bar{\rho}_x}(b^{-\nu_\perp} \tilde{y}, b^{-\nu_\parallel} \tilde{t}; b\epsilon) \tag{3.31}$$

where $\tilde{\bar{\rho}}_x(y, t) := \bar{\rho}_x(y, t)/\rho_0$, $\tilde{y} = y/x_0$ and $\tilde{t} = t/t_0$, which leads

$$\tilde{\bar{\rho}}_x(y, t) = \tilde{y}^{-\beta_{\rm DP}/\nu_\perp} f_{\bar{\rho}_x}(1, \tilde{y}^{z_{\rm DP}} \tilde{t}; \tilde{y}^{-1/\nu_\perp} \epsilon) \tag{3.32}$$

by taking $b = \tilde{y}^{-1/\nu_\perp}$, where $z_{\rm DP} := \nu_\parallel/\nu_\perp$. Substituting $\epsilon = 0$ and $t \to \infty$, we obtain the asymptotic power law $\tilde{\bar{\rho}}_x(y, t) \sim \tilde{y}^{-\beta_{\rm DP}/\nu_\perp}$, which is consistent with our numerical observation. Also, one can derive

$$\tilde{\bar{\rho}}_x(y, t) = \epsilon^{\beta_{\rm DP}} f_{\bar{\rho}_x}(y/\xi_\perp(\epsilon), t/\xi_\parallel(\epsilon); 1) \tag{3.33}$$

by taking $b = \epsilon^{-1}$. This representation suggests that $\xi_\parallel(\epsilon)$ is the characteristic timescale for the crossover from the critical power law to the traveling wave. In the following sections, we will see that this correlation time is indeed the characteristic timescale for the crossover of the interface fluctuation qualitatively observed in the beginning of this section.

3.4.2 Height cumulants

In order to elucidate the nature of the height distribution, we plotted the cumulants of the height $\langle h(x,t)^k \rangle_c$ for $k = 1, \ldots, 4$ (Fig. 3.9) for the cases where $\rho_{\rm bo} = 0.1, 1$ and 10. The data with different $\rho_{\rm bo}$ overlaps for large t, implying that the value of $\rho_{\rm bo}$ is not relevant in the long-time limit [4]. Two characteristic slopes were observed in the plot. One of which is consistent with a power law characterized by the DP exponents $\sim t^{k/z_{\rm DP}}$ and the other is consistent with the exponents for the KPZ scaling laws ($\sim t^{k\beta} = t^{k/3}$ for $k \geq 2$, $\sim t$ for $k = 1$ due to the linear growth). By rescaling the height and the time by the correlation length and the correlation time for the DP class as

$$h_\xi := h(x,t)/\xi_\perp(\epsilon),\ t_\xi := t/\xi_\parallel(\epsilon), \tag{3.34}$$

all the data for each k were collapsed onto a single curve whose slope amplitude crossovers from the DP exponents to the KPZ exponents (Fig. 3.10).

The following scaling arguments can explain these results. With the scaling ansatz (3.6), let us assume that the height of the interface $h(x,t)$ is written in the scaling form of

$$b^{-\nu_\perp}\tilde{h}(x,t) = f_h(b^{-\nu_\perp}\tilde{x}, b^{-\nu_\parallel}\tilde{t}; b\epsilon), \tag{3.35}$$

where $\tilde{h}(x,t) := h(x,t)/x_0$, $\tilde{t} := t/t_0$ and $\tilde{x} := x/x_0$. Then, setting $b = \epsilon^{-1}$, one obtains

$$h_\xi(x,t) = f_h(x/\xi_\perp(\epsilon), t/\xi_\parallel(\epsilon); 1) =: f'_h(x/\xi_\perp(\epsilon), t/\xi_\parallel(\epsilon)), \tag{3.36}$$

which leads to

$$\langle h_\xi(x,t)^k \rangle_c = \langle f'_h(x/\xi_\perp(\epsilon), t/\xi_\parallel(\epsilon))^k \rangle_c =: g_k(t_\xi), \tag{3.37}$$

consistently with the scaling collapse in Fig. 3.10. Our numerical results further suggest that $h_\xi(x,t)$ follows the KPZ scaling laws for $t > \xi_\parallel(\epsilon)$. Also, the short-time behavior can be explained by setting $b = \tilde{t}^{1/\nu_\parallel}$ in (3.35), which yields

$$h_\xi(x,t) = t_\xi^{1/z_{\rm DP}} f_h(t_\xi^{1/z_{\rm DP}} x_\xi, 1; t_\xi^{1/\nu_\parallel}) =: t_\xi^{1/z_{\rm DP}} f''_h(t_\xi^{1/z_{\rm DP}} x_\xi, t_\xi^{1/\nu_\parallel}) \tag{3.38}$$

and

$$\langle h_\xi(x,t)^k \rangle_c = t_\xi^{1/z_{\rm DP}} \left\langle f''_h(t_\xi^{k/z_{\rm DP}} x_\xi, t_\xi^{1/\nu_\parallel})^k \right\rangle_c =: t_\xi^{k/z_{\rm DP}} g'_k(t_\xi), \tag{3.39}$$

suggesting $\langle h(x,t)^k \rangle_c \sim t^{k/z_{\rm DP}}$ in the case of $t_\xi \ll 1$, assuming $\lim_{t_\xi \to 0} g'_k(t_\xi) = \text{const.} \neq 0$.

The crossover from the DP regime to the KPZ regime is accompanied by the change of the shape of the height distribution. In the left panels of Fig. 3.11, the skewness $\mathrm{Sk}[h(x,t)]$ and

[4] We note that the effect of the boundary condition (e.g. the density $\rho_{\rm bo}$ at the boundary) might be systematically treated by the scaling argument considering $\rho_{\rm bo}$ itself in the scaling function [120, 121].

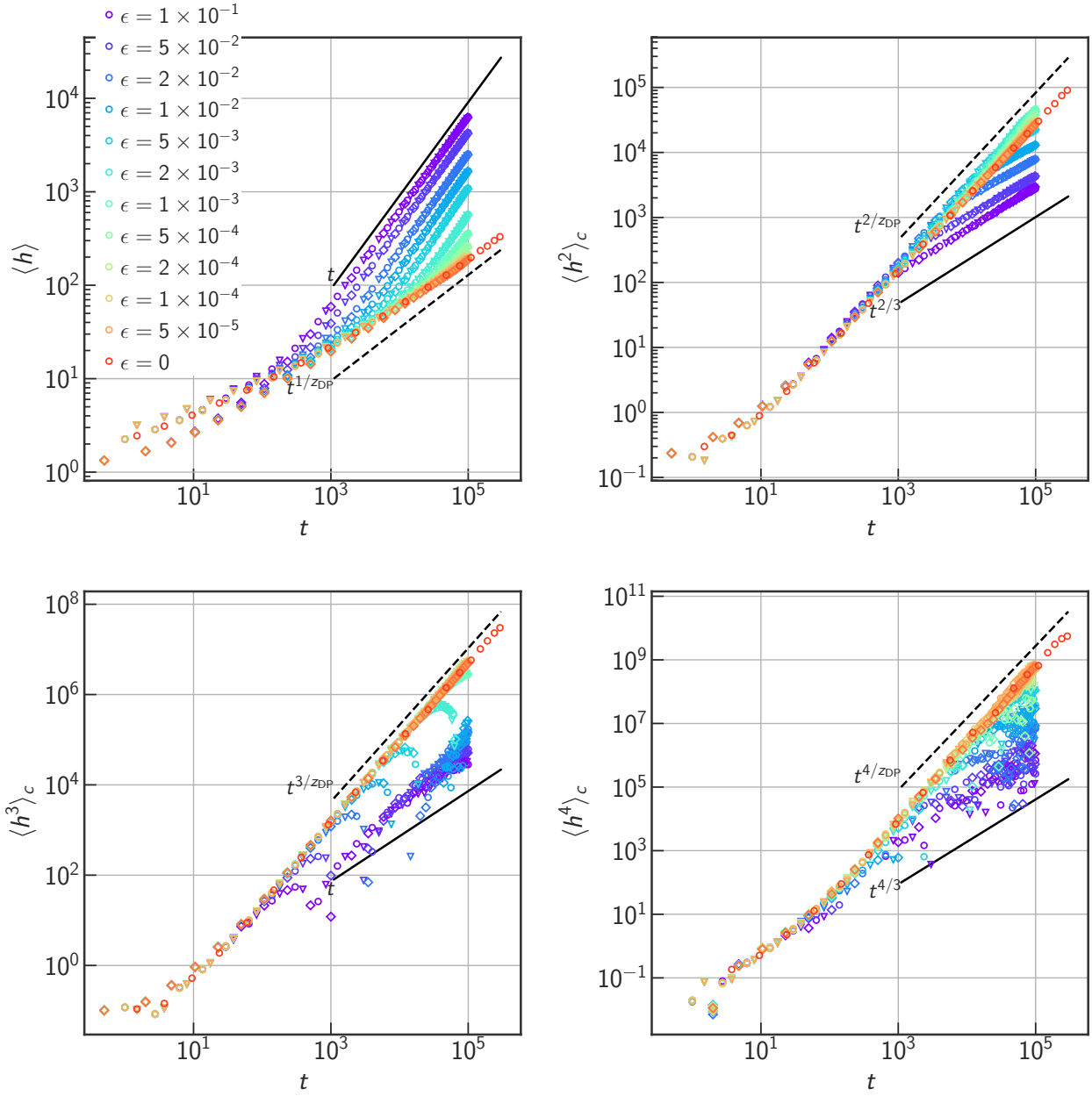

Figure 3.9: The cumulants of the height $\langle h(x,t)^k \rangle_c$ for $k = 1, \ldots, 4$ with the threshold $\rho_{\rm th} = 0$ and the boundary values of $\rho_{\rm bo} = 0.1$ (diamond) 1 (circle) and 10 (triangle). The black broken and solid lines are guides for the eyes with the DP dynamic exponent $k/z_{\rm DP}$ and the KPZ exponents [$k\beta = k/3$ for $k > 1$, 1 for $k = 1$ due to the linear growth], respectively.

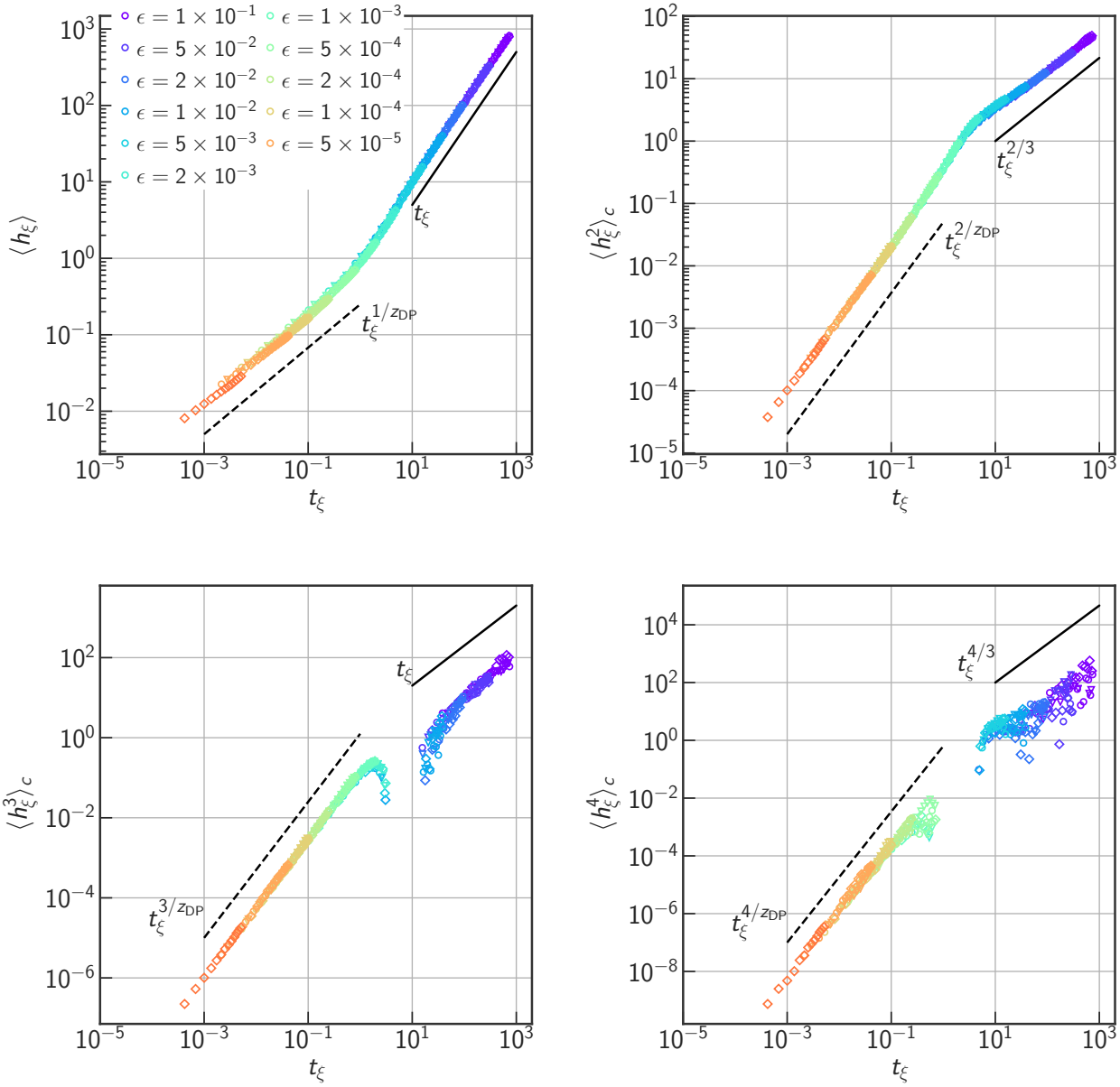

Figure 3.10: The cumulants of the rescaled height $\langle h_\xi(x,t)^k \rangle_c = \langle h(x,t)^k \rangle_c / \xi_\perp(\epsilon)^k$ plotted against the rescaled time $t_\xi = t/\xi_\parallel(\epsilon)$ for $k = 1, \ldots, 4$. The values of $\rho_{\rm th}$ and $\rho_{\rm bo}$ are the same as those in Fig. 3.9, but only data with $t > 5 \times 10^3$ are plotted for the sake of visualization. The black broken and solid lines are guides for the eyes with the DP dynamic exponent $k/z_{\rm DP}$ and the KPZ exponents [$k\beta = k/3$ for $k > 1$, 1 for $k = 1$ due to the linear growth], respectively.

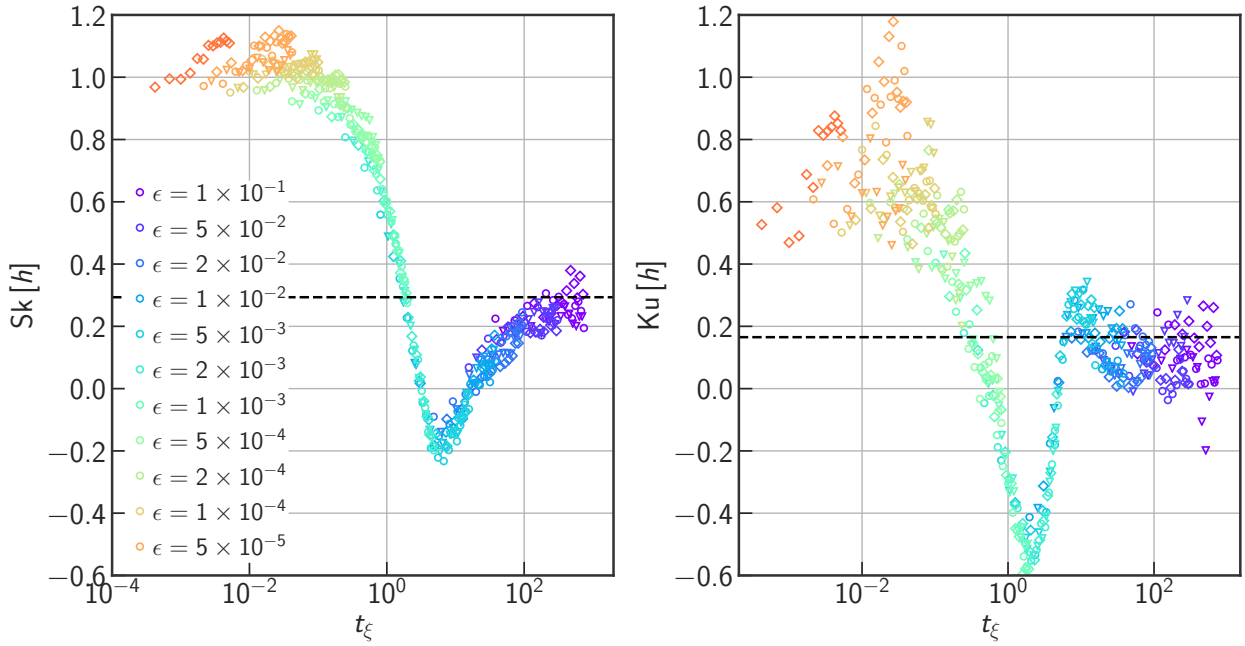

Figure 3.11: The skewness Sk[h] and kurtosis Ku[h] of the height for the (a) $\epsilon > 0$ and (b) $\epsilon = 0$ (critical) interfaces, plotted against (a) the rescaled time $t_\xi = t/\xi_\parallel(\epsilon)$ and (b) the time t, respectively. Only data with $t > 5 \times 10^3$ are plotted for the sake of visualization. The broken lines indicates the values of the exact solution for the flat KPZ interfaces, the GOE-TW distribution (2.11).

the kurtosis $\mathrm{Ku}[h(x,t)]$ are plotted against the rescaled time t_ξ. It is clearly observed that the values of the skewness and the kurtosis approach to the values of the exact solution of the KPZ class, the GOE-TW distribution (χ_1, Sec. 2.1.1), consistently with the scaling exponents. Also, although the data points are rather scattered, the values appear to take constant values in the DP regime $t_\xi \ll 1$, implying the existence of a universal height distribution in the limit of $t_\xi \to 0$.

3.4.3 Universal relationship between non-universal parameters

Finally, we remark the relationship between the non-universal parameters for the KPZ interface growth and the those for the DP transition. The scaling form (3.35) suggests that when the length scales and timescales are respectively rescaled by the correlation length and the correlation time, the statistical properties of the interface are invariant with respect to the change of the ϵ. Thus, by dimensional analysis, we can naturally expect that the non-universal parameters in terms of the KPZ class, the asymptotic velocity v_∞, the fluctuation amplitude Γ and the amplitude of the stationary Brownian motion A [See Eq. (2.5)] depends on the correlation length $\xi_\perp(\epsilon)$ and the correlation time $\xi_\parallel(\epsilon)$ of the DP class as

$$v_\infty = \gamma_v \frac{\xi_\parallel(\epsilon)}{\xi_\perp(\epsilon)}, \quad \Gamma = \gamma_\Gamma \frac{\xi_\perp(\epsilon)^3}{\xi_\parallel(\epsilon)}, \quad A = \gamma_A \xi_\perp(\epsilon) \tag{3.40}$$

where γ_v, γ_Γ and γ_A are constants that are universal if one fixes the definition of the metric factors. The relationship suggests the power laws for the non universal parameters

$$v_\infty \sim \epsilon^{\nu_\perp - \nu_\parallel}, \quad \Gamma \sim \epsilon^{\nu_\parallel - 3\nu_\perp}, \quad A \sim \epsilon^{-\nu_\perp}. \tag{3.41}$$

This relationship further suggests that one can predict the statistical properties of the interfaces of the active phase, only by estimating the correlation length and the correlation time by, for example, the quench experiment or simulation. This observation also suggests that the properties of the critical fluctuation in the bulk might be inferred from the evolution of the interface fluctuation.

3.5 Summary and discussions

In this chapter, we investigated the growth of active phase from an active boundary in 2-D DP Langevin equation. The interface of the active phase was simply defined as the set of active sites mostly distant from the active boundary.

We found that the statistical properties of the fluctuation of the interface show a crossover from the DP regime ($t/\xi_\parallel(\epsilon) \ll 1$) where both of the mean height and the amplitude of the fluctuation is characterized by the DP dynamic correlation length $\sim t^{1/z_{\mathrm{DP}}}$ to the KPZ regime ($t/\xi_\parallel(\epsilon) \gg 1$) where the mean height grows linearly $\sim t$ and the fluctuation amplitude follows the (1+1)-D KPZ-class scaling $\sim t^{1/3}$. The skewness and the kurtosis of the height

distribution were consistent with those of the GOE-TW distribution, the exact solution for the flat KPZ interfaces in the KPZ regime. On the other hand, they seemed to take the different constant values in the DP regime $t/\xi_{\parallel}(\epsilon) \ll 1$, suggesting the existence of another universal distribution which appears in the DP regime. With the scaling relation, we conjectured the universal relationship between the non-universal parameters of the DP and KPZ classes.

Finally, we discuss future perspectives. Since we focused solely on the DP Langevin equation, the universality of the scaling form of the interface height $h_\xi(x_\xi, t_\xi)$ is one subject that we need to confirm. The found that results obtained from simulations of the bond percolation model [120, 121], at least qualitatively, consistent with the phenomena observed in the DP Langevin equation [152]. The quantitative comparison with estimating the metric factors x_0 and t_0 is desirable.

It would be also interesting to ask about the generality of the KPZ fluctuation for other absorbing phase transition in the regime $t/\xi_{\parallel}(\epsilon) \gg 1$. Numerical simulation of the biased voter model, a model which belongs to the CDP universality class [120, 121] suggests the existence of the similar scaling functions of the height cumulants with the KPZ-class scaling in the regime $t/\xi_{\parallel}(\epsilon) \gg 1$ [153] (where $\xi_{\parallel}(\epsilon)$ is the correlation time for the CDP class), implying that those properties are generally found for absorbing phase transitions with short-ranged dynamical rules.

Considering application to the experimental systems such as the laminar-turbulent transition in channel flow [128], It is of crucial importance to investigate the effect of the advection [154, 155], which can significantly affect of the growth of the active phase [154]. Also, a future study investigating other initial conditions such as the half-active condition $\rho(x, y, t) = \rho_{\text{init}}(y > 0),\ 0(y < 0)$ would be instructive to capture the phenomenology of the interface growth.

Chapter 4

Conclusion and outlook

Throughout this dissertation, the author aimed to elucidate mutual relationships between different universal fluctuations in nonequilibrium systems to extend our knowledge on the universality emerging from scale invariance. Particularly, we experimentally and numerically studied universal scale-invariant fluctuations which appear in growing interfaces, with special attention to the (1+1)-D KPZ universality class. In Chapter 2 and Chapter 3, I presented experimental and numerical results that generalizes our understanding of universal fluctuations of the KPZ class in the scaling limit. In the following, I briefly summarize the conclusion for each chapter, and discuss the significance, generality and long-term future perspectives.

Chapter 2: Generalization of flat and circular KPZ subclasses

In Chapter 2, we focused on the geometry dependence of the universal fluctuation of the $(1 + 1)$-D KPZ class. To investigate the fluctuation of the KPZ class with general initial conditions experimentally, I constructed the experimental setup with which we can study the growing interface of the DSM2 in the LC electroconvection with arbitrary-designed initial conditions. Experimentally with this setup and numerically by the simulation of the off-lattice Eden model, I investigated the growth of the KPZ interfaces with the ring-shaped initial conditions, which naturally generalizes the special cases of the circular and the flat interfaces.

We found that the rescaled timescale $\tau := v_\infty t/R_0$ governs the height distribution and the spatial correlation. For both of the ingrowing and outgrowing cases, the interfaces showed the statistical properties of the flat interfaces with $\tau \ll 1$. On the other hand, the departure from the flat subclass was observed for $\tau \sim 1$; The statistical properties of the outgrowing interfaces approached those of the circular interfaces in the limit of $\tau \to \infty$, whereas those of the ingrowing interfaces seemingly diverged with no sign of the circular subclass. We found that the theory derived from the variational formula reasonably explains our observations, and predicts the same statistical properties generally for curved initial conditions.

Notably, to our knowledge, this study is the first experimental illustration that the variational formula was utilized to understand the KPZ-class fluctuation beyond the standard

flat, circular and stationary subclasses. Our study suggest that it provides us a novel way to interconnect the theory and experiments of the KPZ interfaces. For example, we expect that it is also possible to conjecture a variational representation of the height distribution from the experimental or numerical observations. It may be also intriguing to ask whether the similar formulation for geometry-dependent fluctuation exists for other universality classes for nonequilibrium systems. In this direction, it may be essential to consider the generalization of the variational formula for the KPZ class, which relies on the linearity of the stochastic heat equation, a spatial property of the KPZ equation.

Chapter 3: Crossover to KPZ fluctuation in DP active phase growth

In Chapter 3, we studied the interface of the active phase for the $(2+1)$-D DP transition, growing from the active wall into the inactive phase. We found that the interface fluctuation shows the crossover connecting the regime characterized by the exponents associated with the DP class and the regime with the $(1+1)$-D KPZ-class fluctuation. The scaling collapse of the data suggests the universality of the height fluctuation generally for the systems in the DP class. The height distribution showed crossover connecting that in the DP regime, which is yet to be fully characterized, toward that for the KPZ flat interfaces, the GOE-TW distribution.

Our results suggest an intuitive picture that the correlation time and the correlation length acts as the "building block" of in the sense of the KPZ interface. In other words, there seems to be a hierarchical structure of the universal fluctuation, where the large-scale scale invariant fluctuation (the KPZ class) is built by units whose typical length scale (and the timescale) is the correlation length (and the correlation time) in the for the original phase transition (DP class). It may be interesting to consider how one can theoretically understand this situation by coarse-graining the original microscopic model or the Langevin equation to extract the interface fluctuation we observed.

Overall, I hope the studies presented in this dissertation will be an inspiration to extend our knowledge toward more general understanding of scale-invariance-associated universality in nonequilibrium systems.

Bibliography

[1] K. G. Wilson, "Renormalization Group and Critical Phenomena. I. Renormalization Group and the Kadanoff Scaling Picture", *Phys. Rev. B* **4**, 3174 (1971).

[2] K. G. Wilson, "Renormalization Group and Critical Phenomena. II. Phase-Space Cell Analysis of Critical Behavior", *Phys. Rev. B* **4**, 3184 (1971).

[3] A. Pelissetto and E. Vicari, "Critical Phenomena and Renormalization-Group Theory", *Physics Reports* **368**, 549 (2002).

[4] A.-L. Barabási and H. Eugene Stanley, *Fractal Concepts in Surface Growth* (Cambridge University Press, New York, 1995).

[5] K. A. Takeuchi, "Experimental approaches to universal out-of-equilibrium scaling laws: turbulent liquid crystal and other developments", *J. Stat. Mech. Theor. Exp.* **2014**, P01006 (2014).

[6] F. Family and T. Vicsek, "Scaling of the active zone in the Eden process on percolation networks and the ballistic deposition model", *J. Phys. A: Math. Gen.* **18**, L75 (1985).

[7] M. Kardar, G. Parisi, and Y.-C. Zhang, "Dynamic scaling of growing interfaces", *Phys. Rev. Lett.* **56**, 889 (1986).

[8] J.-i. Wakita, H. Itoh, T. Matsuyama, and M. Matsushita, "Self-Affinity for the Growing Interface of Bacterial Colonies", *J. Phys. Soc. Jpn.* **66**, 67 (1997).

[9] M. Matsushita, J. Wakita, H. Itoh, I. Ràfols, T. Matsuyama, H. Sakaguchi, and M. Mimura, "Interface growth and pattern formation in bacterial colonies", *Physica A* **249**, 517 (1998).

[10] J. Maunuksela, M. Myllys, O.-P. Kähkönen, J. Timonen, N. Provatas, M. J. Alava, and T. Ala-Nissila, "Kinetic Roughening in Slow Combustion of Paper", *Phys. Rev. Lett.* **79**, 1515 (1997).

[11] P. L. Schilardi, O. Azzaroni, R. C. Salvarezza, and A. J. Arvia, "Validity of the Kardar-Parisi-Zhang equation in the asymptotic limit of metal electrodeposition", *Phys. Rev. B* **59**, 4638 (1999).

[12] M. A. C. Huergo, M. A. Pasquale, P. H. González, A. E. Bolzán, and A. J. Arvia, "Growth dynamics of cancer cell colonies and their comparison with noncancerous cells", *Phys. Rev. E* **85**, 011918 (2012).

[13] P. J. Yunker, T. Still, M. A. Lohr, and A. G. Yodh, "Suppression of the coffee-ring effect by shape-dependent capillary interactions", *Nature* **476**, 308 (2011).

[14] P. J. Yunker, M. A. Lohr, T. Still, A. Borodin, D. J. Durian, and A. G. Yodh, "Effects of particle shape on growth dynamics at edges of evaporating drops of colloidal suspensions", *Phys. Rev. Lett.* **110**, 035501 (2013).

[15] S. Atis, A. K. Dubey, D. Salin, L. Talon, P. Le Doussal, and K. J. Wiese, "Experimental Evidence for Three Universality Classes for Reaction Fronts in Disordered Flows", *Phys. Rev. Lett.* **114**, 234502 (2015).

[16] S. F. Edwards and D. R. Wilkinson, "The Surface Statistics of a Granular Aggregate", *Proc. R. Soc. London, Ser. A* **381**, 17 (1982).

[17] J. Krug, P. Meakin, and T. Halpin-Healy, "Amplitude universality for driven interfaces and directed polymers in random media", *Phys. Rev. A* **45**, 638 (1992).

[18] J. Anderson and J. Johansson, "The probability density function tail of the Kardar–Parisi–Zhang equation in the strongly non-linear regime", *J. Phys. A: Math. Theor.* **49**, 505001 (2016).

[19] S. Nakajima, "Divergence of shape fluctuation for general distributions in first passage percolation", *arXiv:1706.03493* (2017).

[20] T. Halpin-Healy, "(2+1)-Dimensional Directed Polymer in a Random Medium: Scaling Phenomena and Universal Distributions", *Phys. Rev. Lett.* **109** (2012).

[21] R. A. L. Almeida, S. O. Ferreira, T. J. Oliveira, and F. D.A.A. a. Reis, "Universal fluctuations in the growth of semiconductor thin films", *Phys. Rev. B* **89**, 045309 (2014).

[22] T. Halpin-Healy and G. Palasantzas, "Universal correlators and distributions as experimental signatures of (2+1)-dimensional Kardar–Parisi–Zhang growth", *EPL* **105**, 50001 (2014).

[23] D. A. Huse, C. L. Henley, and D. S. Fisher, "Huse, Henley, and Fisher respond", *Phys. Rev. Lett.* **55**, 2924 (1985).

[24] K. A. Takeuchi, "An appetizer to modern developments on the Kardar–Parisi–Zhang universality class", *Physica A* **504**, 77 (2018).

[25] D. Forster, D. R. Nelson, and M. J. Stephen, "Large-distance and long-time properties of a randomly stirred fluid", *Phys. Rev. A* **16**, 732 (1977).

[26] H. Spohn, "Fluctuating Hydrodynamics Approach to Equilibrium Time Correlations for Anharmonic Chains", in *Thermal Transport in Low Dimensions*, 921 (Springer International Publishing, 2016), pp. 107–158.

[27] K. Johansson, "Shape Fluctuations and Random Matrices", *Commun. Math. Phys.* **209**, 437 (2000).

[28] T. Kriecherbauer and J. Krug, "A pedestrian's view on interacting particle systems, KPZ universality and random matrices", *J. Phys. A: Math. Theor.* **43**, 403001 (2010).

[29] A. S. Pikovsky and J. Kurths, "Roughening interfaces in the dynamics of perturbations of spatiotemporal chaos", *Phys. Rev. E* **49**, 898 (1994).

[30] L. Chen, C. F. Lee, and J. Toner, "Mapping two-dimensional polar active fluids to two-dimensional soap and one-dimensional sandblasting", *Nat. Commun.* **7**, 12215 (2016).

[31] A. Nahum, J. Ruhman, S. Vijay, and J. Haah, "Quantum Entanglement Growth under Random Unitary Dynamics", *Phys. Rev. X* **7**, 031016 (2017).

[32] M. Prähofer and H. Spohn, "Universal Distributions for Growth Processes in 1+1 Dimensions and Random Matrices", *Phys. Rev. Lett.* **84**, 4882 (2000).

[33] I. Corwin, "The Kardar–Parisi–Zhang Equation and Universality Class", *Random Matrices Theory Appl.* **01**, 1130001 (2012).

[34] K. A. Takeuchi and M. Sano, "Universal Fluctuations of Growing Interfaces: Evidence in Turbulent Liquid Crystals", *Phys. Rev. Lett.* **104**, 230601 (2010).

[35] K. A. Takeuchi, M. Sano, T. Sasamoto, and H. Spohn, "Growing interfaces uncover universal fluctuations behind scale invariance.", *Sci. Rep.* **1**, 34 (2011).

[36] K. A. Takeuchi and M. Sano, "Evidence for Geometry-Dependent Universal Fluctuations of the Kardar-Parisi-Zhang Interfaces in Liquid-Crystal Turbulence", *J. Stat. Phys.* **147**, 853 (2012).

[37] K. A. Takeuchi, M. Kuroda, H. Chaté, and M. Sano, "Directed Percolation Criticality in Turbulent Liquid Crystals", *Phys. Rev. Lett.* **99**, 234503 (2007).

[38] K. A. Takeuchi, M. Kuroda, H. Chaté, and M. Sano, "Experimental realization of directed percolation criticality in turbulent liquid crystals", *Phys. Rev. E* **80**, 051116 (2009).

[39] T. Sasamoto and H. Spohn, "The 1+1-dimensional Kardar–Parisi–Zhang equation and its universality class", *J. Stat. Mech. Theor. Exp.* **2010**, P11013 (2010).

[40] J. Quastel, "Introduction to KPZ", in *Current Developments in Mathematics*, Vol. 2011 (International Press of Boston, Incorporated, Somerville, 2012).

[41] J. Quastel and H. Spohn, "The One-Dimensional KPZ Equation and Its Universality Class", *J. Stat. Phys.* **160**, 965 (2015).

[42] T. Sasamoto, "The 1D Kardar–Parisi–Zhang equation: Height distribution and universality", *Prog. Theor. Exp. Phys.* **2016**, 022A01 (2016).

[43] F. Comets, "Kardar-Parisi-Zhang Equation and Universality", in *Directed Polymers in Random Environments* (Springer, Cham, 2017), pp. 127–146.

[44] T. Nattermann and W. Renz, "Diffusion in a random catalytic environment, polymers in random media, and stochastically growing interfaces", *Phys. Rev. A* **40**, 4675 (1989).

[45] T. Halpin-Healy, "Directed polymers in random media: Probability distributions", *Phys. Rev. A* **44**, R3415 (1991).

[46] J. M. Kim, M. A. Moore, and A. J. Bray, "Zero-temperature directed polymers in a random potential", *Phys. Rev. A* **44**, 2345 (1991).

[47] M. Plischke and Z. Rácz, "Active Zone of Growing Clusters: Diffusion-Limited Aggregation and the Eden Model", *Phys. Rev. Lett.* **53**, 415 (1984).

[48] M. Plischke and Z. Rácz, "Dynamic scaling and the surface structure of Eden clusters", *Phys. Rev. A* **32**, 3825 (1985).

[49] S. Havlin, S. V. Buldyrev, H. E. Stanley, and G. H. Weiss, "Probability distribution of the interface width in surface roughening: analogy with a Levy flight", *J. Phys. A: Math. Gen.* **24**, L925 (1991).

[50] M. Prähofer and H. Spohn, "Statistical self-similarity of one-dimensional growth processes", *Physica A* **279**, 342 (2000).

[51] G. W. Anderson, A. Guionnet, and O. Zeitouni, *An introduction to random matrices*, 118 (Cambridge University Press, 2010).

[52] J. Quastel and D. Remenik, "Airy Processes and Variational Problems", in *Topics in Percolative and Disordered Systems* (Springer, New York, NY, 2014), pp. 121–171.

[53] T. Sasamoto, "Spatial correlations of the 1D KPZ surface on a flat substrate", *J. Phys. A: Math. Gen.* **38**, L549 (2005).

[54] P. L. Ferrari and H. Spohn, "A determinantal formula for the GOE Tracy–Widom distribution", *J. Phys. A: Math. Gen.* **38**, L557 (2005).

[55] F. Bornemann, "On the numerical evaluation of Fredholm determinants", *Math. Comp.* **79**, 871 (2010).

[56] O. Vallée and M. Soares, *Airy Functions and Applications to Physics* (IMPERIAL COLLEGE PRESS, 2004).

[57] J. Baik and E. M. Rains, "Limiting Distributions for a Polynuclear Growth Model with External Sources", *J. Stat. Phys.* **100**, 523 (2000).

[58] P. L. Ferrari and H. Spohn, "Scaling Limit for the Space-Time Covariance of the Stationary Totally Asymmetric Simple Exclusion Process", *Commun. Math. Phys.* **265**, 1 (2006).

[59] T. Sasamoto and H. Spohn, "One-Dimensional Kardar-Parisi-Zhang Equation: An Exact Solution and its Universality", *Phys. Rev. Lett.* **104**, 230602 (2010).

[60] G. Amir, I. Corwin, and J. Quastel, "Probability distribution of the free energy of the continuum directed random polymer in 1+1 dimensions", *Commun. Pure Appl. Math.* **64**, 466 (2011).

[61] T. Sasamoto and H. Spohn, "Exact height distributions for the KPZ equation with narrow wedge initial condition", *Nucl. Phys. B* **834**, 523 (2010).

[62] P. Calabrese, P. L. Doussal, and A. Rosso, "Free-energy distribution of the directed polymer at high temperature", *EPL* **90**, 20002 (2010).

[63] V. Dotsenko, "Bethe ansatz derivation of the Tracy-Widom distribution for one-dimensional directed polymers", *EPL* **90**, 20003 (2010).

[64] P. Calabrese and P. Le Doussal, "Exact Solution for the Kardar-Parisi-Zhang Equation with Flat Initial Conditions", *Phys. Rev. Lett.* **106**, 250603 (2011).

[65] T. Imamura and T. Sasamoto, "Exact Solution for the Stationary Kardar-Parisi-Zhang Equation", *Phys. Rev. Lett.* **108**, 190603 (2012).

[66] T. Imamura and T. Sasamoto, "Stationary Correlations for the 1D KPZ Equation", *J. Stat. Phys.* **150**, 908 (2013).

[67] A. Borodin, I. Corwin, P. Ferrari, and B. Vető, "Height Fluctuations for the Stationary KPZ Equation", *Math. Phys. Anal. Geom.* **18**, 20 (2015).

[68] M. Prähofer and H. Spohn, "Scale Invariance of the PNG Droplet and the Airy Process", *J. Stat. Phys.* **108**, 1071 (2002).

[69] K. Johansson, "Discrete Polynuclear Growth and Determinantal Processes", *Commun. Math. Phys.* **242**, 277 (2003).

[70] A. Borodin, P. L. Ferrari, and T. Sasamoto, "Large Time Asymptotics of Growth Models on Space-like Paths II: PNG and Parallel TASEP", *Commun. Math. Phys.* **283**, 417 (2008).

[71] S. Prolhac and H. Spohn, "The one-dimensional KPZ equation and the Airy process", *J. Stat. Mech. Theor. Exp.* **2011**, P03020 (2011).

[72] A. Borodin, P. L. Ferrari, and P. Michael, "Fluctuations in the Discrete TASEP with Periodic Initial Configurations and the Airy1 Process", *Int. Math. Res. Pap.* **2007** (2007).

[73] J. Baik, P. L. Ferrari, and S. Péché, "Limit process of stationary TASEP near the characteristic line", *Commun. Pure Appl. Math.* **63**, 1017 (2010).

[74] P. L. Ferrari and H. Spohn, "On the current time correlations for one-dimensional exclusion processes", *arXiv:1602.00486* (2016).

[75] V. Dotsenko, "On two-time distribution functions in (1+1) random directed polymers", *J. Phys. A: Math. Theor.* **49**, 27LT01 (2016).

[76] K. Johansson, "Two Time Distribution in Brownian Directed Percolation", *Commun. Math. Phys.* **351**, 441 (2017).

[77] K. Johansson, "The two-time distribution in geometric last-passage percolation", *arXiv:1802.00729* (2018).

[78] J. De Nardis, P. Le Doussal, and K. A. Takeuchi, "Memory and Universality in Interface Growth", *Phys. Rev. Lett.* **118**, 125701 (2017).

[79] J. de Nardis and P. le Doussal, "Tail of the two-time height distribution for KPZ growth in one dimension", *J. Stat. Mech. Theor. Exp.* **2017**, 053212 (2017).

[80] S. Kai, W. Zimmermann, M. Andoh, and N. Chizumi, "Spontaneous Nucleation of Turbulence in Electrohydrodynamics and Its Similarity with Crystal Growth", *J. Phys. Soc. Jpn.* **58**, 3449 (1989).

[81] V. S. U. Fazio and L. Komitov, "Alignment transition in a nematic liquid crystal due to field-induced breaking of anchoring", *EPL* **46**, 38 (1999).

[82] S. Kai, W. Zimmermann, M. Andoh, and N. Chizumi, "Local transition to turbulence in electrohydrodynamic convection", *Phys. Rev. Lett.* **64**, 1111 (1990).

[83] S. Kai and W. Zimmermann, "Pattern Dynamics in the Electrohydrodynamics of Nematic Liquid Crystals", *Prog. Theor. Phys. Supp.* **99**, 458 (1989).

[84] J. Nehring, "Calculation of the Structure and Energy of Nematic Threads", *Phys. Rev. A* **7**, 1737 (1973).

[85] N. Scaramuzza, C. Versace, and V. Carbone, "Intermittency at the DSM1-DSM2 Transition in Nematic Liquid Crystal Films", *Mol. Cryst. Liq. Cryst.* **266**, 85 (1995).

[86] V. S. U. Fazio, F. Nannelli, and L. Komitov, "Sensitive methods for estimating the anchoring strength of nematic liquid crystals on Langmuir-Blodgett monolayers of fatty acids", *Phys. Rev. E* **63**, 061712 (2001).

[87] K. A. Takeuchi and T. Akimoto, "Characteristic Sign Renewals of Kardar–Parisi–Zhang Fluctuations", *J. Stat. Phys.* **164**, 1167 (2016).

[88] T. Sasamoto and T. Imamura, "Fluctuations of the One-Dimensional Polynuclear Growth Model in Half-Space", *J. Stat. Phys.* **115**, 749 (2004).

[89] T. Sasamoto, "Fluctuations of the one-dimensional asymmetric exclusion process using random matrix techniques", *J. Stat. Mech. Theor. Exp.* **2007**, P07007 (2007).

[90] T. Gueudré and P. L. Doussal, "Directed polymer near a hard wall and KPZ equation in the half-space", *EPL* **100**, 26006 (2012).

[91] J. Baik, G. Barraquand, I. Corwin, and T. Suidan, "Pfaffian Schur processes and last passage percolation in a half-quadrant", *arXiv:1606.00525* (2016).

[92] A. Borodin, A. Bufetov, and I. Corwin, "Directed random polymers via nested contour integrals", *Ann. Phys.* **368**, 191 (2016).

[93] J. Baik, G. Barraquand, I. Corwin, and T. Suidan, "Facilitated exclusion process", *arXiv:1707.01923* (2017).

[94] G. Barraquand, A. Borodin, and I. Corwin, "Half-space Macdonald processes", *arXiv:1802.08210* (2018).

[95] Y. Ito and K. A. Takeuchi, "When fast and slow interfaces grow together: Connection to the half-space problem of the Kardar-Parisi-Zhang class", *Phys. Rev. E* **97**, 040103 (2018).

[96] I. S. S. Carrasco and T. J. Oliveira, "Universality and dependence on initial conditions in the class of the nonlinear molecular beam epitaxy equation", *Phys. Rev. E* **94**, 050801 (2016).

[97] M. O. Lavrentovich, K. S. Korolev, and D. R. Nelson, "Radial Domany-Kinzel models with mutation and selection", *Phys. Rev. E* **87**, 012103 (2013).

[98] O. Hallatschek, P. Hersen, S. Ramanathan, and D. R. Nelson, "Genetic drift at expanding frontiers promotes gene segregation", *Proc. Natl. Acad. Sci.* **104**, 19926 (2007).

[99] I. S. S. Carrasco, K. A. Takeuchi, S. C. Ferreira, and T. J. Oliveira, "Interface fluctuations for deposition on enlarging flat substrates", *New J. Phys.* **16**, 123057 (2014).

[100] I. S. S. Carrasco and T. J. Oliveira, "Circular Kardar-Parisi-Zhang interfaces evolving out of the plane", *arXiv:1810.11292* (2018).

[101] K. A. Takeuchi, "Statistics of circular interface fluctuations in an off-lattice Eden model", *J. Stat. Mech. Theor. Exp.* **2012**, P05007 (2012).

[102] J. Quastel and D. Remenik, "How flat is flat in random interface growth?", *arXiv:1606.09228* (2016).

[103] P. G. de Gennes and J. Prost, *The Physics of Liquid Crystals* (Oxford University Press, U.S.A., Oxford, 1995).

[104] A. M. Weiner, "Femtosecond pulse shaping using spatial light modulators", *Rev. Sci. Instrum.* **71**, 1929 (2000).

[105] J. E. Curtis, B. A. Koss, and D. G. Grier, "Dynamic holographic optical tweezers", *Opt. Commun.* **207**, 169 (2002).

[106] A. K. Ghatak and K. Thyagarajan, *Contemporary Optics* (Springer US, Boston, 1978).

[107] F. Wyrowski and O. Bryngdahl, "Iterative Fourier-transform algorithm applied to computer holography", *J. Opt. Soc. Am. A* **5**, 1058 (1988).

[108] M. Hacker, G. Stobrawa, and T. Feurer, "Iterative Fourier transform algorithm for phase-only pulse shaping", *Opt. Express* **9**, 191 (2001).

[109] S. G. Alves, T. J. Oliveira, and S. C. Ferreira, "Non-universal parameters, corrections and universality in Kardar–Parisi–Zhang growth", *J. Stat. Mech. Theor. Exp.* **2013**, P05007 (2013).

[110] S. C. Ferreira and S. G. Alves, "Pitfalls in the determination of the universality class of radial clusters", *J. Stat. Mech. Theor. Exp.* **2006**, P11007 (2006).

[111] Y. T. Fukai and K. A. Takeuchi, "Kardar-Parisi-Zhang Interfaces with Inward Growth", *Phys. Rev. Lett.* **119**, 030602 (2017).

[112] I. Corwin, Z. Liu, and D. Wang, "Fluctuations of TASEP and LPP with general initial data", (2014).

[113] I. Corwin and A. Hammond, "KPZ line ensemble", *Probab. Theory Related Fields* **166**, 67 (2016).

[114] I. Corwin, J. Quastel, and D. Remenik, "Renormalization Fixed Point of the KPZ Universality Class", *J. Stat. Phys.* **160**, 815 (2015).

[115] F. Bornemann, P. L. Ferrari, and M. Prähofer, "The Airy1 Process is not the Limit of the Largest Eigenvalue in GOE Matrix Diffusion", *J. Stat. Phys.* **133**, 405 (2008).

[116] D. T. Gillespie, "Exact numerical simulation of the Ornstein-Uhlenbeck process and its integral", *Phys. Rev. E* **54**, 2084 (1996).

[117] F. Bornemann, "On the Numerical Evaluation of Distributions in Random Matrix Theory: A Review", *arXiv:0904.1581* (2009).

[118] A. Borodin, P. L. Ferrari, and T. Sasamoto, "Transition between Airy1 and Airy2 processes and TASEP fluctuations", *Commun. Pure Appl. Math.* **61**, 1603 (2008).

[119] P. le Doussal, "Crossover between various initial conditions in KPZ growth: flat to stationary", *J. Stat. Mech. Theor. Exp.* **2017**, 053210 (2017).

[120] H. Hinrichsen, "Non-equilibrium critical phenomena and phase transitions into absorbing states", *Adv. Phys.* **49**, 815 (2000).

[121] M. Henkel, H. Hinrichsen, and S. Luebeck, *Non-Equilibrium Phase Transitions: Volume 1: Absorbing Phase Transitions* (Springer, Dordrecht; New York, 2009).

[122] T. E. Harris, "Contact Interactions on a Lattice", *Ann. Probab.* **2**, 969 (1974).

[123] J. Marro, *Nonequilibrium Phase Transitions in Lattice Models* (Cambridge University Press, Cambridge, 2008).

[124] I. Jensen, "Low-density series expansions for directed percolation: I. A new efficient algorithm with applications to the square lattice", *J. Phys. A: Math. Gen.* **32**, 5233 (1999).

[125] J. Wang, Z. Zhou, Q. Liu, T. M. Garoni, and Y. Deng, "High-precision Monte Carlo study of directed percolation in (d+1) dimensions", *Phys. Rev. E* **88**, 042102 (2013).

[126] H. K. Janssen, "On the nonequilibrium phase transition in reaction-diffusion systems with an absorbing stationary state", *Z. Phys. B* **42**, 151 (1981).

[127] P. Grassberger, "On phase transitions in Schlögl's second model", *Z. Phys. B* **47**, 365 (1982).

[128] M. Sano and K. Tamai, "A universal transition to turbulence in channel flow", *Nature Physics* **12**, 249 (2016).

[129] G. Lemoult, L. Shi, K. Avila, S. V. Jalikop, M. Avila, and B. Hof, "Directed percolation phase transition to sustained turbulence in Couette flow", *Nature Physics* **12**, 254 (2016).

[130] Y. Pomeau, "Front motion, metastability and subcritical bifurcations in hydrodynamics", *Physica D* **23**, 3 (1986).

[131] O. Reynolds, "XXIX. An experimental investigation of the circumstances which determine whether the motion of water shall be direct or sinuous, and of the law of resistance in parallel channels", *Philos. Trans. Roy. Soc. London* **174**, 935 (1883).

[132] A. Hankey and H. E. Stanley, "Systematic Application of Generalized Homogeneous Functions to Static Scaling, Dynamic Scaling, and Universality", *Phys. Rev. B* **6**, 3515 (1972).

[133] M. Eden, "A Two-dimensional Growth Process", in Proceedings of the Fourth Berkeley Symposium on Mathematical Statistics and Probability, Volume 4: Contributions to Biology and Problems of Medicine (1961).

[134] R. Jullien and R. Botet, "Surface Thickness in the Eden Model", *Phys. Rev. Lett.* **54**, 2055 (1985).

[135] K. A. Takeuchi, "Universal behavior of macroscopic out-of-equilibrium systems examined in the electrohydrodynamic turbulence of liquid crystals", Ph. D. Thesis (the University of Tokyo, Tokyo, Japan, 2010).

[136] C. Mueller and R. Tribe, "Stochastic pde's arising from the long range contact and long range voter processes", *Probab. Theory Related Fields* **102**, 519 (1995).

[137] R. A. Fisher, "THE WAVE OF ADVANCE OF ADVANTAGEOUS GENES", *Ann. Eugenics* **7**, 355 (1937).

[138] A. Kolmogorov, I. Petrovskii, and N. Piscounov, "A study of the diffusion equation with increase in the amount of substance, and its application to a biological problem", trans. by V. M. Volosov, *Moscow Univ. Math. Bull.* **1**, 1 (1937).

[139] J. D. Murray, *Mathematical Biology*, 2nd ed. (Springer-Verlag, Berlin; Heidelberg, 1993).

[140] M. Bramson, "Convergence of Solutions of the Kolmogorov Equation to Travelling Waves", *Mem. Amer. Math. Soc.* **44** (1983).

[141] S. Nesic, R. Cuerno, and E. Moro, "Macroscopic Response to Microscopic Intrinsic Noise in Three-Dimensional Fisher Fronts", *Phys. Rev. Lett.* **113**, 180602 (2014).

[142] L. Pechenik and H. Levine, "Interfacial velocity corrections due to multiplicative noise", *Phys. Rev. E* **59**, 3893 (1999).

[143] E. Moro, "Internal Fluctuations Effects on Fisher Waves", *Phys. Rev. Lett.* **87**, 238303 (2001).

[144] E. Brunet, B. Derrida, A. H. Mueller, and S. Munier, "Phenomenological theory giving the full statistics of the position of fluctuating pulled fronts", *Phys. Rev. E* **73**, 056126 (2006).

[145] C. Mueller, L. Mytnik, and J. Quastel, "Effect of noise on front propagation in reaction-diffusion equations of KPP type", *Inventiones mathematicae* **184**, 405 (2011).

[146] C. R. Doering, C. Mueller, and P. Smereka, "Interacting particles, the stochastic Fisher–Kolmogorov–Petrovsky–Piscounov equation, and duality", *Physica A* **325**, 243 (2003).

[147] O. Hallatschek and K. S. Korolev, "Fisher Waves in the Strong Noise Limit", *Phys. Rev. Lett.* **103**, 108103 (2009).

[148] I. Dornic, H. Chaté, and M. A. Muñoz, "Integration of Langevin Equations with Multiplicative Noise and the Viability of Field Theories for Absorbing Phase Transitions", *Phys. Rev. Lett.* **94**, 100601 (2005).

[149] W. H. Press, S. A. Teukolsky, W. T. Vetterling, and B. P. Flannery, *Numerical Recipes 3rd Edition: The Art of Scientific Computing*, 3rd ed. (Cambridge University Press, Cambridge; New York, 2007).

[150] E. Moro and H. Schurz, "Boundary Preserving Semianalytic Numerical Algorithms for Stochastic Differential Equations", *SIAM J. Sci. Comput.* **29**, 1525 (2007).

[151] S. Kliem, "Travelling wave solutions to the KPP equation with branching noise arising from initial conditions with compact support", *Stochastic Process. Appl.* **127**, 385 (2017).

[152] K. Tamai, *Private communication*, 2018.

[153] H. Yamaguchi, *Private communication*, 2018.

[154] A Costa, R. A. Blythe, and M. R. Evans, "Discontinuous transition in a boundary driven contact process", *J. Stat. Mech. Theor. Exp.* **2010**, P09008 (2010).

[155] K. Tamai and M. Sano, "How to experimentally probe universal features of absorbing phase transitions using steady state", *arXiv:1712.05789* (2017).